

UNIVERSITY OF CAMBRIDGE

**Measurements of $B \rightarrow \mu^+ \mu^-$ decays using
the LHCb Experiment**

Hannah Mary Evans

Selwyn College

supervisor
Prof. Val Gibson

Abstract

This dissertation documents studies of very rare B meson decays at the LHCb experiment on data taken during the first two experiment runs of the Large Hadron Collider (LHC).

The LHCb experiment was designed to test the Standard Model of particle physics and search for new physics theories that go beyond the scope of the Standard Model, through the decay of b -hadrons produced in high energy proton-proton collisions at the LHC. The measurements described in this dissertation were made using data samples of proton-proton collisions with integrated luminosities of 1.0, 2.0 and 1.4 fb^{-1} , collected at centre-of-mass energies of 7, 8 and 13 TeV respectively.

The branching fractions and effective lifetimes of the very rare $B_s^0 \rightarrow \mu^+ \mu^-$ and $B^0 \rightarrow \mu^+ \mu^-$ decays are sensitive to particles from new physics theories. New physics processes could influence the $B_s^0 \rightarrow \mu^+ \mu^-$ effective lifetime and branching fraction independently, and therefore the two observables are complementary in the search for new physics.

The $B_s^0 \rightarrow \mu^+ \mu^-$ decay is observed with a statistical significance of 7.9σ and the branching fraction is measured as $\mathcal{B}(B_s^0 \rightarrow \mu^+ \mu^-) = (2.8 \pm 0.6) \times 10^{-9}$. The $B_s^0 \rightarrow \mu^+ \mu^-$ effective lifetime is measured for the first time as $2.04 \pm 0.44 \text{ (stat)} \pm 0.05 \text{ (syst)} \text{ ps}$. An upper limit is placed on the branching fraction $\mathcal{B}(B^0 \rightarrow \mu^+ \mu^-) < 6.1 \times 10^{-10}$ at the 95 % confidence level. All results are consistent with the predictions of the Standard Model.

Declaration

Here I shall say the appropriate lines that are needed to say that this thesis is actually mine.

Hannah Evans
March 2017

Acknowledgements

Preface

Table of contents

Abstract	iii
Acknowledgements	vii
Preface	ix
1 Introduction	1
2 Theory of $B_{(s)}^0 \rightarrow \mu^+ \mu^-$ decays; the Standard Model and Beyond.	3
3 CERN, the LHC and the LHCb Experiment	5
3.1 The LHC	5
3.2 LHCb Experiment	8
3.2.1 Tracking	9
3.2.2 Particle Identification	17
3.2.3 The Trigger	25
3.2.4 LHCb Software and Simulation	27
3.2.5 LHCb data collected so far	29
4 Event Selection	31
5 Measurement of $B_{(s)}^0 \rightarrow \mu^+ \mu^-$ Branching Fractions	33
5.1 Analysis Strategy	33
5.2 $B_s^0 \rightarrow \mu^+ \mu^-$ mass and BDT <i>pdfs</i>	36
5.2.1 Mass <i>pdfs</i>	36
5.2.2 BDT <i>pdfs</i>	37
5.2.3 Decay time dependence of the $B_s^0 \rightarrow \mu^+ \mu^-$ BDT <i>pdf</i>	38
5.3 Background mass <i>pdfs</i> and expected yields	39
5.3.1 $B \rightarrow h^+ h^-$ mass and BDT <i>pdfs</i>	40
5.3.2 Semi-leptonic mass and BDT <i>pdfs</i>	41

5.4	Normalisation	41
5.4.1	$B^0 \rightarrow K^+ \pi^-$ and $B^+ \rightarrow J/\psi K^+$ yields	42
5.4.2	Efficiency ratio	42
5.4.3	Hadronisation factors	44
5.4.4	Normalisation parameters	44
5.5	Results	45
6	Measurement of the $B_s^0 \rightarrow \mu^+ \mu^-$ effective lifetime	47
6.1	Analysis Strategy	47
6.2	Mass <i>pdfs</i>	49
6.3	Decay time <i>pdfs</i>	50
6.3.1	$B_s^0 \rightarrow \mu^+ \mu^-$ decay time <i>pdf</i>	51
6.3.2	Background decay time <i>pdf</i>	59
6.4	Toy Studies for fit optimisation	62
6.4.1	To fit for τ or τ^{-1}	64
6.4.2	Toy Results	67
6.5	Results	72
7	Systematic Uncertainties and Cross Checks	75
8	Summary and Future Outlook	77
	Bibliography	79
A	Distributions of input variables for the global BDT	81

Chapter 1

Introduction

This will include a brief introduction of why B2MuMu decays are interesting and the current experimental status of the decays - CMS-LHCb combination and the ALTAS result.

Chapter 2

Theory of $B_{(s)}^0 \rightarrow \mu^+ \mu^-$ decays; the Standard Model and Beyond.

Chapter 3

CERN, the LHC and the LHCb Experiment

The European Organisation for Nuclear Research (CERN) was founded in 1954, it began with 12 member states as a organisation to encourage European collaboration and the study of nuclear physics. The collaborative nature of CERN allowed large-scale expensive experiments over the years that individual member states would not have been able to afford. The Proton Synchrotron (PS) was CERN's flagship accelerator, operational in 1959 it had a circumference of 628 m and accelerated protons to 25 GeV. The PS was the highest energy particle accelerator at that time. Now 62 years since its foundation, CERN has grown to include 22 member states¹ and is still at the forefront of high energy physics research. CERN's latest accelerator, the Large Hadron Collider (LHC), is most energetic particle accelerator ever built, with a 27 km circumference the LHC was designed to collide protons at a centre-of-mass energy of 14 TeV. This chapter shall discuss the LHC and the LHC beauty experiment, one of the experiments that studies the products of particle collisions at the LHC.

3.1 The LHC

The LHC is a proton synchrotron designed to accelerate and collide two beams of protons with a centre-of-mass energy of 14 TeV. Although operation of the LHC began in 2010 it is yet to reach the design energy. The purpose of the LHC is to provide high energy proton collisions, the products of which are used for precision tests of the Standard Model (SM) and to search for new physics particles that go beyond the scope

¹Countries and organisations that are unable to become member states can still participate in scientific research as observer states [1].

of the SM. There are four interaction points on the LHC ring where the beams are brought to collide, at these points various experiments detect and study the products of particle collisions. The LHC can also accelerate lead-nuclei up to 2.76 TeV per nucleon, it is only the products from proton collisions that are relevant for the topic of this thesis.

The protons for the LHC come from hydrogen gas, the hydrogen atoms are ionised to strip away the electrons and then the protons are accelerated through a chain of particle accelerators of increasing energy before being injected into the LHC. The chain of accelerators, shown in Fig. 3.1, consists of machines that were used in experiments throughout the second half of the last century and have been modified to meet the requirements needed to provide protons for the LHC.

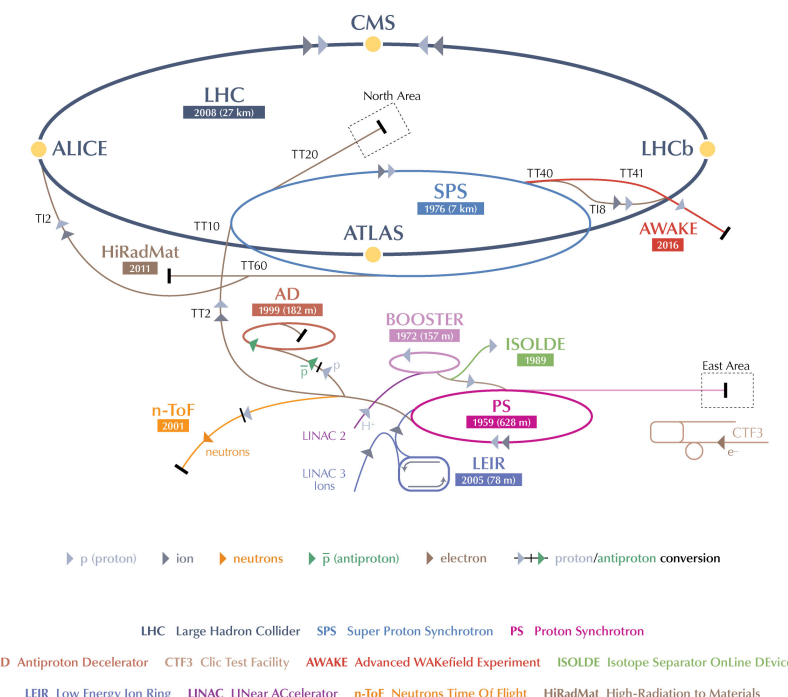


Fig. 3.1 The accelerator complex at CERN. The chain of accelerators used to inject protons into the LHC begins with the Linac 2 which accelerates protons to 50 MeV, these are passed to the Proton Synchrotron Booster that accelerates the protons to 1.4 GeV. The Proton Synchrotron is next in the chain, accelerating protons to 25 GeV and creating the desired spacing between proton bunches. Then finally the Super Proton Synchrotron accelerating protons to 450 GeV ready for injection into the LHC. Source: CERN.

The protons leave the chain of accelerators with an energy of 450 GeV per proton and in bunches of 10^{11} protons, as the bunches are injected into the LHC they are split into two oppositely circulating beams. The LHC accelerates the protons to the

desired centre-of-mass energy using supercooled radio frequency cavities and guides them around the ring with superconducting dipole magnets. Once the required energy has been reached, the bunches are focused using quadrupole magnets before being brought to collide at 4 interaction points around the LHC ring.

The centre-of-mass energy of a collider is an important measure of its performance as it dictates what particles could be produced in collisions, another important measure of collider performance is the instantaneous luminosity a collider can provide. The instantaneous luminosity, \mathcal{L} , is a measure of how many collision occur per second, it is given by

$$\mathcal{L} = \frac{N^2 f n_b}{\mathcal{F}}. \quad (3.1)$$

where N is the number of protons per bunch, n_b the number of bunches per beam, f the bunch revolution frequency and \mathcal{F} contains information about the beam geometry. The LHC is designed to operate at a maximum instantaneous luminosity of $10^{34} \text{ cm}^{-2}\text{s}^{-1}$. To reach this luminosity the LHC can have up to 2808 proton bunches per beam with a revolution frequency of 11.245 kHz, therefore the separation between proton bunches can be as short as 25 ns. The higher the luminosity, the more collisions happen in a second and the more particles will be produced, this can either be advantageous or disadvantageous depending on the physics process that is being studied. Therefore luminosity delivered at each interaction point can be tuned by the quadrupole magnets by altering the shape of each bunch to suit the experiments at each point.

Proton beams first circulated the LHC in 2008 and since then there have been two physics runs separated by a long shutdown period. Run 1 began in 2010 and continued until 2013, during this time protons were collided with a centre-of-mass energy of $\sqrt{s} = 7 \text{ TeV}$ in 2010 and 2011 then this energy was increased to $\sqrt{s} = 8 \text{ TeV}$ for 2012. After Run 1 came first long shutdown (LS1), during this time work was done to prepare the LHC to operate at higher energies and renovation work was preformed on accelerators that provide the LHC with protons. Run 2 began in 2015 with proton collisions at a centre-of-mass energy of $\sqrt{s} = 13 \text{ TeV}$, this Run will continue until 2018 when a second period of upgrades and maintenance, the Long Shutdown 2, will begin.

There are 7 experiments on the LHC that detect particles produced in proton and heavy ion collisions. There are two general purpose detectors, ATLAS and CMS, that were designed to search for the Higgs boson and new particles that are beyond the scope of the SM in proton collisions, these two experiments operate at the full instantaneous luminosity of the LHC. ALICE studies quark-gluon plasma produced in heavy ions collisions to understand conditions similar to those present in the early universe. The TOTEM experiment studies properties of protons as they collide head

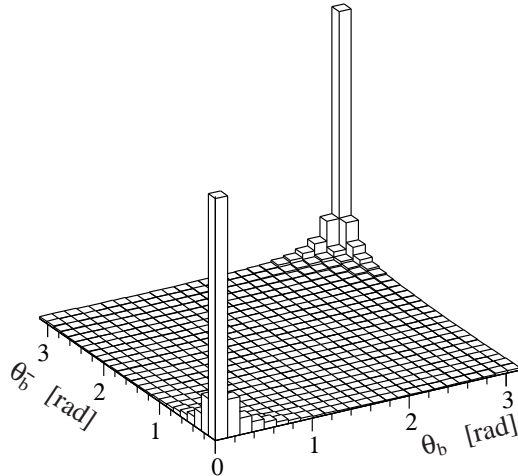


Fig. 3.2 Simulated angular distribution for $b\bar{b}$ production at the LHC, angles are relative the the beam pipe with $\theta = 0$ in the forward direction and $\theta = \pi$ in the backward direction [2].

on at the LHC and the MOEDAL experiment is aims to detect magnetic monopoles. The LHCf experiment is a very forward experiment studying particles that are thrown forward in LHC collisions to understand similar processes that occur in cosmic rays. Finally there is the Large Hadron Collider Beauty experiment (LHCb) that will be described in the next section.

3.2 LHCb Experiment

The LHCb experiment was built to study CP violation and rare decays of b -hadrons to search for new physics processes that could be revealed in these decays. At the LHC $b\bar{b}$ pairs are produced with large transverse momentum, the dominant production mechanisms of $b\bar{b}$ pairs are gluon-gluon fusion, quark anti-quark annihilation and gluon-gluon splitting. The $b\bar{b}$ pairs hadronize to form a range of b -hadrons, including B^+ , B_s^0 and Λ_b^0 , that are studied by LHCb. The large transverse momentum of the $b\bar{b}$ pairs means that the quarks and subsequent b -hadrons are boosted along the beam pipe. The angular distribution of $b\bar{b}$ pairs from pp collision is shown in Figure 3.2.

The LHCb experiment was built as a single arm forward spectrometer, with an angular coverage of 10 to 300 mrad in the vertical direction and 10 to 250 mrad in the horizontal direction relative the the beam pipe. This angular coverage what chosen to exploit the small angles relative the the beam pipe that $b\bar{b}$ pairs are produced at. A cross-section of the detector is shown in Figure 3.3, where a right handed coordinate system is used. Protons collide at the interaction point on the left hand

side of the diagram, the products of the collisions then travel through the detector leaving information in the different sub detectors along the length of the detector. The information deposited in the sub detectors is reconstructed to determine what happened in the proton collisions.

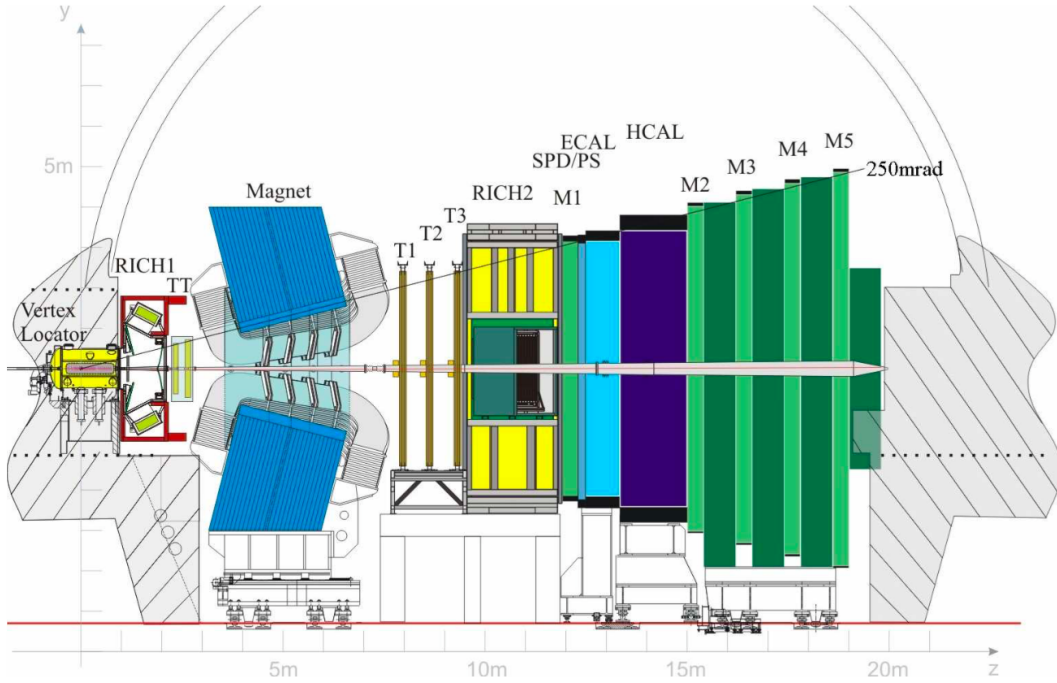


Fig. 3.3 Cross section of the LHCb detector [3].

The different sub detectors have been chosen to exploit the characteristics of b -hadron decays and fall into 2 distinct categories; tracking detectors and particle identification detectors. These detectors and their performance are described briefly in the following sections along with the trigger system and software needed to perform physics analyses. Finally the data recorded by the experiment during Run 1 and Run 2 is presented in Section 3.2.5. For a full description of the detector and its performance during Run 1 see references [4, 5].

3.2.1 Tracking

The tracking system within the LHCb experiment consists of the VELO, the dipole magnet and the tracking stations, together the sub-detectors provide precise information on the passage of charged particles through the detector and the particle momentum. The tracking detectors work on the basic principle that the passage of high energy

charged particles through silicon or ionised gas causes excitation or ionisation atoms in the material. The release of this energy is recorded and translated into an electrical signal that reveals the path of a particle. Precise particle track and momentum measurements are necessary to obtain the accurate particle mass and decay time measurements that help distinguish between different b -hadron decaying in the LHCb detector.

3.2.1.1 The VELO

The VELO is a silicon detector surrounding the interaction point. Its main goal is to provide precise information about the interaction vertices and secondary decay vertices of particles produced in proton collisions. Information the VELO provide enables precise measurements of particle lifetimes and impact parameters of particles tracks necessary for physics analyses.

The VELO is made up of two identical halves, each half consists of 21 stations containing two silicon sensors arranged along the beam pipe. The two halves of the VELO slot together and there is a small hole in the centre of the sensors for the beams to pass through. The arrangement of sensors along the z axis, shown in figure 3.4, it designed such that the sensors cover the full LHCb acceptance and a charged particle within the acceptance will pass through at least three stations. In each station the two sensors measure different coordinates, one measures the r coordinates of charged particles and the other measures the ϕ coordinates as shown in Figure 3.5. The r , ϕ coordinates and the z placement of the sensors are used to reconstruct charged particle trajectories. Cylindrical coordinates were chosen to allow for fast reconstruction for particle trajectories in the VELO.

The momentum resolution achievable for charged tracks is limited by multiple scattering of particles as they travel through material in the detector. Therefore, to ensure good momentum resolution throughout the detector, the VELO is kept in a vacuum to reduce its material budget. Each half of the VELO is enclosed inside an aluminium box, which keeps it in a vacuum and shields the electronic readouts of the from radio frequencies generated by the beam. The overall material budget of the VELO comes to 17.5 % of a radiation length.

Excellent vertex resolution is required in the VELO, to achieve this the sensors in the VELO need to be as close as possible to the interaction point. This is achieved by making the VELO out of two retractable halves and including the interaction point within the coverage of the VELO. During data taking, when the VELO is recording particle tracks the sensors are only 8mm from the beam axis. However during the

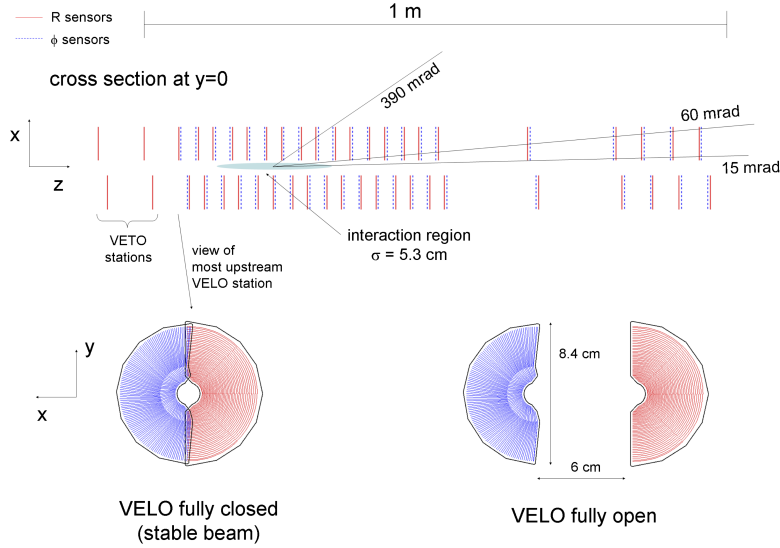


Fig. 3.4 The VELO layout and position of sensors along the beam axis [3].

injection phase of the beam the width of the beam is much greater, therefore the 2 halves of the VELO can retract so that they are 3 cm from the nominal beam axis. This keeps the VELO safe from unnecessary radiation damage. The two halves of the VELO are displaced by 150 mm in the z direction, as shown in Figure 3.4 so that when the VELO is closed, the sensors in each half overlap to help with detector alignment and reduced edge effects.

An additional purpose of the VELO is to act as a veto for high pile up events. There are 2 VELO sensors upstream of the interaction point that provide information to the trigger about how many pp interactions there were with each bunch crossing. Events with large numbers of primary vertices are difficult and time consuming to reconstruct and lead to less precise measurements of particle decay properties. Information from the VELO is used to reject events with high numbers of primary vertices to ensure the best use of information from the detector.

The VELO achieves a vertex resolution of $10 - 20 \mu\text{m}$ transverse to the z direction and $50 - 100 \mu\text{m}$ along the z direction, the resolution of each track depends on the number of tracks in each event as shown in Figure 3.6. The VELO also gives measurements on the impact parameters of particles tracks, which is the distance of closest approach between a particle track and the primary vertex. Figure 3.7 shows the IP resolution for 2012 data, for a track with transverse momentum of $1 \text{ GeV}/c$ it has an impact parameter resolution of $35 \mu\text{m}$.

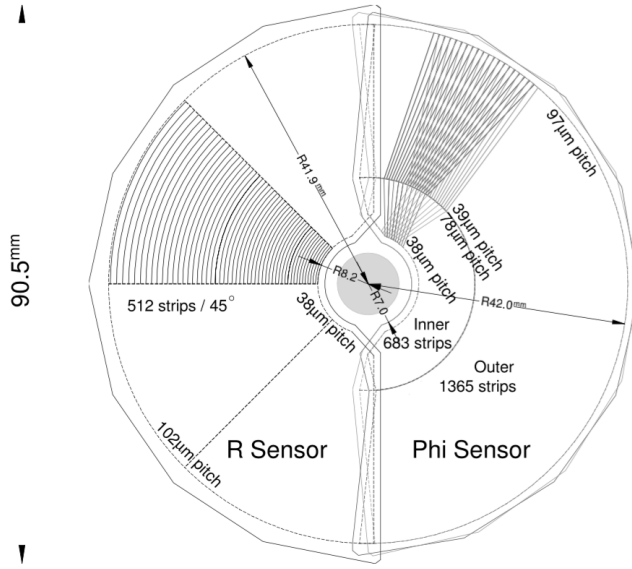


Fig. 3.5 Diagram of r and ϕ sensor layouts [3].

3.2.1.2 The Tracking Stations

The LHCb experiment has 4 tracking stations in addition to the VELO, the Tracker Turicensis (TT) which is located upstream of the magnet and the T stations, T1-T3, located down stream of the magnet. These tracking stations provide complementary tracking information to the VELO and the presence of the magnetic field allows the momentum of charged particles to be determined.

The TT is made up of 4 layers of silicon trackers spaced 27 cm apart that cover the full LHCb angular acceptance. The TT is located just within the influence of

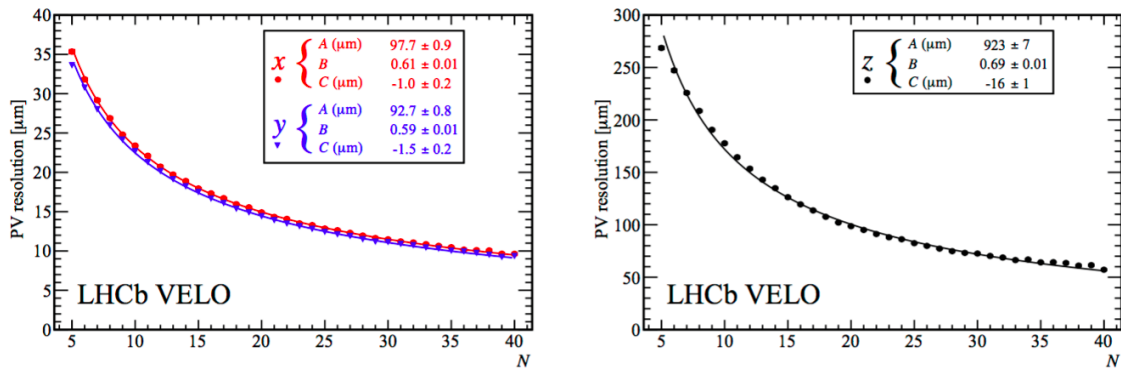


Fig. 3.6 Velo performance for primary vertex resolution perpendicular (left) and parallel (right) to the beam axis as a function of the number of tracks in an event for 2012 data [6].

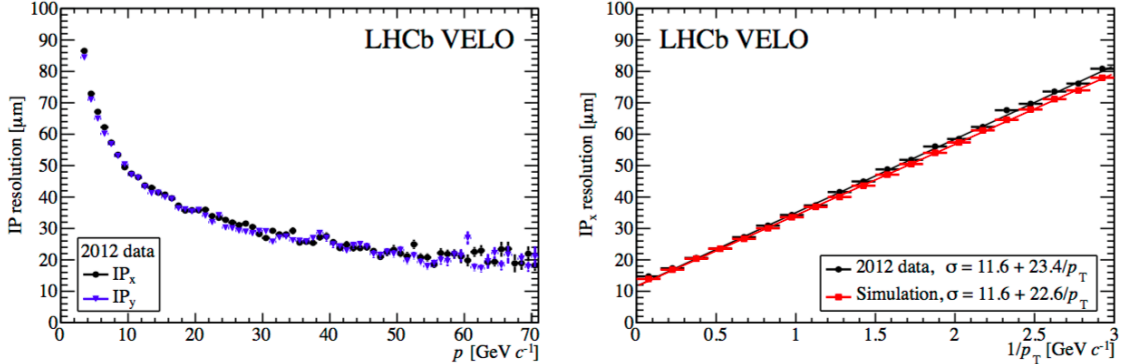


Fig. 3.7 Velo performance for impact parameter resolution as a function of momentum (left) and inverse transverse momentum (right) for 2012 data [6].

the magnetic field of the dipole magnet, which provides the detector with 2 main purposes. Firstly, the TT tracks the passage of charged particles with high momentum to enable good momentum resolution for tracks when combined with the other tracking stations. The TT has a resolution of $50 \mu\text{m}$ for a single hit, this resolution was chosen so that multiple scattering in the detector material rather than detector resolution is the limiting factor for the momentum resolution. The second purpose of the TT is to record tracks of low momentum particles that are then swept out of the detector acceptance as they continue through the magnetic field. These tracks will have a lower momentum resolution but help with pattern recognition within the RICH detectors.

The T stations, T1-3, are split into two sections, each are composed of an Inner Tracker (IT) made of silicon and an Outer Tracker (OT) composed of straw drift tubes. There is a large increase in size of the tracking stations between the TT and the T3 so that all the detectors cover the full angular acceptance of the detector. The TT is 150 cm by 130 cm where as the T3 station is 600cm by 490 cm, this is illustrated in Figure 3.8. The large size of the T stations meant that the high cost of silicon prevented it being used for the full coverage of each station.

The IT has very similar in design to the TT, each station is made of 4 layers of silicon trackers and it has with a track resolution of $50 \mu\text{m}$. The silicon trackers are arranged in a cross shape around the beam pipe, as shown in Figure 3.8, although the IT covers less than 2% of the T stations, 20% of tracks pass through it. This allows the occupancy of the OT to be less than 10% enabling a good overall track resolution from the OT despite it not being made of silicon. The OT of each tracking station is made of 2 staggered layers of straw tubes, they cover the remaining area required for cover

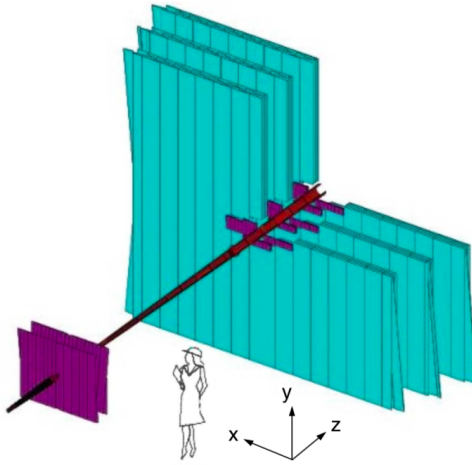


Fig. 3.8 Sizes of the TT and T stations [3].

the LHCb full angular acceptance which includes tracks bend by the magnetic field. The tubes have a fast drift time of 50 ns giving a better than $200 \mu\text{m}$ track resolution.

3.2.1.3 The Dipole Magnet

A warm dipole magnet is used to measure the momentum of charged particles travelling through the LHCb detector. In a magnetic field the trajectories of charged particles are bent and from the radius of curvature of the particle track the particle momentum can be determined.

The magnet is located between the TT and the T stations and its field covers the full LHCb acceptance. The field is in the vertical direction therefore bending tracks in the horizontal direction. The magnet was designed so that the field strength in the RICH detectors is negligible (less than 2 mT) and to have the largest strength possible between the TT and T stations. Figure 3.9 shows a plot of the magnet strength alongside the detector layout. A small magnetic field is achieved in the RICH detectors by iron shielding. The magnet was designed to have an integrated field strength is 4Tm for track that travels 10m through the detector.

The polarity of the magnetic field is periodically switched so that it bends charged tracks in opposite directions. This is done so measure left-right detection asymmetries and to help understand systematic uncertainties of CP violation measurements.

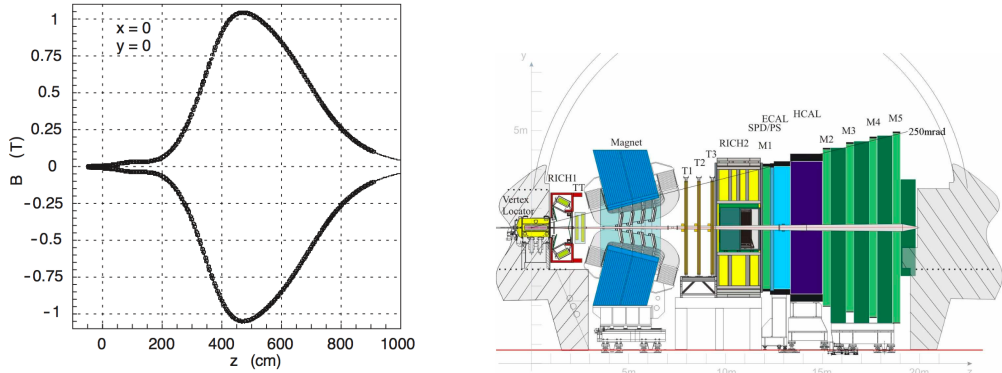


Fig. 3.9 Magnet field of the dipole magnet along the length of the LHCb detector (left) and the layout to the LHCb detector [3]. The peak strength of the field occurs between the TT and T1-3 station.

3.2.1.4 Track reconstruction and performance

The information left by the passage of charged particles in the VELO, TT and T stations is combined using track reconstruction algorithms to find trajectories of charged particles through the length of the LHCb detector and the particle momentum. The algorithms start with either segments of tracks in the VELO or the T stations as seeds and extrapolate from these segments into the other tracking detectors in specific search windows. Once the segments of the track have been found the trajectory is fitted with a Kalam Fitter which takes into account multiple scattering and energy loss within the detector. For each track the fitter returns the χ^2 per degree of freedom, this is a measure of quality for the track. In LHCb this parameter is used to ensure that only good quality tracks are used in physics analyses. The reconstructed tracks are classified into five types depending on which detectors they travelled through, as shown in Figure 3.11.

The different track classifications are:

- **VELO tracks** are formed by particles produced at large angles to the beam axis or travelling in the negative z direction from the interaction point, these particles only leave tracks in the VELO. These tracks are useful for reconstructing primary vertices.
- **Upstream tracks** are made by low momentum particles that only leave hits in the tracking stations upstream of the magnet, the VELO and TT. The absence of tracks further down the detector is because the magnetic field sweeps the particles out of the detector acceptance. Upstream tracks have poor momentum

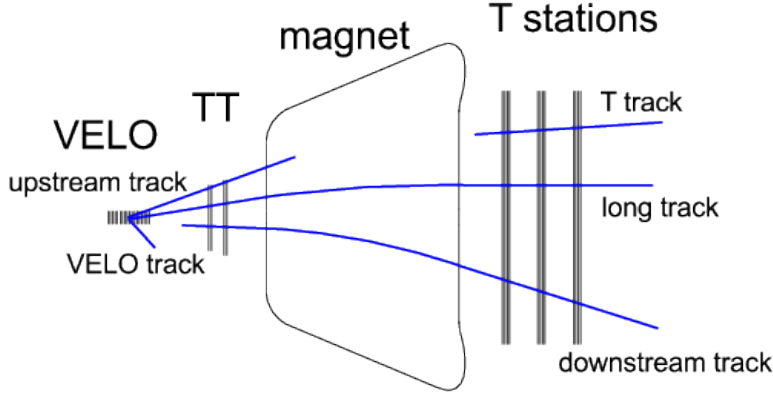


Fig. 3.10 Different types of tracks that are reconstructed at LHCb [7].

resolution but are useful for understanding backgrounds and pattern recognition in the RICH 1 located between the VELO and the TT.

- **Downstream tracks** are produced by decays of long lived neutral particles, that travel out of the VELO before decaying. These particles only leave tracks the TT and T stations.
- **T tracks** are tracks that only cross the T1-3 stations and are formed from particles created in interactions with the detector material. Similarly to upstream tracks, T tracks can help to understand backgrounds and pattern recognition in the RICH 2 located just before the T stations.
- **Long tracks** are the most useful for physics analyses because they are formed by particles that travel through the VELO, TT and T1-3 stations. Information from all the tracking stations is combined so these tracks have the best momentum resolution.

The efficiency to correctly reconstruct tracks varies with different parameters of the events, including the momentum to the particle producing the track and the number of tracks present in the event, as shown in Figure 3.11 for 2012 data. In Run 1 long tracks were correctly reconstructed on average of 96% of the time.

Inevitably not all tracks that are reconstructed are correct, there are two main types of incorrectly reconstructed tracks. The first are clone tracks that occur when the two tracks have many hits in common, when this happens the track with the highest number of total hits is used and the other is discarded. The second type of incorrect tracks are ghost tracks when track segments in different detectors are incorrectly joined

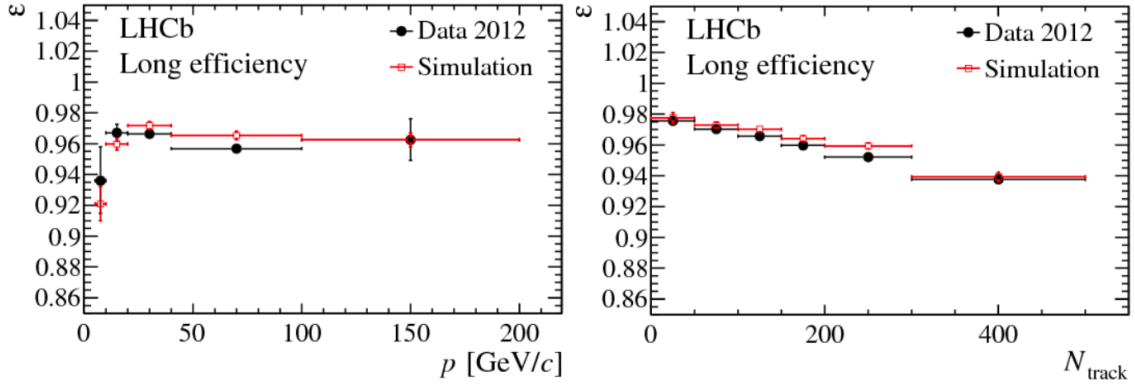


Fig. 3.11 Long track reconstruction efficiency as a function of momentum (left) and number of track in the event (right) for 2012 data [7].

together. This most often occurs with segments in the VELO and T1-3 stations, the number of ghost tracks in an event depends on the event multiplicity. These tracks are removed by cutting on the output of a neural network that returns a probability of how likely a track is to be fake.

Once the tracks have been reconstructed, parameters that are necessary for the identifying and measuring different particles decays in an event can be computed from the tracks. The combined tracking systems achieve a momentum resolution of $\delta p/ = 0.5\%$ for particles with $p = 20$ GeV/c and a resolution of $\delta p/ = 0.8\%$ for particles with $p = 100$ GeV/c. This momentum resolution, when combined with vertex information from the VELO, gives a decay time resolution of around 50 ns.

3.2.2 Particle Identification

In LHCb the particles identification (PID) detectors consist of two ring imaging Cherenkov (RICH) detectors, electromagnetic and hadronic calorimeters and the muons stations. Together these detectors distinguish between different charged leptons and hadrons and between neutral particles such as photons and neutral pions. Good particle identification is necessary to determine which b -hadron decayed and to distinguish between topologically similar decays, such as $B^0 \rightarrow K^+ \pi^-$, $B_s^0 \rightarrow K^+ K^-$ and $B_{(s)}^0 \rightarrow \mu^+ \mu^-$.

3.2.2.1 RICH

RICH detectors are used at LHCb to distinguish between charged hadrons and leptons that have a momentum between 0 and 100 GeV/c. The RICH detectors are vital to

distinguish between pions, kaons and protons frequently produced in b -hadron decays. The energy range of the RICH detectors was chosen because the typical decay products of 2-body b -hadron decays is around 50 GeV.

The RICH detectors are based on the following principle; when a charged particle travels with velocity v through a dielectric medium with a refractive index n , the atoms excited by its passage are polarised, if the particle is travelling faster than the speed of light in the medium the excitation energy is released as a coherent wavefront. The angle, θ_c , the wavefront travels at relative to the particle trajectory depends on the speed at which the particle was travelling as $\cos(\theta_c) = c/nv$. The light produced is called Cherenkov radiation. The RICH detectors measure the angle of light produced as particles pass through them, the angle gives a measurement of the particle's speed which when combined with momentum from the tracking stations gives that particle's mass and therefore its identity.

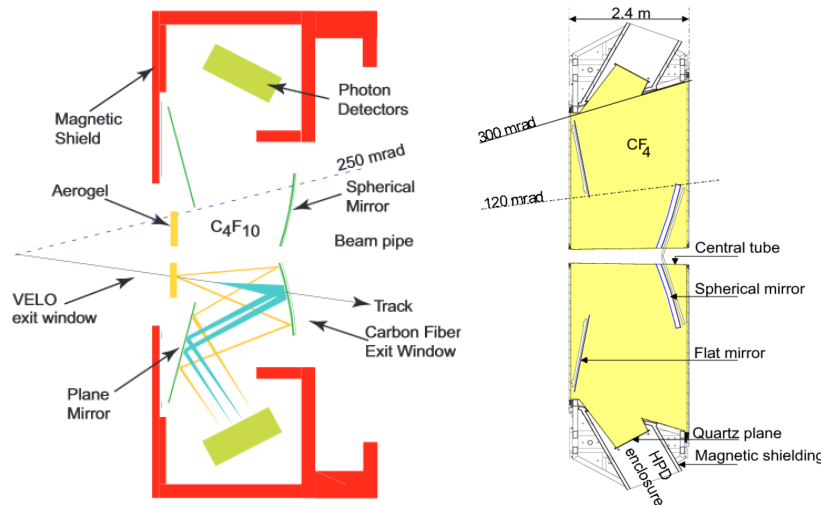


Fig. 3.12 Diagram of the RICH1 detector (left) and the RICH 2 detector (right) [3]. For Run 2 the aerogel radiator in the RICH 1 detector was removed.

The two RICH detectors cover complimentary momentum regions. The RICH 1 detector is located between the VELO and the TT station, it covers the full LHCb angular acceptance and provides PID information on particles in the momentum range 1-60 GeV/c. The RICH 1, is illustrated in Figure 3.12, it contains two different radiator materials; at the front of the detector is a aerogel sensitive to particles with a momentum up to 10 GeV/c, behind the aerogel is a gas radiator sensitive to particles in the momentum range 10 - 60 GeV/c. The aerogel radiation was removed after Run 1, therefore the RICH 1 is only sensitive to particles in the momentum range 10 - 60 GeV/c in Run 2. As charged particles travel through the RICH 1, the rings of

light produced are focused by spherical mirrors onto Hybrid Photon Detectors (HPDs), the radii of the detected rings provides information about how fast the particle was travelling.

The RICH 2 detector is located upstream of the RICH 1, between the last tracking station and before the first muon station. The RICH 2 consists of a gas radiator sensitive to particles with a momentum range 50 - 100 GeV/c and the detection of the light produced is similar to the RICH 1 as illustrated in Figure [?]. Unlike the RICH 1, the RICH 2 detector does not cover the full LHCb angular acceptance but only ± 120 mrad in the horizontal and ± 100 mrad in the vertical direction. This area contains the higher momentum particles the RICH 2 is sensitive to, the low momentum particles have been bent out of the acceptance by the magnetic field.

Both RICH detectors use HPDs that are sensitive to magnetic fields, they are shielded from the magnet field using iron sheets ensuring the field is less than 2mT across the HPDs. This allows accurate detection of light created within the RICH detectors. The rings of light collected by the RICH detectors when combined with information about it's momentum from the tracking stations realise the particles mass and therefore it's identity. Figure 3.14 shows how the Cherenkov angle and momentum can be combined to identify different types of particles in the RICH 1 detector, there are distinct bands for each particle mass. Figure 3.13 shows what is expected for the different radiators.

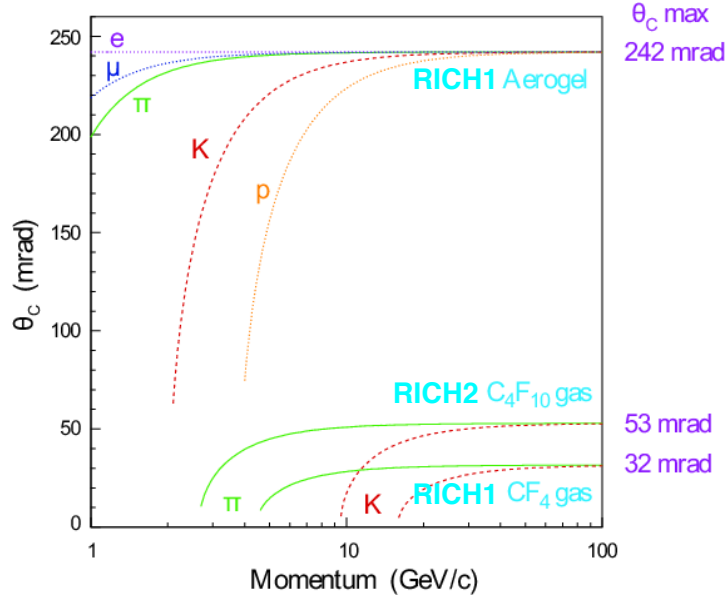


Fig. 3.13 Expected Cherenkov angles produced by different particles travelling through the different radiators in the RICH detectors [3].

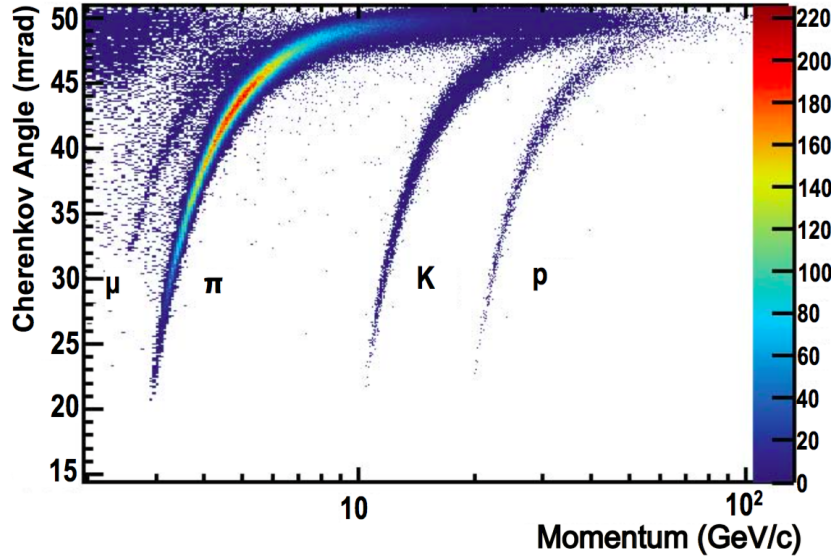


Fig. 3.14 Cherenkov angles for isolated tracks as a function of momentum in the RICH1 detector for 2011 data [8].

3.2.2.2 Calorimeters

The calorimeter system consists of the Scintillating Pad Detector (SDP), Pre-Shower (PS), electromagnetic calorimeter (ECAL) and the hadronic calorimeter (HCAL). The main purposes of the calorimeters are to identify electrons, photons and hadrons with high transverse momentum to be used in the first level of the trigger the L0, and also to help with the reconstruction and identification of these particles. The ECAL is the only part of the LHCb detector that measures the position and energy of photons and neutral pions.

The calorimeters in LHCb are sampling calorimeters that consist of layers of lead absorbers and scintillating material. In lead, incident particles create showers of secondary particles, the charged particles produced in the absorbers create light as they pass through the scintillators. The light travels through wavelength shifters where it is collected by photon multiplier tubes and turned into an electrical signal. In the ECAL showers are started by ionisation, bremsstrahlung radiation or pair production depending on the energy of the incident particle and whether it is a e^\pm or a photon. In the HCAL it is interaction via the strong force that leads to showers of secondary particles. The showers produced in the calorimeters are along the direction of flight of the incident particle. Unlike other sub-detectors in LHCb, the calorimeters change the particle as it moves through the detector in order to measure the energy.

The SPD, PS and ECAL identify electrons, positrons and photons. The SPD is a layer of scintillating material at the start of the calorimeter system, it separates electron and photon showers created later in the calorimeter because only charged particles will produce light in the SPD. Next in the calorimeter system is the PS, it consists of a lead absorber followed by another scintillator similar to the SPD, the length of the lead absorber is chosen so that electrons will start showers in the absorber but charged pions will not. There is only a 1% chance of a pion creating shower in the PS. Information collected by the PS enables showers created by pions in the ECAL to be separated from those created by electrons and positrons. The ECAL is designed to contain the entire shower of high energy photons so that it can provide good energy resolutions of photons passing through the detector. The ECAL has an energy resolution of $\delta E/E = 9\%/\sqrt{(E)} \oplus 0.8\%$ provided information from the PS and SPD are used.

The HCAL is predominately designed for use in the trigger and there is no requirement that the HCAL contains the full hadronic showers, therefore it was designed with a lower energy resolution of $\delta E/E = 69\%/\sqrt{(E)} \oplus 9\%$.

3.2.2.3 Muon Stations

The muons stations are designed to identify highly penetrating muons, for use in the trigger and offline analyses. Muons are produced in made b -hadron decays, good muon identification is necessary trigger events containing muons and to distinguish topologically similar decays such as $B_{(s)}^0 \rightarrow \mu^+ \mu^-$, $B^0 \rightarrow K^+ \pi^-$, $B_s^0 \rightarrow K^+ K^-$ and $B_s^0 \rightarrow K^+ \pi^-$ in physics analyses. Compared to other particles muons have a high penetrating power due to their relatively large mass and because muons do not interact via the strong force, these properties are exploited in the muon detectors.

There are 5 muon stations, M1-5, shown in Figure 3.15 that track and identify highly penetrating muons. The first muon station is located before the calorimeters, the inner section where the fluence is greatest, is made of gas electron multiplier foils and the outer section is made from multiwire proportional chambers (MWPCs). Stations M2-5 are located after the HCAL, by which point most other particles have been absorbed by the calorimeters. These stations are made from MWPC and between each station is 80cm of lead absorber ensuring only highly penetrating muons pass through the muon detector. A muon must have a momentum of at least 3 GeV/c to pass through the calorimeters and M2 and M3, to travel through all the muons stations a muon must have a momentum of 6 GeV/c. The first 3 stations have a high spatial resolution and provide track and transverse momentum information to be used the the

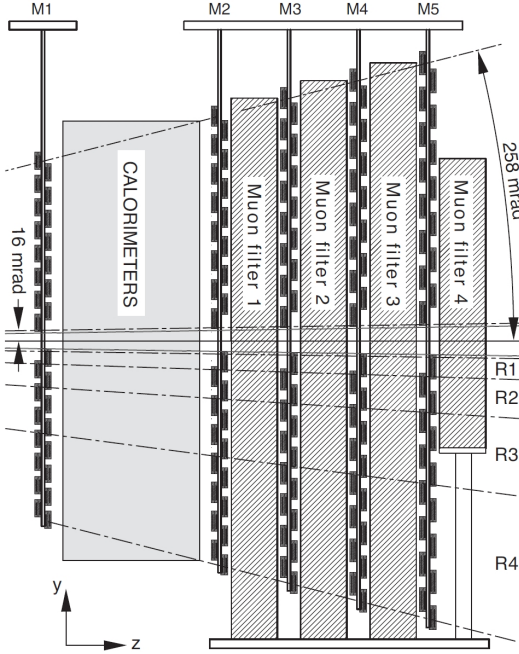


Fig. 3.15 Layout of the muon stations [3].

trigger. M1 is located before the calorimeters to improve the transverse momentum measurement of the muons. The last two stations have lower spatial resolution and are designed to identify highly penetrating muons. After the muon stations there is an iron wall to stop any particles from travelling downstream of the detector. The size of the muon stations increases with distance from the interaction point to ensure the full angular acceptance of the detector is covered. Tracking information collected in the muon stations can be used in the trigger because the station lie outside the magnetic field which allows for fast reconstruction of the tracks and a muons.

3.2.2.4 PID information and performance

The information collected in the PID detectors is combined to provide several discriminating variables that can be used to identify muons, protons, kaons, pions and electrons.

The muon stations are used, along with information from the tracking system, to produce a binary selection (`isMuon`) to identify muons. The tracking system is used to extrapolate a field of interest within the muon stations, a muon is identified if hits in the muon stations can be combined with those from the tracking system within the field of interest. The number of the hits required in the muon stations depends

on the momentum of the muon. Muons with momentum in the range $3 < p < 6$ GeV must leave hits in M2-3, those in the momentum range $6 < p < 10$ muon leave hits in M2-3 and either M4 or M5 and finally muons with momentum above 10 GeV must be observed in all the muon stations. Figure 3.16 shows the efficiency for the isMuon selection at selecting muons and hadron mis-identification probabilities. The mis-ID rate is higher for lower momentum particles, which is expected given there are less hits in the muons detectors. The main contribution is the misidentifying particles as muons comes from the kaons and pions that decay in flight, the muons from these decays are then detected in the muon stations.

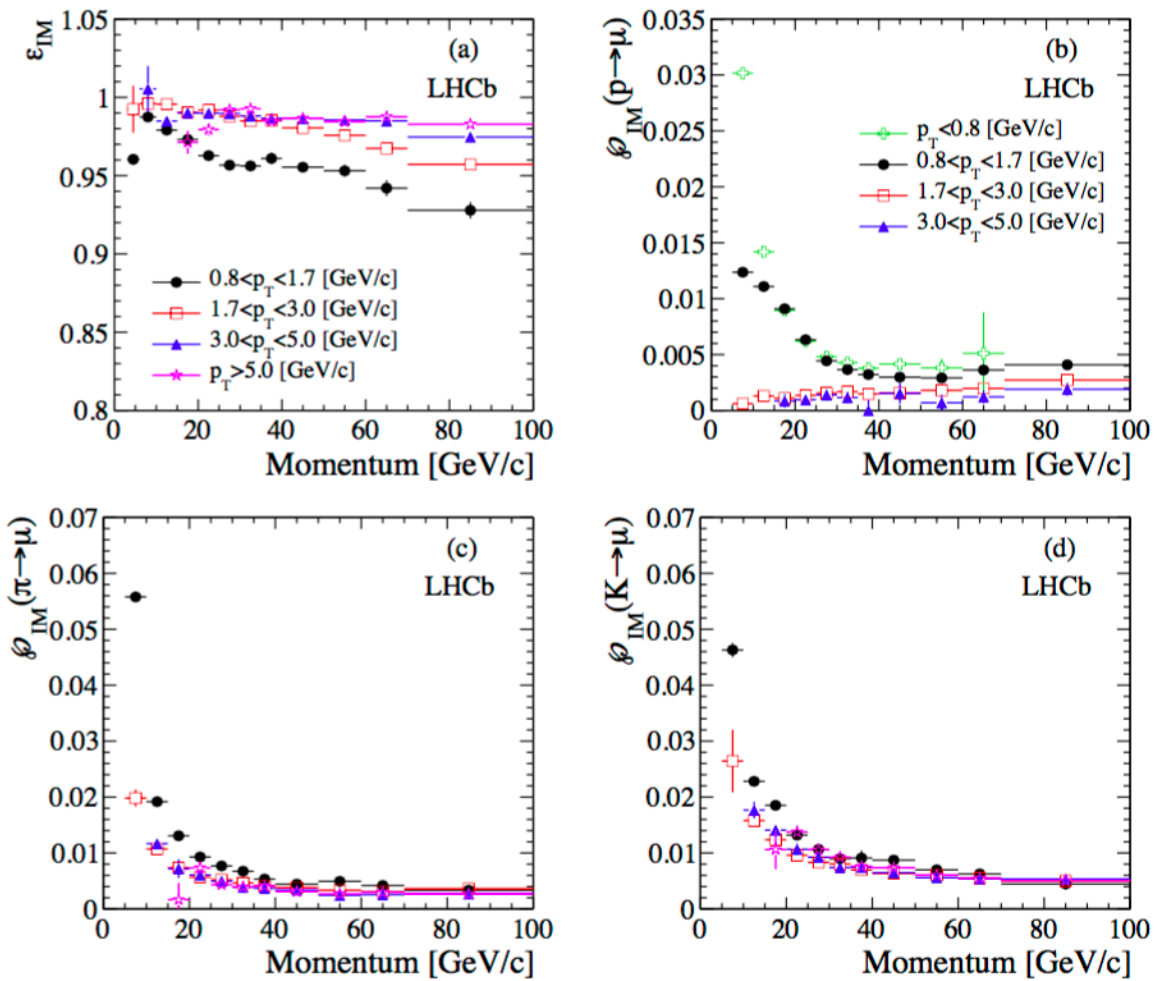


Fig. 3.16 Muon efficiency (top left) and misidentification probabilities for protons (top right), pions (bottom left) and kaons (bottom right) for isMuon criteria [9].

The information from all the PID detectors is combined using two different methods to provide global particle identification variables. One method is based on likelihood

fits and the other is based on Neural Networks. In the first method, likelihood fits are performed in each sub-detector comparing each charged particle track to different particle hypotheses. The information from the likelihood fits in each sub detector are combined into a global variable. The final variable is the difference in the log - likelihoods between the track corresponding to a pion and a different particles hypothesis (kaon, proton, muon, electron), it gives a measure of how likely each particle hypothesis is compared to a pion. These variables are known as DLL variables where the difference in log - likelihoods between the track corresponding to a pion and a kaon would be given by $DLL_{K\pi}$ etc.

The second method uses information from the PID detectors and the tracking system in Neural Networks to provide a global probability of a track having a particular particle hypothesis. This method takes into account correlations between detector systems and extra detector information that are not considered in the likelihood method. The Neural Networks are trained on simulated inclusive b decays and can be tuned to suit different situations, such as the data taking year. The variables produced by the Neural Networks are known as ProbNN variables where the probabiltiy of a particle being a muon is given by $ProbNN\mu$ and the probabiltiy of a particle being a pion is given by $ProbNN\pi$ etc.

Figure 3.17 shows a comparison of the performance of the DLL and ProbNN variables in selecting protons and muons. Although the performance to the two types of variables are quite different, the efficiencies of each variable varies with different kinematic properties of the decay. The most appropriate PID variable type to use depends on the physics analysis it is being used in.

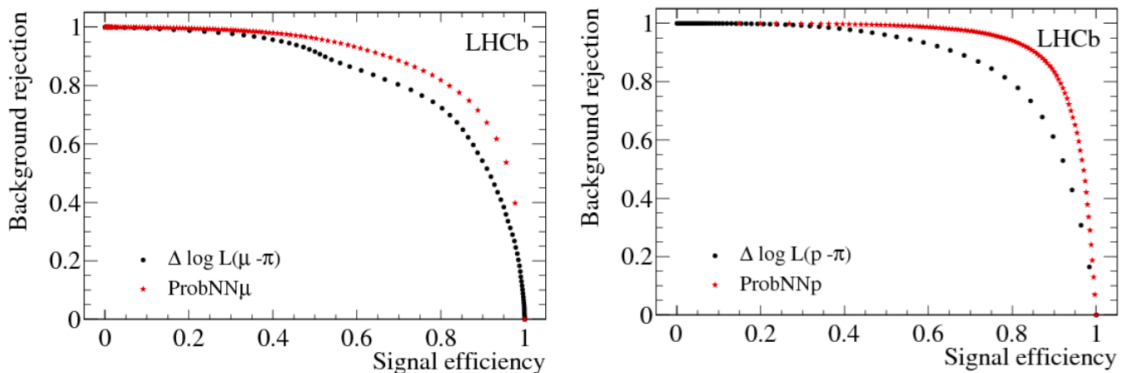


Fig. 3.17 Muon (left) and proton (right) signal efficiency vs background rejection for DLL and ProbNN PID variables [3].

3.2.3 The Trigger

The LHC was designed to collide protons at a rate of 40 MHz, this rate is too high for information to be read out of the LHCb detector. However most pp collisions do not produce particles within the detector acceptance that are interesting for physics analyses at LHCb. A trigger system is used that selects potentially interesting events to be saved for later physics analysis. The trigger has been designed to select interesting physics events with a high efficiency whilst reducing the event rate to one where information from the full detector can be read out. There are two levels to the LHCb trigger; the hardware trigger and the software trigger. The hardware trigger is known as the level-zero (L0) trigger and reduces the 40 MHz event rate to 1 MHz at which the full detector can be read out. The software trigger is known as the High-Level-Trigger (HLT), it has two stages and runs on the output of the L0 further reducing the event rate by utilising information for all the detector sub-systems. Each level of the trigger is composed of trigger ‘lines’; these lines are made up of reconstruction and selection algorithms and either accept or reject each event. Only events that are accepted by a trigger line at both the L0 and HLT are available for use in physics analyses.

3.2.3.1 The L0 trigger

The L0 trigger runs synchronously to the LHC bunch crossing. Its purpose is to reduce the event rate to 1 MHz, where information from the full detector can be read out. Therefore the L0 is limited to use information from the detector that can be read at the same rate as the LHC collision rate. The L0 uses information from 3 parts of the detector, the VELO, calorimeters and the muon stations, to make decisions about the relevance of each event.

The pileup veto stations in the VELO are used in L0 pileup trigger lines, these lines identify the number of collisions in an event and are predominantly used for luminosity measurements [10].

The other L0 trigger lines are based on the kinematic properties of b -hadron decays. The heavy masses of b -hadrons means that their decays are characterised by the production of daughter particles with large transverse momentum (p_T) and transverse energy (E_T). The calorimeters are used in trigger lines that select events containing high E_T electrons, photons or hadrons. Information from the PS, SPD, ECAL and HCAL is used to identify electrons, photons and hadrons in each event. Events are then accepted by the trigger lines if there is an electron, photon or hadron with E_T above a threshold value provided the event multiplicity is not too high. The E_T thresholds

are different for each particle type. Events with high multiplicity take a long time to reconstruct and process in the HLT, therefore it is not efficient to keep these events. The multiplicity is measured by the number of hits in the SPD detector (nSPD), only events with nSPD lower than a specified value can pass an L0 trigger line.

In a similar way to the calorimeters, the muon stations are used to identify muons with high p_T for trigger lines. There are two L0 trigger lines for muons that accept events based on muon p_T if either a single muon has a p_T above a threshold value or if the two muons with this highest p_T have $\sqrt{p_{T1} \times p_{T2}}$ above a threshold value, provided the event multiplicity is not too high.

The E_T and p_T thresholds and the multiplicity limit for the L0 trigger lines vary for each year of data taking depend on the bandwidth available for the trigger.

3.2.3.2 The HLT trigger

Events that are accepted by trigger lines in the L0 are moved to the Event Filter Farm where the HLT is run. The HLT is a software trigger that is split into two levels that are run successively.

The HLT1 is the first level of the HLT. It runs on the output of the L0 checking the decisions made by the L0 trigger lines and reducing the event rate. Time constraints in the HLT1 do not allow for full event reconstruction using all LHCb sub-detectors, instead the HLT1 runs reconstruction and selection algorithms on event information from the VELO and tracking stations. These trigger lines are composed of generic selection criteria, making decisions that confirm those made in the L0 about particular particle types and also identify generic types of particle decays such as inclusive b -hadron decays. The second level of the HLT, HLT2, runs on the output of the HLT1 which provides an event rate that is low enough to allow event reconstruction that includes all detector subsystems. The trigger lines in the HLT2 are designed to select decays relevant to specific physics analyses or particle decay topologies, this is made possible by detailed information from the reconstruction.

Just like the L0 trigger, trigger lines in the HLT vary for each year of data taking both the selection criteria used in the lines and also new trigger lines are introduced. The number of HLT2 lines increases with each year of data taking as understanding of the capabilities of the experiment increases; there were about 100 HLT2 lines in 2011, 200 in 2012 and 450 in 2015. Furthermore, significant changes were made in the reconstruction used in the HLT between Run 1 and Run 2, the details of the changes made can be found in [11]. The majority of the changes to the HLT for Run 2 are not relevant for the analysis discussed in this thesis, the overall impact is that a more

detailed reconstruction is used in the decisions of the Run 2 HLT lines compared to Run 1.

3.2.3.3 Trigger Decisions

The trigger lines in the L0 and HLT return three different types of decisions that are used to classify events. The choice of which type of trigger decision to use depends on the particular physics analysis and the signal decay of interest, the decisions can either be used line by line or as global decisions taking all lines together. The different decisions are:

- **TOS**, ‘triggered on signal’, tracks and hits that make up signal candidate of a physics analysis are sufficient for the event to pass the trigger line.
- **TIS**, ‘triggered independant of signal’, if the tracks and hits associated with the signal candidate of a physics analysis are removed from the event, other tracks and hits would still cause the event to pass the trigger line.
- **Dec**, refers to whether the event was accepted by the trigger line.

3.2.4 LHCb Software and Simulation

The data that is read out of the LHCb experiment needs further processing before it can be used in physics analyses. The GAUDI framework [12] is a C++ framework that is the basis for the software applications needed to process the data at LHCb [13]. This framework ensures that the necessary software is available to all users and changes to the software are implemented across all applications, it is suited to the distributed computing system used in LHCb [14].

Once events have been accepted by the trigger, the first step in processing the output of the detector is reconstructing events, this is done by the BRUNEL application. It takes the digitised detector read out and reconstructs hits in the tracking stations to find particle trajectories and momenta and combines information from the RICH detectors, calorimeters and Muon Stations to compute PID variables. The output of processing by the BRUNEL application are stored in ‘Data Summary Type’ (DST) files.

Next the DAVINCI application is used to fit the tracks reconstructed in BRUNEL with primary and secondary vertices. This application assigns particle hypotheses to each track and reconstructs the decay trees of particles in the detector, computing the kinematic properties that are needed for physics analyses. The the reconstructed output of the trigger is too large to be stored in one place and to be used by all the analysts

therefore a ‘stripping’ procedure is used to break up the data into a manageable size for physics analyses. Each physics analysis designs a set of loose selection requirements, called stripping lines, specific to their decays of interest, the selections are applied centrally to the reconstructed events and are designed to keep as much of the signal as possible but reduce the number background events. Only events that pass a stripping line selection are available to be used in physics analyses. The output of this process are smaller DST files, events passing the stripping selections can either be saved with the full event information or with just the tracks related to the signal candidate. The choice depends on the physics process the stripping line is relevant for. The stripping selection is run a limited number of times and is applied separately to data collected in different years. Requirements are imposed on the amount of data each stripping line can retain; typically the output of a line must be less than 0.05 % of the original data set size if the full event information is saved. Each analyst then uses the DaVinci application one last time to produce ROOT [15] files from the output of their stripping lines, these files display the data in histogram and are used for physics analyses.

As well as data collected by the experiment, simulated data that mirrors what is expected in the experiment is needed to understand the detector performance and for physics analyses. There is a set of software applications that are dedicated to the production of Monte Carlo simulated events within the GAUDI framework. Events are generated using the GAUSS application [16, 17], this package uses PYTHIA [18, 19] to model proton-proton collisions and the production of particles, then the EVTGEN [20] application to calculate the decays of these particles. Final state radiation is modelled using PHOTOS [21]. Both PYTHIA and EVTGEN have been tuned for the production and decay of particles within the LHCb detector. In the simulation the type of particles generated and how they decay can be specified so that the simulated events are relevant to particular physics decays. The detector response to the simulated events is processed by the BOOLE application which uses GEANT4 [22, 23] to model the detector. The output is a digitised response of the detector which is then processed by BRUNEL and DAVINCI in the same way as the real data to produce ROOT files that are used in physics analyses.

The LHCb software framework is set up so that it can be used on the Worldwide LHC Computing Grid [24, 25], the Grid is made up of computers across the world that each store part for the LHCb data set and simulation data. Despite the stripping process the data produced at LHCb is too large to be stored in one place. The DIRAC [26] system manages grid sites and the GANGA project allows the submission analysis code to different grid sites. The grid enables analysts to process and study

the large amounts of data produced by LHCb without having to store the data where the analyst is.

3.2.5 LHCb data collected so far

The data taking periods of the LHC can be split up into different ‘Runs’ which are separated by Long Shut Down periods when maintenance and upgrades are performed on the LHC, the detectors and the accelerator chain that delivers protons to the LHC. Run 1 began in 2010 and ended in 2013, during this Run the LHC operated at two different centre-of-mass energies. In 2010 and 2011 the LHC delivered proton collisions at a centre-of-mass energy of 7 TeV, this was increased to 8 TeV in 2012. The luminosity recorded by LHCb in each was; 0.04 fb^{-1} in 2010, 1.10 fb^{-1} in 2011 and 2.08 fb^{-1} in 2012. After Run 1 the LHC and experiment entered the Long Shutdown 1 (LS1) when the machine and experiments were prepared to deliver and detect proton collisions at $\sqrt{s} = 13$. Run 2 began in early 2015 and is still on going, so far LHCb has recorded 0.32 fb^{-1} in 2015 and 1.67 fb^{-1} in 2016 both at a centre-of-mass energy of 13 TeV. Figure 3.18 shows the integrated luminosity collected by LHCb in each year of data taking. The recorded luminosity of Run 2 is currently less than what was recorded in Run 1, however the production cross section for b -hadrons approximately doubled with the increase in centre-of-mass energy between Run 1 and Run 2 therefore the Run 2 data set will already contain more b -hadrons useful for physics analyses than the Run 1 data set.

The expected end of Run 2 is 2018 by which time LHCb is expected to have recorded 5 fb^{-1} luminosity during the Run. Run 2 will be followed by a second long shut down period (LS2) in which LHCb shall be upgraded ready to record proton collisions at 14 TeV during Run 3. This run of data taking is expected to be from 2021 - 2024 and by the end of Run 3 LHCb is expected to have collected an integrated luminosity of 23 fb^{-1} over all the runs.

The physics analysis described in this thesis uses the full data sets from Run 1 and 2015 and data taken up to September during 2016. The 2016 data set is therefore reduced to 1.1 fb^{-1} .

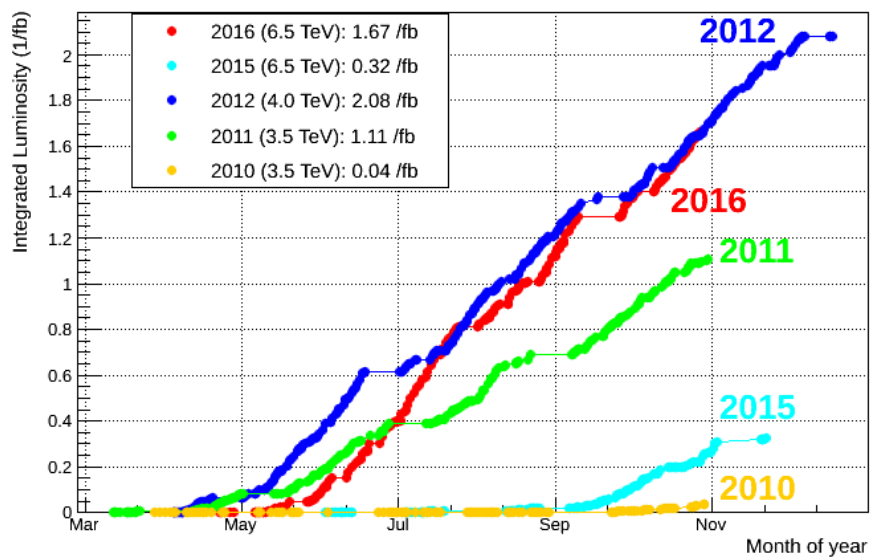


Fig. 3.18 Integrated luminosity collected by the LHCb experiment in each year of data taking. Source: LHCb.

Chapter 4

Event Selection

Chapter 5

Measurement of $B_{(s)}^0 \rightarrow \mu^+\mu^-$ Branching Fractions

This chapter presents the measurements of the $B^0 \rightarrow \mu^+\mu^-$ and $B_s^0 \rightarrow \mu^+\mu^-$ branching fractions. Section 5.1 gives an overview of the analysis strategy and a description of how the $B_{(s)}^0 \rightarrow \mu^+\mu^-$ yield is extracted from the data is given in Section 5.2. The estimation of the background decays present in that data set is detailed in Section 5.3 and the normalisation procedure to convert the number of observed $B_{(s)}^0 \rightarrow \mu^+\mu^-$ decays in to the branching fractions for these decays is explained in Section 5.4. Finally the results are presented in Section 5.5.

The work presented in this Chapter was performed by the $B_{(s)}^0 \rightarrow \mu^+\mu^-$ LHCb analysis group and is published here []. My contribution was maintaining the stripping selection used for this analysis and providing the ROOT files for contained the data and simulated events needed for the analysis development and measurements.

5.1 Analysis Strategy

The $B_{(s)}^0 \rightarrow \mu^+\mu^-$ branching fractions, $\mathcal{B}(B_{(s)}^0 \rightarrow \mu^+\mu^-)$, are defined as the ratio of $B_{(s)}^0 \rightarrow \mu^+\mu^-$ decays to the number of $B_{(s)}^0$ mesons created. However in reality not every $B_{(s)}^0 \rightarrow \mu^+\mu^-$ decay produced in pp collisions will be within the LHCb detector acceptance or be reconstructed and pass the selection criteria of Chapter 4. Therefore the number of observed $B_{(s)}^0 \rightarrow \mu^+\mu^-$ decays at LHCb is reduced by the efficiency, ϵ , of the detector, reconstruction and selection. The $B_{(s)}^0 \rightarrow \mu^+\mu^-$ branching fractions

can be given by

$$\mathcal{B}(B_{(s)}^0 \rightarrow \mu^+ \mu^-) = \frac{\mathcal{N}_{B_{(s)}^0 \rightarrow \mu^+ \mu^-}}{\mathcal{N}_{B_{(s)}^0}} = \frac{\mathcal{N}_{B_{(s)}^0 \rightarrow \mu^+ \mu^-}^{obs}}{\mathcal{N}_{B_{(s)}^0}^{obs}} \quad (5.1)$$

where $\mathcal{N}_{B_{(s)}^0 \rightarrow \mu^+ \mu^-}(B_{(s)}^0)$ is the total number of $B_{(s)}^0 \rightarrow \mu^+ \mu^-$ decays ($B_{(s)}^0$ mesons) and $\mathcal{N}_{B_{(s)}^0 \rightarrow \mu^+ \mu^-}^{obs}$ the number of observed $B_{(s)}^0 \rightarrow \mu^+ \mu^-$ decays.

The number of $B_{(s)}^0$ created can be calculated from the integrated luminosity, \mathcal{L}_{int} , and the $b\bar{b}$ production cross-section, $\sigma_{b\bar{b}}$, via

$$\mathcal{N}_{B_{(s)}^0} = 2 \times \mathcal{L}_{int} \times \sigma_{b\bar{b}} \times f_{d(s)} \quad (5.2)$$

where $f_{d(s)}$ is the hadronisation factor, giving the probability for a b or \bar{b} quark to form a B^0 (B_s^0) or a \bar{B}^0 (\bar{B}_s^0). The factor of 2 arises because no distinction is made between the $B_{(s)}^0$ and the \bar{B}_s^0 . Although the number of $B_{(s)}^0$ can be computed this way the measured cross-section is not precisely known. Therefore to achieve a more precise branching fraction measurement an alternative approach is used. Another decay with a well known branching fraction is used to normalise the observed number of $B_{(s)}^0 \rightarrow \mu^+ \mu^-$ decays and obtain the branching fractions. The extraction of $\mathcal{B}(B_{(s)}^0 \rightarrow \mu^+ \mu^-)$ from the number of observed decays is therefore

$$\begin{aligned} \mathcal{B}(B_{(s)}^0 \rightarrow \mu^+ \mu^-) &= \frac{1}{\mathcal{B}_{norm}} \cdot \frac{f_{norm}}{f_{d(s)}} \cdot \frac{\epsilon_{norm}}{\epsilon_{B_{(s)}^0 \rightarrow \mu^+ \mu^-}} \cdot \frac{\mathcal{N}_{B_{(s)}^0 \rightarrow \mu^+ \mu^-}^{obs}}{\mathcal{N}_{norm}^{obs}} \\ &= \alpha_{d(s)} \cdot \mathcal{N}_{obs B_{(s)}^0 \rightarrow \mu^+ \mu^-} \end{aligned} \quad (5.3)$$

where *norm* indicates the normalisation channel. The normalisation factors can be combined into one normalisation parameter $\alpha_{d(s)}$ for each of the B_s^0 and B^0 decays. The normalisation procedure removes the uncertainty from $\sigma_{b\bar{b}}$. Therefore the number of observed $B_{(s)}^0 \rightarrow \mu^+ \mu^-$ decays and the normalisation parameters, $\alpha_{d(s)}$, need to be evaluated to measure the branching fractions. The selection described in Chapter 4 allows $B_{(s)}^0 \rightarrow \mu^+ \mu^-$ candidates to be classified by their dimuon invariant mass and global BDT output. A simultaneous unbinned maximum likelihood fit is performed to the dimuon invariant mass distribution in 4 BDT bins to measure the observed number of $B^0 \rightarrow \mu^+ \mu^-$ and $B_s^0 \rightarrow \mu^+ \mu^-$ decays. The Run 1 and Run 2 data are kept separate and the fit is applied simultaneously to both data sets. To measure the number of $B_{(s)}^0 \rightarrow \mu^+ \mu^-$ decays knowledge is required of the mass shapes and the fraction of $B_{(s)}^0 \rightarrow \mu^+ \mu^-$ decays in each BDT bin and the number of background decays and their

mass shapes in each bin. The mass shapes and fraction of $B_{(s)}^0 \rightarrow \mu^+ \mu^-$ decay in each BDT bin are described by probability density functions (*pdfs*). The evaluation of the $B_{(s)}^0 \rightarrow \mu^+ \mu^-$ mass *pdfs* and the fraction of decays in each BDT bin are described in Section 5.2. The expected number of background decays and their mass *pdfs* in each BDT bin are described in Section 5.3.

The binning choice used for the BDT is chosen to optimise both fit stability and sensitivity to the $B_{(s)}^0 \rightarrow \mu^+ \mu^-$ branching fractions. The bin boundaries used are

$$[0.25, 0.4, 0.5, 0.6, 1.0]. \quad (5.4)$$

Candidates with BDT values between 0 and 0.25 are not included in the fit because this bin is dominated by backgrounds from random combinations of muons in the event. The inclusion of this bin does not improve the branching fraction sensitivity and reduces the stability of the fit.

The normalisation decay is chosen to be as similar as possible to $B_{(s)}^0 \rightarrow \mu^+ \mu^-$ decays to reduce systematic uncertainties introduced by different detection and selection efficiencies between signal and normalisation decays. Furthermore the chosen decay needs to be abundant so the precision of the $B_{(s)}^0 \rightarrow \mu^+ \mu^-$ branching fraction measurements are not limited by the statistics available for the normalisation channel and it must have a precisely measured branching fraction, which is likely for abundant decays. Two decays are chose as normalisation channels; $B^+ \rightarrow J/\psi K^+$ where $J/\psi \rightarrow \mu^+ \mu^-$ and $B^0 \rightarrow K^+ \pi^-$. Both decays have large, precisely measured branching fractions and are similar to $B_{(s)}^0 \rightarrow \mu^+ \mu^-$ decays in complementary ways. The $B^+ \rightarrow J/\psi K^+$ decay has a very similar trigger efficiency to $B_{(s)}^0 \rightarrow \mu^+ \mu^-$ decays, due to the two muons from the J/ψ , but the extra particle in the final state leads to different selection and reconstruction efficiencies. The $B^0 \rightarrow K^+ \pi^-$ decay has a very similar topology to $B_{(s)}^0 \rightarrow \mu^+ \mu^-$ therefore the selection and reconstruction efficiencies will be similar, but the trigger efficiencies for hadrons is quite different compared to muons.

The normalisation factors $\alpha_{d(s)}$ for $B^0 \rightarrow \mu^+ \mu^-$ and $B_s^0 \rightarrow \mu^+ \mu^-$ decays are evaluated independently for each normalisation channel and year of data taking, the factors are combined to produce an overall normalisation factor for Run 1 and Run 2. The evaluation of the normalisation factors is described in Section 5.4.

5.2 $B_s^0 \rightarrow \mu^+ \mu^-$ mass and BDT *pdfs*

5.2.1 Mass *pdfs*

The mass *pdfs* for $B^0 \rightarrow \mu^+ \mu^-$ and $B_s^0 \rightarrow \mu^+ \mu^-$ decays are modelled by a Crystal Ball function [27]. A Crystal Ball function is a Gaussian function that has an exponential tail on the low mass side to model radiative energy loss in the final state. The parameters defining the function are the mean, μ , and resolution, σ of the Gaussian, the slope of the exponential, n , and a parameter α , defined in terms of σ , that determines the transition point between the Gaussian and the exponential function.

The parameters are evaluated using different methods:

- μ - the means of B^0 and B_s^0 decays are evaluated separately from a fits to $B^0 \rightarrow K^+ \pi^-$ and $B_s^0 \rightarrow K^+ K^-$ decays in data
- σ - the resolution is extrapolated from the resolutions of quarkonia resonances. The resolutions for the J/ψ , $\Psi(2S)$ and $\Upsilon(1, 2, 3S)$ decaying into two muons are measured from a fits to data. The B^0 and B_s^0 resolutions are then extrapolated from the observed relationship between quarkonia mass and resolution.
- n and α - these parameters are evaluated from the mass spectrum of $B^0 \rightarrow \mu^+ \mu^-$ and $B_s^0 \rightarrow \mu^+ \mu^-$ simulated decays where the mass distributions are smeared to have the same resolution as that measured from the quarkonia decays in data.

All parameters are evaluated separately for the B^0 and B_s^0 for each year of data taking. The resulting parameter values are in good agreement across each year in the Run 1 and Run 2 data sets. The weighted average of the yearly parameters is used to produced the mass *pdfs* for Run 1 and Run 2 and are given in Tables 5.1 and 5.2 .

Parameter	$B^0 \rightarrow \mu^+ \mu^-$	$B_s^0 \rightarrow \mu^+ \mu^-$
$\mu/\text{MeV}/c^2$	$5284.73 \pm 0.15_{\text{stat}} \pm 0.27_{\text{syst}}$	$5372.05 \pm 0.16_{\text{stat}} \pm 0.36_{\text{syst}}$
$\sigma/\text{MeV}/c^2$	$22.68 \pm 0.05_{\text{stat}} \pm 0.39_{\text{syst}}$	$23.07 \pm 0.05_{\text{stat}} \pm 0.39_{\text{syst}}$
n	1.141 ± 0.026	1.156 ± 0.013
α	2.054 ± 0.013	2.053 ± 0.007

Table 5.1 Parameter values for Crystal Ball functions used to describe the $B_{(s)}^0 \rightarrow \mu^+ \mu^-$ mass *pdf* for Run 1.

Parameter	$B^0 \rightarrow \mu^+ \mu^-$	$B_s^0 \rightarrow \mu^+ \mu^-$
$\mu/\text{MeV}/c^2$	$5279.95 \pm 0.13_{\text{stat}} \pm 0.08_{\text{syst}}$	$5367.34 \pm 0.14_{\text{stat}} \pm 0.35_{\text{syst}}$
$\sigma/\text{MeV}/c^2$	$22.46 \pm 0.08_{\text{stat}} \pm 0.41_{\text{syst}}$	$22.85 \pm 0.08_{\text{stat}} \pm 0.42_{\text{syst}}$
n	1.118 ± 0.014	1.110 ± 0.017
α	2.063 ± 0.007	2.062 ± 0.008

Table 5.2 Parameter values for Crystal Ball functions used to describe the $B_{(s)}^0 \rightarrow \mu^+ \mu^-$ mass *pdf* for Run 2.

5.2.2 BDT *pdfs*

The global BDT distribution for $B_{(s)}^0 \rightarrow \mu^+ \mu^-$ decays is expected to be uniform between 0 and 1 as designed by the flattening procedure described in Section ???. The fraction of $B_{(s)}^0 \rightarrow \mu^+ \mu^-$ decays in a BDT bin should simply be proportional to the bin width. However the global BDT was trained and flattened using simulated decays, therefore to avoid differences between simulated decays and data affecting the expected fraction of $B_{(s)}^0 \rightarrow \mu^+ \mu^-$ decays in each BDT bin, the BDT *pdf* is evaluated from data. This process is known as the BDT calibration. The global BDT is designed to use only kinematic and geometric information to classify candidates and includes no PID information. Therefore the BDT distributions of $B \rightarrow h^+ h^-$ decays will be the same as $B_{(s)}^0 \rightarrow \mu^+ \mu^-$ decays. $B^0 \rightarrow K^+ \pi^-$ decays are used to calibrate the BDT response because it is the most abundant $B \rightarrow h^+ h^-$ decay.

The number of $B^0 \rightarrow K^+ \pi^-$ decays is extracted from data using maximum likelihood fits in each BDT bin for each year of data taking. The $B^0 \rightarrow K^+ \pi^-$ candidates must pass the standard $B \rightarrow h^+ h^-$ selection in Table ?? and are separated from other $B \rightarrow h^+ h^-$ modes using $\text{DLL}_{K\pi}$ variable. To reduce the difference in the trigger efficiency between and $B_{(s)}^0 \rightarrow \mu^+ \mu^-$ decays, $B^0 \rightarrow K^+ \pi^-$ candidates are required to be TIS at the L0 and Hlt1 but TOS at Hlt2 to ensure enough statistics.

The particle identification and trigger efficiencies are different for $B^0 \rightarrow K^+ \pi^-$ and $B_{(s)}^0 \rightarrow \mu^+ \mu^-$ decays. Therefore the $B^0 \rightarrow K^+ \pi^-$ yields in each BDT bin are corrected for using by the different trigger and particle identification efficiencies. The same calibration is used for $B_s^0 \rightarrow \mu^+ \mu^-$ and $B^0 \rightarrow \mu^+ \mu^-$ decays. The calibration is performed for each year separately then combined to give the Run 1 and Run 2 fractions per BDT bin. Figure 5.1 shows the BDT distribution for $B_{(s)}^0 \rightarrow \mu^+ \mu^-$ decays calibrated with $B^0 \rightarrow K^+ \pi^-$ data for Run 1 and Run 2.

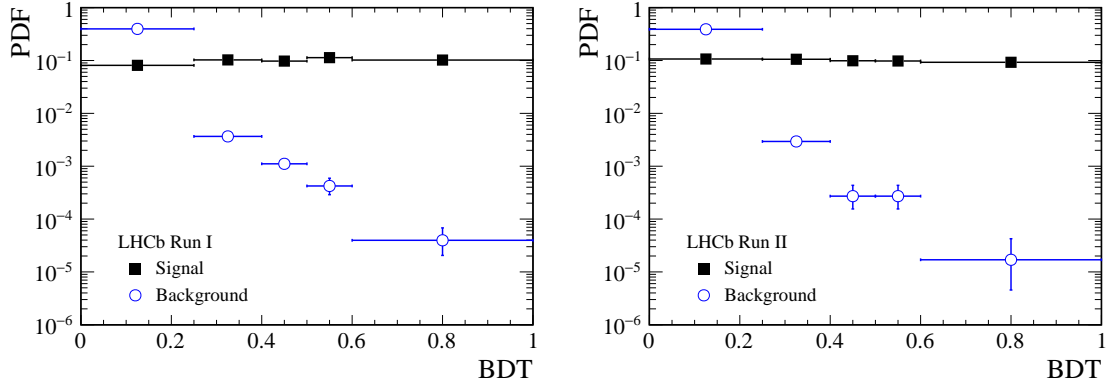


Fig. 5.1 $B_{(s)}^0 \rightarrow \mu^+\mu^-$ BDT *pdfs* (black squares) for Run 1 and Run 2 data calibrated on $B^0 \rightarrow K^+\pi^-$ decay and the combinatorial background decays (blue circles) for $B_{(s)}^0 \rightarrow \mu^+\mu^-$ candidates in data with a dimuon mass above $5477 \text{ MeV}/c^2$.

5.2.3 Decay time dependence of the $B_s^0 \rightarrow \mu^+\mu^-$ BDT *pdf*

The output of the global BDT for $B_{(s)}^0 \rightarrow \mu^+\mu^-$ is correlated with the $B_{(s)}^0 \rightarrow \mu^+\mu^-$ decay time due to the choice of input variables used in the BDT as listed in Section ???. This correlation will lead to slightly incorrect estimations of the $B_s^0 \rightarrow \mu^+\mu^-$ BDT *pdf*. In the Standard Model the $B_s^0 \rightarrow \mu^+\mu^-$ effective lifetime, $\tau_{\mu\mu}$, is equal to the lifetime of the heavy B_s^0 mass eigenstate, τ_H , however in reality $\tau_{\mu\mu}$ could be somewhere in between the lifetimes of the heavy and light mass eigenstates. As described in Chapter (*the Theory Chapter*) the $B_s^0 \rightarrow \mu^+\mu^-$ effective lifetime is related to the parameter $A_{\Delta\Gamma}$, where $A_{\Delta\Gamma} = +1$ for $\tau_{\mu\mu} = \tau_H$ and $A_{\Delta\Gamma} = -1$ for $\tau_{\mu\mu} = \tau_L$, where τ_L is the lifetime of the light $B_s^0 \rightarrow \mu^+\mu^-$ mass eigenstate.

The simulated decays used to train and flatten the global BDT use as the $B_s^0 \rightarrow \mu^+\mu^-$ lifetime the mean of the measured τ_H and τ_L values at the time of production. Therefore the lifetime used is different between simulation versions. Since the BDT output is correlated with the lifetime the fraction of $B_s^0 \rightarrow \mu^+\mu^-$ decays in each BDT bin will depend on the lifetime used in the simulation. Numerical correction factors are computed for each year to scale the fraction of $B_s^0 \rightarrow \mu^+\mu^-$ decays in each BDT bin for the situations where $= -1, 0$ or $+1$, so that the dependence on $A_{\Delta\Gamma}$ of the measured branching fractions can be evaluated.

No corrections are needed for $B^0 \rightarrow \mu^+\mu^-$ because the difference in lifetime of the heavy and light B^0 mass eigenstates is negligible and the need for correction cancels out with the BDT calibration that uses the $B^0 \rightarrow K^+\pi^-$.

5.3 Background mass *pdfs* and expected yields

The selection described in Chapter 4 is effective at reducing the backgrounds in the data set to a suitable level so that number of the $B_{(s)}^0 \rightarrow \mu^+\mu^-$ decays can be measured. However background decays are present in the final data set, these cannot be completely removed without drastically reducing the efficiency to select signal decays. The backgrounds present in the data set must be included in the fit to the dimuon invariant mass in order to accurately measure the $B_{(s)}^0 \rightarrow \mu^+\mu^-$ branching fractions. The backgrounds present in the final data set come from;

- $B \rightarrow h^+h^-$ decays (where $h = K, \pi$) when both hadrons are mis-identified as muons because the hadrons decay during their flight through the detector after leaving the VELO. This background falls within the B^0 mass window but not the B_s^0 mass window¹ due to the missing energy from the undetected neutrino.
- semi-leptonic decays where one hadron is mis-identified as a muon that include;
 - $B^0 \rightarrow \pi^-\mu^+\nu_\mu$ and $B_s^0 \rightarrow K^-\mu^+\nu_\mu$ decays where the final state hadrons are mis-identified as muons. The mass of these backgrounds falls below the B^0 mass window in the left mass sideband
 - $\Lambda_b^0 \rightarrow p\mu^-\nu_\mu$ decays when the proton is mis-identified as a muon. The large mass of the Λ_d means that this background pollutes the B_s^0 and B^0 mass windows and below these windows
- semi-leptonic decays where muons in the decay form a good vertex that include;
 - $B^{0(+)} \rightarrow \pi^{0(+)}\mu^+\mu^-$ decays where the pion is not detected. The missing hadron means that these backgrounds fall well below the B^0 mass window.
 - $B_c^+ \rightarrow J/\psi\mu^+\nu_\mu$ decays where $J/\psi \rightarrow \mu^+\mu^-$. The large mass of the B_c^+ causes this background to cover the full mass range 4900 - 6000 MeV/ c^2
- combinatorial background formed by the random combination of any two muons in the event, this background is distributed across the full mass range

In the fit to the dimuon invariant mass the combinatorial background is modelled by an exponential function. The combinatorial background yield is not constrained in the fit and the slope is constrained to have the same value across all BDT bins for each data set. These parameters are determined from a simultaneous fit to candidates

¹ B^0 and B_s^0 mass windows are defined as ± 60 MeV/ c^2 of the B^0 and B_s^0 masses.

in data in BDT bins for the mass ranges $[4900, (m_{B^0} - 50)]$ MeV/ c^2 and $[(m_{B_0^0} + 60, 6000]$ MeV/ c^2 , where the mass shapes and yields of the remaining backgrounds are constrained. The mass *pdfs* and yields of the background from $B \rightarrow h^+ h^-$ and semi-leptonic decays are constrained in the fit around the expected values. The backgrounds that have lower masses than the B^0 and B_s^0 must be accurately modelled in the fit to ensure the combinatorial background yield, that spans the full mass range, is accurately described within the signal mass windows. The approaches for finding the mass *pdfs* and expected yields differ for $B \rightarrow h^+ h^-$ and semi-leptonic backgrounds, these procedures are described in the following sections.

5.3.1 $B \rightarrow h^+ h^-$ mass and BDT *pdfs*

The mass *pdf* describing mis-identified $B \rightarrow h^+ h^-$ decays is formed of two Crystal Ball functions. The parameter values are evaluated from simulated decays for $B^0 \rightarrow K^+ \pi^-$, $B_s^0 \rightarrow K^+ K^-$, $B^0 \rightarrow \pi^+ \pi^-$ and $B_s^0 \rightarrow K^+ \pi^-$ the momenta of tracks smeared to model the hadrons decaying in flight. The parameters are evaluated separately for each decay and combined using the branching fractions and the particle identification efficiencies for each decay.

The number of mis-identified $B \rightarrow h^+ h^-$ decays in each BDT bin, $\mathcal{N}_{B \rightarrow hh \rightarrow \mu\mu}$, is found using the relationship

$$\mathcal{N}_{B \rightarrow hh \rightarrow \mu\mu} = \epsilon_{B_{(s)}^0 \rightarrow \mu^+ \mu^-}^{TRIG} \cdot \frac{\mathcal{N}_{B \rightarrow hh}}{\epsilon_{B \rightarrow hh}^{TRIG}} \cdot \epsilon_{B \rightarrow hh \rightarrow \mu\mu} \quad (5.5)$$

where $\mathcal{N}_{B \rightarrow hh}$ is the number of TIS $B \rightarrow h^+ h^-$ decays in data, $\epsilon_{B_{(s)}^0 \rightarrow \mu^+ \mu^-, B \rightarrow hh}^{TRIG}$ are the $B_{(s)}^0 \rightarrow \mu^+ \mu^-$ and $B \rightarrow h^+ h^-$ trigger efficiencies and $\epsilon_{B \rightarrow hh \rightarrow \mu\mu}$ is the probability that a $B \rightarrow h^+ h^-$ decays is mis-identified as $B_{(s)}^0 \rightarrow \mu^+ \mu^-$. The number of $B \rightarrow h^+ h^-$ decays triggered as TIS is calculated for the full BDT range from the number of $B^0 \rightarrow K^+ \pi^-$ decays in data corrected for the expected fraction of $B \rightarrow h^+ h^-$ decays it mode occupies. Apart from the trigger and particle identification requirements the same selection is used for $B^0 \rightarrow K^+ \pi^-$ decays as $B_{(s)}^0 \rightarrow \mu^+ \mu^-$, therefore only the trigger and particle identification efficiencies are corrected for. The efficiencies are calculated using a combination of data and simulated decays for each BDT bin and the same BDT *pdf* as $B_{(s)}^0 \rightarrow \mu^+ \mu^-$ decays is assumed for $B \rightarrow h^+ h^-$ decays.

5.3.2 Semi-leptonic mass and BDT *pdfs*

The mass *pdfs* of semi-leptonic backgrounds vary across the BDT range therefore these *pdfs* are evaluated using simulated decays separated into each BDT bin. An Argus function [28] convoluted with an Gaussian Function is used to describe the mass distributions. The shapes of $B^0 \rightarrow \pi^- \mu^+ \nu_\mu$ and $B_s^0 \rightarrow K^- \mu^+ \nu_\mu$ are extremely similar and therefore these backgrounds are modelled with one common *pdf*. Similarly one mass *pdf* is used to model $B^+ \rightarrow \pi^+ \mu^+ \mu^-$ and $B^0 \rightarrow \pi^0 \mu^+ \mu^-$ decays.

The expected yields of the semi-leptonic backgrounds in each BDT bin is estimated by normalising to the number of $B^+ \rightarrow J/\psi K^+$ decays observed via

$$\mathcal{N}_x^{exp} = \mathcal{N}_{B^+ \rightarrow J/\psi K^+} \cdot \frac{f_x}{f_u} \cdot \frac{\mathcal{B}_x}{\mathcal{B}_{B^+ \rightarrow J/\psi K^+}} \cdot \frac{\epsilon_x}{\epsilon_{B^+ \rightarrow J/\psi K^+}} \quad (5.6)$$

where x represents each background decay. The background estimation can be factorised as

$$\mathcal{N}_x^{exp} = \beta \cdot f_x \cdot \epsilon_x \cdot \mathcal{B}_x \quad (5.7)$$

where β combines the background yield, detection and selection efficiency and hadronisation factors of $B^+ \rightarrow J/\psi K^+$ decays, it is the same for all backgrounds. The β term is evaluated using the same method as the normalisation of the $B_{(s)}^0 \rightarrow \mu^+ \mu^-$ branching fractions described in Section 5.4. The efficiencies and yields are evaluated across the full BDT range whereas the detection and selection efficiency of each background, ϵ_x , are evaluated separately for each BDT bin from information from both data and simulated decays. The hadronisation factors and branching fractions are specific to each background and were possible measured, rather than predicted, branching fractions are used.

5.4 Normalisation

As introduced earlier the $B_{(s)}^0 \rightarrow \mu^+ \mu^-$ branching fractions are measured by normalising the number of observed $B_{(s)}^0 \rightarrow \mu^+ \mu^-$ decays to the number of observed $B^+ \rightarrow J/\psi K^+$ and $B^0 \rightarrow K^+ \pi^-$ decays. The normalisation parameters $\alpha_{d(s)}$, in equation 5.3 for $B_{(s)}^0 \rightarrow \mu^+ \mu^-$ decays depend on the yields of the normalisation decays, the ratio of the detection and selection efficiencies and the hadronisation factors. The evaluation of each of these terms are described in the following sections. In addition to the normalisation decay $B_s^0 \rightarrow J/\psi \phi$ decays are used to check to normalisation parameters used to measure the $B_{(s)}^0 \rightarrow \mu^+ \mu^-$ branching fractions therefore the yield of decays

and the detection and selection efficiencies must also be evaluated. This is done in the same way as the normalisation channels.

5.4.1 $B^0 \rightarrow K^+ \pi^-$ and $B^+ \rightarrow J/\psi K^+$ yields

The yields of $B^+ \rightarrow J/\psi K^+$ and $B^0 \rightarrow K^+ \pi^-$ decays, \mathcal{N}_{norm}^{obs} , are calculated from data using maximum likelihood fits to each year of data taking. The $B^+ \rightarrow J/\psi K^+$ mass *pdf* is modelled by an Ipathia function [] and the fit includes components for combinatorial background and $B^+ \rightarrow J/\psi \pi^+$ decays that are mis-reconstructed as $B^+ \rightarrow J/\psi K^+$. The mass *pdf* parameters are determined from both data and simulated decays. The $B^0 \rightarrow K^+ \pi^-$ yields are calculated in the same way at the BDT calibration and the same trigger requirements are used. However for the normalisation the total number of $B^0 \rightarrow K^+ \pi^-$ decays across the full BDT range is needed rather than bin-by-bin yields. Figure 5.2 and 5.3 show the mass fits used to calculate the Run 1 and Run 2 $B^0 \rightarrow K^+ \pi^-$ and $B^+ \rightarrow J/\psi K^+$ yields.

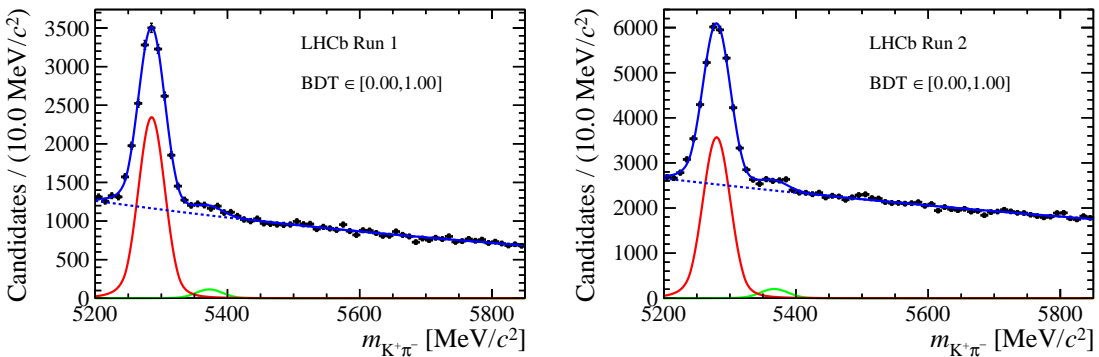


Fig. 5.2 Mass fit to measure $B^0 \rightarrow K^+ \pi^-$ yield for the normalisation for Run 1 (left) and Run 2 (right) data.

5.4.2 Efficiency ratio

The efficiency ratio in equation 5.3 is split into several separate efficiency terms

$$\frac{\epsilon_{norm}}{\epsilon_{B_{(s)}^0 \rightarrow \mu^+ \mu^-}} = \frac{\epsilon_{norm}^{Acc}}{\epsilon_{B_{(s)}^0 \rightarrow \mu^+ \mu^-}^{Acc}} \cdot \frac{\epsilon_{norm}^{RecSel|Acc}}{\epsilon_{B_{(s)}^0 \rightarrow \mu^+ \mu^-}^{RecSel|Acc}} \cdot \frac{\epsilon_{norm}^{Trig|RecSel}}{\epsilon_{B_{(s)}^0 \rightarrow \mu^+ \mu^-}^{Trig|RecSel}} \quad (5.8)$$

for the detector acceptance, ϵ^{Acc} , reconstruction and selection efficiencies, $\epsilon^{RecSel|Acc}$, and the trigger efficiency, $\epsilon^{Trig|RecSel}$.

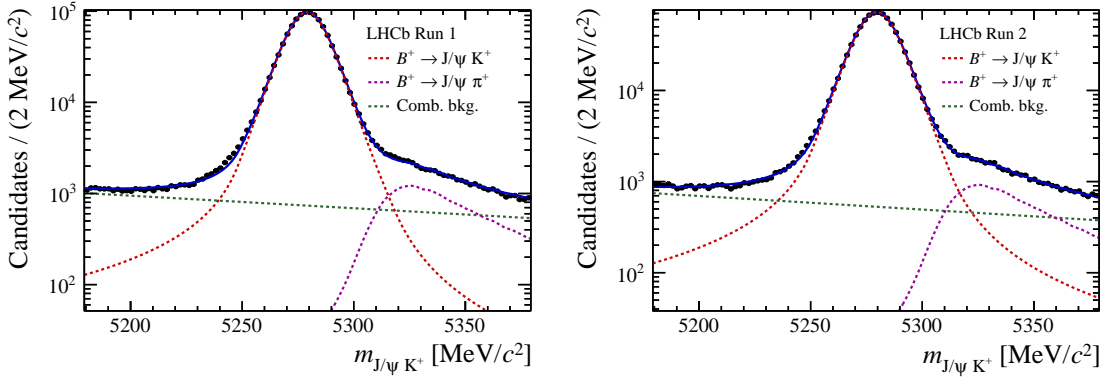


Fig. 5.3 Mass fit to measure $B^+ \rightarrow J/\psi K^+$ yield for the normalisation for Run 1 (left) and Run 2 (right) data.

The detector acceptance efficiency gives the efficiency for the decay products to be within the LHCb detector acceptance. This efficiency is evaluated on simulated decays to for decay products that fall within the range [10,400] mrad. The range is chosen to be slightly larger than the detector acceptance so that particles recovered by the magnetic field are included. To keep this efficiency similar for $B_{(s)}^0 \rightarrow \mu^+ \mu^-$ and $B^0 \rightarrow K^+ \pi^-$ decays, the hadrons from $B^0 \rightarrow K^+ \pi^-$ are required to be within the muon detector acceptance.

The reconstruction and selection efficiencies are calculated as the reconstruction efficiency of decays that are within the detector acceptance and the selection efficiency of reconstructed decays. The selection and reconstruction efficiencies are evaluated from a combination of information from data and simulated decays to ensure accurate selection efficiency ratios. Similar to the fraction of $B_s^0 \rightarrow \mu^+ \mu^-$ in each BDT bin, a correction is applied for the lifetime used in simulated $B_s^0 \rightarrow \mu^+ \mu^-$ decays assuming $A_{\Delta\Gamma} = +1$.

The trigger efficiencies for decays passing the reconstruction and selection are evaluated for each decay by data driven methods as described in ??.

The efficiencies are calculated for $B_s^0 \rightarrow \mu^+ \mu^-$, $B^0 \rightarrow \mu^+ \mu^-$, $B^0 \rightarrow K^+ \pi^-$ and $B^+ \rightarrow J/\psi K^+$ separately to account for difference in the decays and kinematics. The ratio of efficiencies between signal and normalisation channels in the normalisation parameters ensures that systematic uncertainties arising from the use of simulated decays cancel out and will not effect the precision of the $B_{(s)}^0 \rightarrow \mu^+ \mu^-$ branching fractions.

5.4.3 Hadronisation factors

The normalisation factors depend on the hadronisation factors, f_u, f_s, f_d , that give the probability of a b or \bar{b} quark to form a B^+ , B_s^0 or B^0 , respectively. The hadronisation factors f_d and f_u are equal therefore the $B^0 \rightarrow \mu^+\mu^-$ branching fraction does not depend on hadronisation factors. For the $B_s^0 \rightarrow \mu^+\mu^-$ the ratio f_s/f_d is used in the normalisation, since $f_d = f_u$. This ratio was measured at LHCb for pp collisions at $\sqrt{s} = 7$ TeV, and it is used for the different LHC \sqrt{s} energies. However for Run 2 the f_s/f_d ratio must be modified for a small observed relative production difference. The uncertainty on the hadronisation factor ratio contributes the largest uncertainty to the $B_s^0 \rightarrow \mu^+\mu^-$ branching fraction. Alternatively the $B_s^0 \rightarrow \mu^+\mu^-$ decay could be normalised using a different B_s^0 decay however the precision of the measured branching fractions and abundance of B_s^0 decays, such as $B_s^0 \rightarrow J/\psi\phi$, are not high enough at present to provide a lower overall uncertainty on the measured branching fraction.

5.4.4 Normalisation parameters

The yields, efficiencies and hadronisation factors are combined to produce separate normalisation factors for each year of data taking and each normalisation channel. The consistency of the efficiencies and yields for each normalisation channel are checked for each year by comparing the branching fraction ratios $\mathcal{B}(B^0 \rightarrow K^+\pi^-)/\mathcal{B}(B^+ \rightarrow J/\psi K^+)$ and $\mathcal{B}(B^+ \rightarrow J/\psi K^+)/\mathcal{B}(B_s^0 \rightarrow J/\psi\phi)$ with the PDG values. The yearly normalisation factors are combined for each channel using to produce the normalisation factors for Run 1 and for Run 2 taking into account correlations between the parameters. A weighted average of the normalisation factors for $B^0 \rightarrow K^+\pi^-$ and is used to produce the overall normalisation factors for Run 1 and Run 2 as shown in Table 5.3.

Normalisation Paramters	Run 1	Run 2
$\alpha_d \times 10^{11}$	2.877 ± 0.101	3.521 ± 0.155
$\alpha_s \times 10^{10}$	1.071 ± 0.072	1.306 ± 0.095

Table 5.3 Normalisation parameters for $B_s^0 \rightarrow \mu^+\mu^-$ and $B^0 \rightarrow \mu^+\mu^-$ for Run 1 and Run 2.

5.5 Results

As described earlier in Section 5.1 the $B_s^0 \rightarrow \mu^+\mu^-$ and $B_{(s)}^0 \rightarrow \mu^+\mu^-$ branching fractions are measured by a simultaneous maximum likelihood fit to the dimuon invariant mass of the Run 1 and Run 2 data sets, each divided into four BDT bins.

In the fit the mass *pdfs* and fraction of $B_{(s)}^0 \rightarrow \mu^+\mu^-$ decays in each BDT bin are constrained within Gaussian limits using the expected values and uncertainties. The yield of the combinatorial background is left free in the fit in each BDT bin and the slope of the mass distribution is constrained to have the same value across all bins for each data set. The yields of the backgrounds from $B \rightarrow h^+h^-$, $B^0 \rightarrow \pi^-\mu+\nu_\mu$, $B_s^0 \rightarrow K^-\mu+\nu_\mu$, $B^{0(+)} \rightarrow \pi^{0(+)}\mu^+\mu^-$, $B^0 \rightarrow \pi^0\mu^+\mu^-$ and $B_c^+ \rightarrow J/\psi\mu^+\nu_\mu$ decays in each BDT bin are constrained around the expected values, similarly to the signal fractions but the mass shapes are fixed in the fit.

The branching fraction results from the fit are;

$$\begin{aligned}\mathcal{B}(B_s^0 \rightarrow \mu^+\mu^-) &= (2.8 \pm 0.6) \times 10^{-9} \\ \mathcal{B}(B^0 \rightarrow \mu^+\mu^-) &= (1.6_{-0.9}^{+1.1}) \times 10^{-10}\end{aligned}\tag{5.9}$$

Figure 5.4 shows the fit results for $B_{(s)}^0 \rightarrow \mu^+\mu^-$ candidates in the 4 BDT bins for both Run 1 and Run 2 data and Figure ?? the 2-dimensional likelihood profile for the $B^0 \rightarrow \mu^+\mu^-$ and $B_s^0 \rightarrow \mu^+\mu^-$ branching fraction measurements. The statistical significance of the $B_s^0 \rightarrow \mu^+\mu^-$ signal is 7.9σ making this measurement the first single experiment observation of the $B_s^0 \rightarrow \mu^+\mu^-$ decay. While the significance of the $B^0 \rightarrow \mu^+\mu^-$ signal is less at 1.9σ , therefore the CLs method [] is used to place an upper limit on the branching fraction of $\mathcal{B}(B^0 \rightarrow \mu^+\mu^-) < 3.4 \times 10^{-10}$ at the 95 % confidence level.

The quoted $B_s^0 \rightarrow \mu^+\mu^-$ branching fraction assumes the Standard Model value for $A_{\Delta\Gamma}$, applying the corrections detailed in Section 5.2.3 for $A_{\Delta\Gamma}$ values of 0 and -1 shift the central value of $\mathcal{B}(B_s^0 \rightarrow \mu^+\mu^-)$ by 4.6 % and 10.9 %, respectively. All results are consistent with the predictions of the Standard Model.

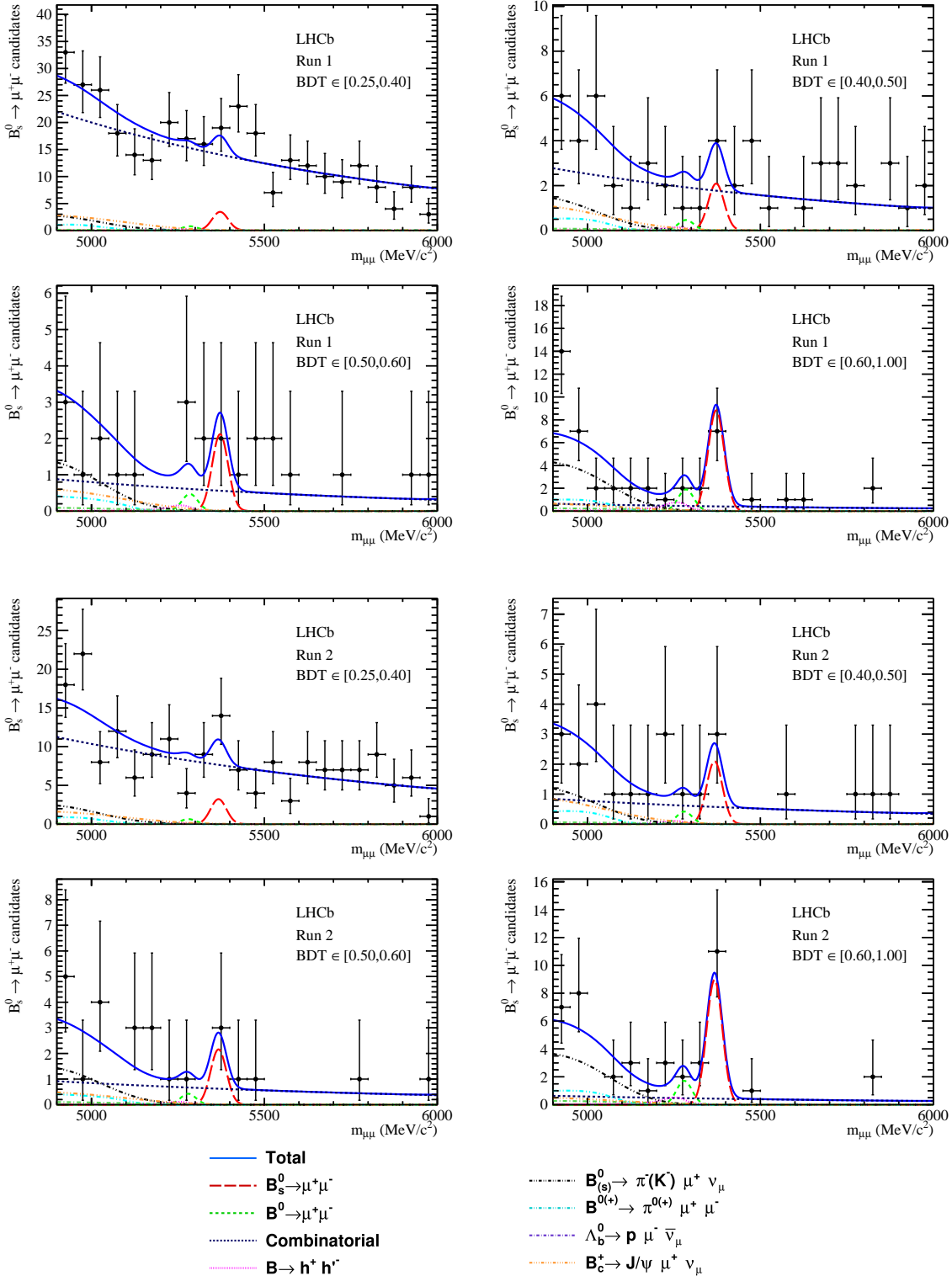


Fig. 5.4 Mass distribution in BDT bins for selected $B_s^0 \rightarrow \mu^+ \mu^-$ and $B^0 \rightarrow \mu^+ \mu^-$ candidates with the fit overlaid for Run 1 and Run 2 data. The fit includes components for $B^0 \rightarrow \mu^+ \mu^-$, $B_s^0 \rightarrow \mu^+ \mu^-$, combinatorial backgrounds, mis-identified $B \rightarrow h^+ h^-$ decays and backgrounds from semi-leptonic decays. *Needs to be updated for new tail parameters.*

Chapter 6

Measurement of the $B_s^0 \rightarrow \mu^+\mu^-$ effective lifetime

This chapter describes the measurement of the $B_s^0 \rightarrow \mu^+\mu^-$ effective lifetime. Section 6.1 presents an overview of the analysis strategy used to measure the $B_s^0 \rightarrow \mu^+\mu^-$ effective lifetime from data, the mass and decay time distributions of $B_s^0 \rightarrow \mu^+\mu^-$ decays and backgrounds passing the selection must be known for the optimisation of the analysis strategy and the measurement of the effective lifetime. The *pdfs* of the mass and decay time distributions are described in Sections 6.2 and 6.3 for signal and background decays. Due to the very rare nature of $B_s^0 \rightarrow \mu^+\mu^-$ decays, the measurement strategy has been optimised to produce the lowest expected uncertainty on the measured $B_s^0 \rightarrow \mu^+\mu^-$ effective lifetime, the optimisation studies are detailed in Section 6.4. Finally the measurement of the $B_s^0 \rightarrow \mu^+\mu^-$ effective lifetime is presented in Section 6.5.

The work presented in this chapter was completed for this thesis except the areas where the same method as the branching fraction analysis is used. This includes the background mass *pdf* evaluation and the expected signal and background yields for the data set, as well as the yields from data.

6.1 Analysis Strategy

The $B_s^0 \rightarrow \mu^+\mu^-$ effective lifetime is measured from the decay time distribution of $B_s^0 \rightarrow \mu^+\mu^-$ candidates passing the selection criteria described in Section ???. However the selection requirements do not completely separate real $B_s^0 \rightarrow \mu^+\mu^-$ decays from the backgrounds, therefore to measure the $B_s^0 \rightarrow \mu^+\mu^-$ effective lifetime either the *pdfs* describing the decay time distributions of signal and backgrounds must be known or the background candidates must be removed from the data set leaving only the

signal distribution. Several approaches were investigated to determine which would produce stable results for the measured $B_s^0 \rightarrow \mu^+\mu^-$ effective lifetime on 4.4 fb^{-1} and yield the smallest expected statistical uncertainty on the result. The most successful approach uses the sPlot statistical method as described in [29] that provides a way to statistically untangle the signal and background distributions in a data set.

This method produces a two step strategy to measure the effective lifetime. This first step is an unbinned maximum likelihood fit to the dimuon invariant mass spectrum, where components are included in the *pdf* for $B_s^0 \rightarrow \mu^+\mu^-$ decays and each background decay. The mass fit measures the yields of the signal and background decays and from the fit sWeights are calculated for each component in the mass fit. The second step is to apply the sWeights of $B_s^0 \rightarrow \mu^+\mu^-$ decays to the data set, effectively removing all background decays, and perform an unbinned maximum likelihood fit to the signal weighted decay time distribution to measure the $B_s^0 \rightarrow \mu^+\mu^-$ effective lifetime. In the final fit only the $B_s^0 \rightarrow \mu^+\mu^-$ decay time *pdf* is needed to measure the effective lifetime. Due to the low statistics expected for the data set, Run 1 and Run 2 data are combined and the maximum likelihood fit to the mass and weighted decay time distributions are performed to the combined data.

A requirement of the sPlot procedure is that the variable used to calculate the sWeights and the variable from which the observable is measured must be independent. The correlation of the mass and decay time for $B_s^0 \rightarrow \mu^+\mu^-$ decays and combinatorial background decays has been evaluated using simulated decays and data. The correlation is of the order of a few percent, as shown in Table 6.1, therefore mass can be used to accurately determine sWeighted to measure the $B_s^0 \rightarrow \mu^+\mu^-$ effective lifetime.

Year	$B_s^0 \rightarrow \mu^+\mu^-$ correlation	$b\bar{b} \rightarrow \mu^+\mu^- X$ correlation
2011	-0.008	0.003
2012	-0.006	0.008
2015	-0.006	0.010
2016	0.008	0.002

Table 6.1 Correlation between mass and decay time for candidate from $B_s^0 \rightarrow \mu^+\mu^-$ simulated decays and combinatorial background decays from data for 2011, 2012, 2015 and 2016 data taking conditions. The full effective lifetime selection is applied to simulated $B_s^0 \rightarrow \mu^+\mu^-$ decays and decays in data must pass the effective lifetime selection requirements apart from the global BDT cut and have a dimuon invariant mass of $5447 \text{ MeV}/c^2$.

The sWeights are calculated using the RooFit package [30], however the raw sWeights from the mass fit cannot be used directly in the maximum likelihood fit to

measure the effective lifetime. The normalisation of the sWeights will not produce the correct statistical uncertainty on the effective lifetime measurement. Therefore the sWeights are re-normalised via

$$\omega'_i = \omega_i \cdot \frac{\sum_j \omega_j}{\sum_j \omega_j^2} \quad (6.1)$$

where ω_i are the sWeights values for each decay. The re-normalised sWeights will produce the correct statistical uncertainty in a maximum likelihood fit to measure the $B_s^0 \rightarrow \mu^+ \mu^-$ effective lifetime.

The approach outlined here is suited to the measurement of the $B_s^0 \rightarrow \mu^+ \mu^-$ effective lifetime because the mass *pdfs* are accurately known for the signal and background decays in the data set from the branching fraction analysis. Furthermore no knowledge is needed to the decay time *pdfs* in the final fit, this is advantageous because decay time distribution of combinatorial background decays is challenging to accurately model. However the overall performance of this strategy depends on the maximum likelihood fit to the invariant mass distribution; how many background components are included in the fit and the mass range the fit covers. The determination of the final fit configuration was done using toy studies, described in Section 6.4, that study a range of different mass ranges largest being 4900 - 6000 MeV/ c^2 . Therefore the development of the fit configuration requires the mass and decay time *pdfs* of all background within the largest mass range need to be known as well as the signal *pdfs*.

6.2 Mass *pdfs*

The selection criteria used to identify $B_s^0 \rightarrow \mu^+ \mu^-$ candidates for the $B_{(s)}^0 \rightarrow \mu^+ \mu^-$ branching fraction and $B_s^0 \rightarrow \mu^+ \mu^-$ effective lifetime measurements are very similar. Therefore the background decays passing the $B_s^0 \rightarrow \mu^+ \mu^-$ effective lifetime selection and in the mass range 4900 - 6000 MeV/ c^2 are the same as those passing the branching fraction selection, although the yields will be different. Therefore the maximum likelihood fit to extract the sWeights is very similar to the fit to the mass distribution used to measure the $B_{(s)}^0 \rightarrow \mu^+ \mu^-$ yields for the measurement of the $B_{(s)}^0 \rightarrow \mu^+ \mu^-$ branching fractions. The *pdf* used in the mass fit has the form

$$\mathcal{P}_{tot}(m) = N_{sig} \mathcal{P}_{sig}(m) + \sum_i N_{bkg}^i \mathcal{P}_{bkg}^i(m) \quad (6.2)$$

where i represents a particular background, $N_{sig(bkg)}$ are the signal (background) yields and $P_{sig(bkg)}$ are the signal (background) *pdfs*. The background decays include; $B^0 \rightarrow \mu^+\mu^-$, $B \rightarrow h^+h^-$, $\Lambda_b^0 \rightarrow p\mu^-\nu_\mu$, $B^0 \rightarrow \pi^-\mu+\nu_\mu$, $B_s^0 \rightarrow K^-\mu+\nu_\mu$, $B^+ \rightarrow \pi^+\mu^+\mu^-$, $B^0 \rightarrow \pi^0\mu^+\mu^-$, $B_c^+ \rightarrow J/\psi\mu^+\nu_\mu$ and combinatorial background decays. For the effective lifetime measurement the $B^0 \rightarrow \mu^+\mu^-$ decay is included as a background.

The $B_s^0 \rightarrow \mu^+\mu^-$ and $B^0 \rightarrow \mu^+\mu^-$ mass *pdfs* are described by the same a Crystal ball functions used in the branching fraction measurements, with the Run 1 parameters given in Table 5.1. The Run 1 and Run 2 data sets are combined for the measurement of the $B_s^0 \rightarrow \mu^+\mu^-$ effective lifetime therefore only one mass *pdf* is needed to describe $B_{(s)}^0 \rightarrow \mu^+\mu^-$ decays in data. The choice of Run 1 or Run 2 parameters in the *pdf* has a negligible affect on the measurement of the $B_s^0 \rightarrow \mu^+\mu^-$ effective lifetime as shown in Section ??.

Mis-identified semi-leptonic decays, $\Lambda_b^0 \rightarrow p\mu^-\nu_\mu$, $B^0 \rightarrow \pi^-\mu+\nu_\mu$, $B_s^0 \rightarrow K^-\mu+\nu_\mu$, $B^+ \rightarrow \pi^+\mu^+\mu^-$, $B^0 \rightarrow \pi^0\mu^+\mu^-$ and $B_c^+ \rightarrow J/\psi\mu^+\nu_\mu$ are each described by an Argus function convoluted with a Gaussian function evaluated from simulated decays using the same method as described in Section 5.3. The particle identification requirements and the cut on the global BDT use in the selection of candidates for the effective lifetime measurement are taken into account in the evaluation of the *pdf* shapes. However unlike the *pdfs* used in the branching fraction analysis a separate *pdf* is used for each background decay.

Backgrounds from mis-identified $B \rightarrow h^+h^-$ decays are described by the double Crystal Ball function evaluated using the method described in Section 5.3 with the effective lifetime particle identification requirements applied. Finally the combinatorial background is modelled with a decaying exponential where the slope is not constrained in the final fit.

The mass *pdfs* for the signal and backgrounds are evaluated for the mass range 4900 to 6000 MeV/ c^2 to be used in the toy studies described in Section 6.4. The parameters used describing the background shapes are given in Appendix ??.

6.3 Decay time *pdfs*

The efficiency of the selection criteria to identity candidates for the measurement of the $B_s^0 \rightarrow \mu^+\mu^-$ effective lifetime varies as a function of decay time for both signal and background decays, biasing the decay time distribution. The bias arises because variables used in the selection and the global BDT, such as the isolations and the B meson impact parameter and flight distance significance, are correlated with the decay

time. Consequently cuts placed on these variables have a non-uniform efficiency across the decay time range. Therefore the *pdf* describing the decay time changes from a decaying exponential to

$$\mathcal{P}(t) = \epsilon(t) \times e^{-t/\tau} \quad (6.3)$$

where $\epsilon(t)$ is the selection efficiency as a function of decay time. The decay time distribution and selection efficiency as a function of decay time are shown in Figure 6.1 for simulated $B_s^0 \rightarrow \mu^+ \mu^-$ decays at different stages through the selection. The cut on the global BDT causes the biggest decay time bias as expected since it is the hardest selection cut applied.

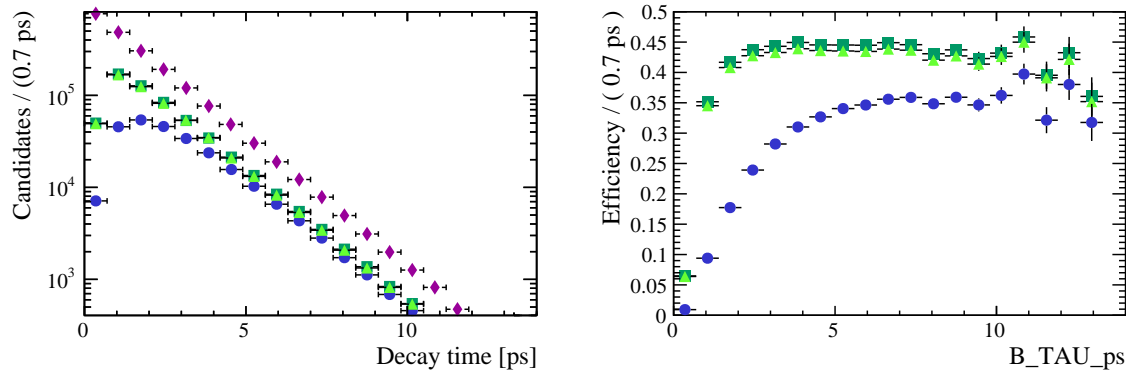


Fig. 6.1 Decay time distribution (left) and selection efficiency as a function of decay time (right) for 2012 $B_s^0 \rightarrow \mu^+ \mu^-$ simulated decays at different stages of the selection process. The decay time distributions and efficiencies are shown for reconstructed decays that pass the trigger, stripping and pre-selection cuts (turquoise), the decays that go on to pass PID requirements (green) and decays that pass all selection requirement including the global BDT cut (blue). Also the decay time distribution is shown for all generated simulated decays (purple).

To measure the $B_s^0 \rightarrow \mu^+ \mu^-$ effective lifetime the efficiency of the selection on $B_s^0 \rightarrow \mu^+ \mu^-$ decay as a function of decay time must be accurately modelled. The determination of $\epsilon(t)$ for $B_s^0 \rightarrow \mu^+ \mu^-$ decays is described in Section 6.3.1. Although the sPlot method used to measure the $B_s^0 \rightarrow \mu^+ \mu^-$ effective lifetime means that the decay time *pdfs* of the backgrounds present in the data set are not needed, realistic descriptions of the background decay time *pdfs* are necessary for optimising the mass fit configuration. The background *pdfs* are used described in Section 6.3.2.

6.3.1 $B_s^0 \rightarrow \mu^+ \mu^-$ decay time *pdf*

The selection efficiency of $B_s^0 \rightarrow \mu^+ \mu^-$ decays as a function of decay time is modelled by an ‘acceptance’ function. A range of different models were investigated for the

acceptance function, the parameterised acceptance

$$\epsilon(t) = \frac{[a(t - t_0)]^n}{1 + a(t - t_0)^n} \quad (6.4)$$

used in [31] was found to best describe the $B_s^0 \rightarrow \mu^+ \mu^-$ decay time efficiency. The acceptance function parameters are taken from a fit to simulated $B_s^0 \rightarrow \mu^+ \mu^-$ decays and are fixed in the fit to data. The parameters could not be determined from data because there are too few $B_s^0 \rightarrow \mu^+ \mu^-$ decays in data and the efficiency distribution of the more abundant $B \rightarrow h^+ h^-$ decays after the selection is quite different to that of $B_s^0 \rightarrow \mu^+ \mu^-$. The decay time efficiency for each year of data taking is slightly different therefore simulated decays from each year of data taking must be used to determine the acceptance parameters.

In general simulated decays model distributions in data reasonably well, however the number of tracks present in an event are not well modelled in the simulation. Although the $B_s^0 \rightarrow \mu^+ \mu^-$ decay time distribution does not depend on the number of tracks present in the event, the isolations used in the global BDT do. Therefore the selection efficiency as a function of decay time depends on the number of tracks in the event and cannot be accurately described by simulated decays alone. To overcome this the number of tracks in an event for simulated $B_s^0 \rightarrow \mu^+ \mu^-$ decays are weighted using information from the number of tracks per event for $B^0 \rightarrow K^+ \pi^-$ decays in both data and simulation.

The selection requirements listed in Table ?? are used to identify $B^0 \rightarrow K^+ \pi^-$ decays in data and simulated decays but importantly the global BDT cut is not applied. The $DLL_{K\pi}$ variable is used to separate $B^0 \rightarrow K^+ \pi^-$ decays from other $B \rightarrow h^+ h^-$ decays in data and the loose trigger requirements used for the branching fraction analysis are applied to data and simulated decays to keep a high trigger efficiency¹. The same requirements are applied to simulated decays. The distribution of the number of tracks present in events containing $B^0 \rightarrow K^+ \pi^-$ decays is obtained from data by performing a maximum likelihood fit to the B^0 mass distribution and extracting sWeights. The distribution of the weighted number of tracks per event in data is compared with the distribution in simulated $B^0 \rightarrow K^+ \pi^-$ decays. The mass fits to $B^0 \rightarrow K^+ \pi^-$ decays in data are shown in Figure 6.2 and the normalised distributions

¹The Hlt2Phys Dec trigger decision was not correctly implemented in 2016 simulated decays, therefore the DEC decisions of a combination of trigger lines designed to select $B \rightarrow h^+ h^-$ are used to emulate the Hlt2Phys DEC trigger decision. The trigger lines are Hlt2Topo2BodyDecision, Hlt2B2HH_Lb2PPiDecision, Hlt2B2HH_Lb2PKDecision Dec, Hlt2B2HH_B2PiPiDecision, Hlt2B2HH_B2PiKDecision, Hlt2B2HH_B2KKDecision and Hlt2B2HH_B2HHDecision. These trigger lines are applied to both data and simulated decays.

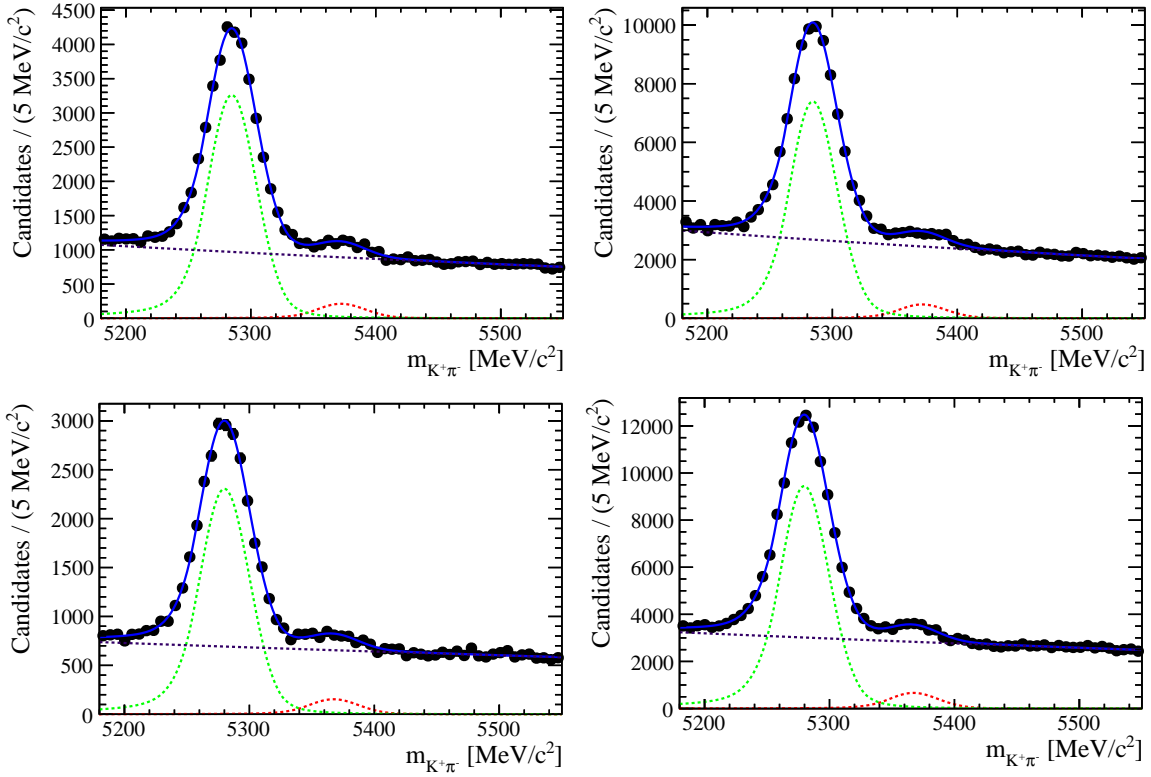


Fig. 6.2 Maximum likelihood fits to the mass distribution of $B^0 \rightarrow K^+\pi^-$ candidates in 2011 (top left), 2012 (top right), 2015 (bottom left) and 2016 (bottom right) data. The mass *pdf* includes components for $B^0 \rightarrow K^+\pi^-$ (green), $B_s^0 \rightarrow K^+\pi^-$ (red) and combinatorial background (purple).

of the number of tracks per event in weighted data and simulated decays are shown in Figure 6.3. Each year of data taking is kept separate and the same simulation version is used for $B^0 \rightarrow K^+\pi^-$ simulated decays as available for $B_s^0 \rightarrow \mu^+\mu^-$ decays.

The distributions of the number of tracks per event for $B^0 \rightarrow K^+\pi^-$ decays in data and simulated decays are used to weight $B^0 \rightarrow K^+\pi^-$ decays so that the distribution in simulation matches that in data. The weights are evaluated by taking the ratio of the normalised histograms in Figure 6.3 for the number of tracks per event in data and simulation for each year. The affect on the decay time distribution of using these weights and then applying the global BDT cut is shown in Figure 6.4 for the simulated $B^0 \rightarrow K^+\pi^-$ decays. The difference between the decay time distributions with and without the weights is not large but clearly noticeable at low decay times where the change in selection efficiency is greatest.

The same weights are applied to simulated $B_s^0 \rightarrow \mu^+\mu^-$ decays by binning the number of tracks per event for $B_s^0 \rightarrow \mu^+\mu^-$ decays in the same way to used for

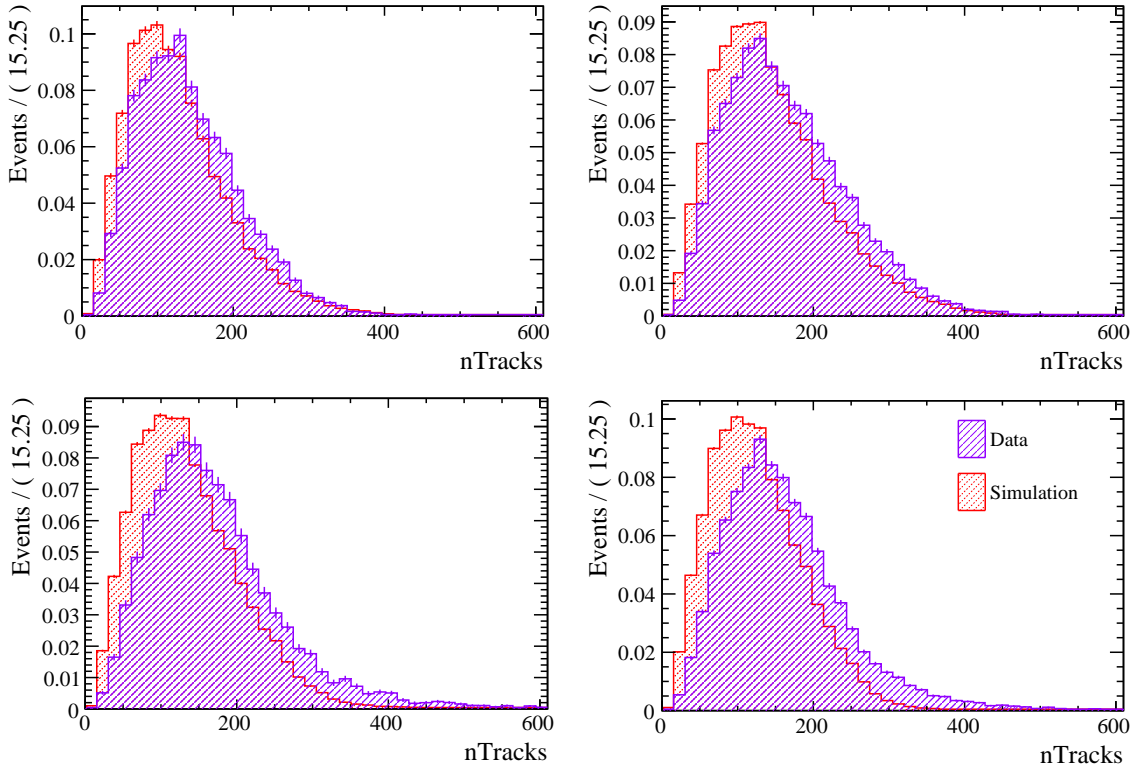


Fig. 6.3 Normalised histograms of the number of tracks per event in simulated $B^0 \rightarrow K^+ \pi^-$ decays and weighted $B^0 \rightarrow K^+ \pi^-$ decays in data for 2011 (top left), 2012 (top right), 2015 (bottom left) and 2016 (bottom right) data.

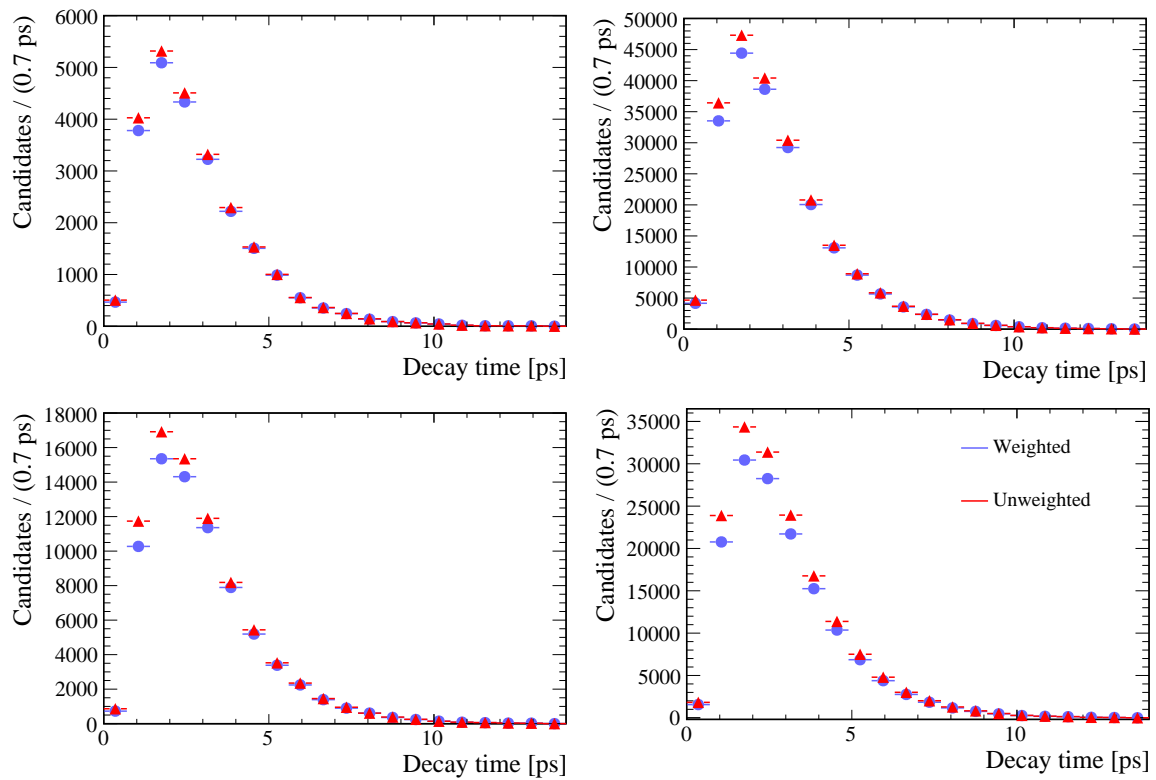


Fig. 6.4 Decay time distributions for weighted and un-weighted $B^0 \rightarrow K^+\pi^-$ simulated decays for for 2011 (top left), 2012 (top right), 2015 (bottom left) and 2016 (bottom right) data taking conditions.

$B^0 \rightarrow K^+\pi^-$ decays. The weights are applied to decays that pass selection but before the global BDT cut is applied. The change in the decay time distribution for simulated decays after the global BDT cut is shown in Figure 6.6 in the comparison of weighted and un-weighted $B_s^0 \rightarrow \mu^+\mu^-$ decay time distributions. Similarly to $B^0 \rightarrow K^+\pi^-$ decays the biggest effect is at low decay times where the change in selection efficiency is greatest as seen in Figure 6.1.

The reweighting relies on the number of tracks per event being very similar for $B^0 \rightarrow K^+\pi^-$ and $B_s^0 \rightarrow \mu^+\mu^-$ decays, this cannot be evaluated in data due to the small number of $B_s^0 \rightarrow \mu^+\mu^-$ decays in data. However Figure 6.6 shows a comparison of the number of tracks per event for simulated $B_s^0 \rightarrow \mu^+\mu^-$ and $B^0 \rightarrow K^+\pi^-$ decays for each year and resulting distributions are rather similar.

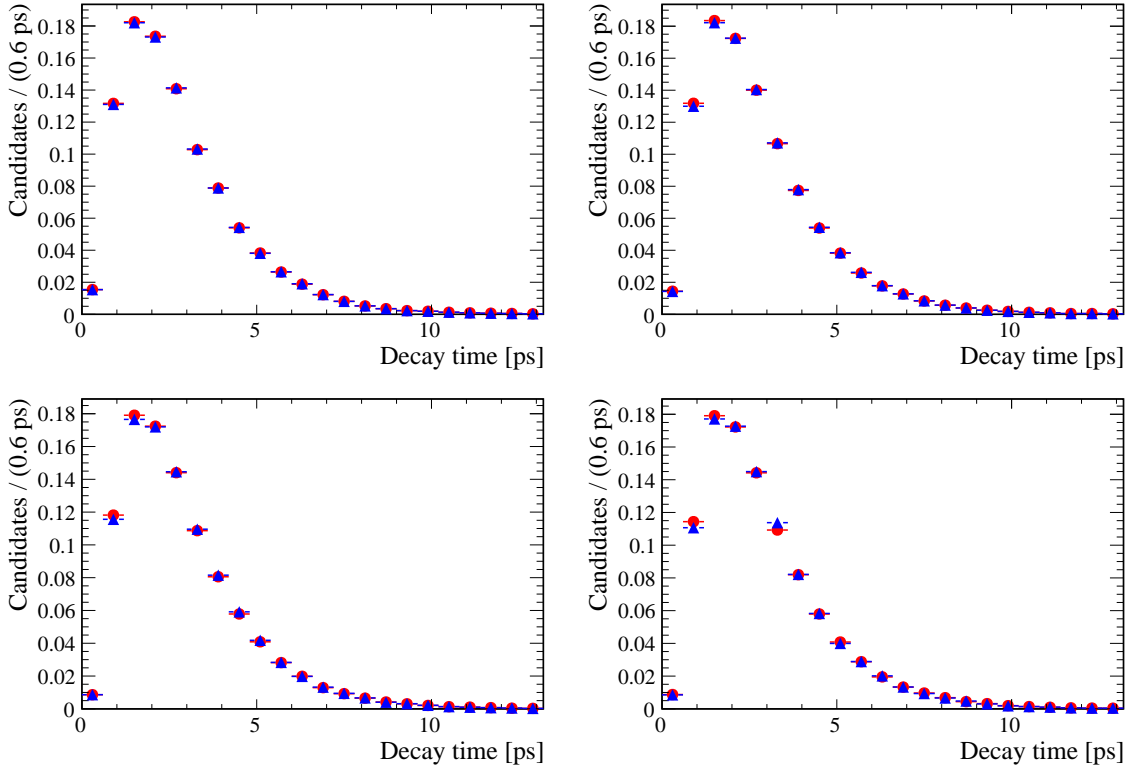


Fig. 6.5 Decay time distributions for weighted and un-weighted $B_s^0 \rightarrow \mu^+\mu^-$ simulated decays for for 2011 (top left), 2012 (top right), 2015 (bottom left) and 2016 (bottom right) data taking conditions. Distributions have been normalised to have unit area.

The decay time efficiency will now be accurately modelled in the weighted simulated $B_s^0 \rightarrow \mu^+\mu^-$ decays and the parameters in the acceptance function can be evaluated. The number of simulated decays available for each year does not correspond to the proportions of decays present in each year of the data. Therefore weights are used

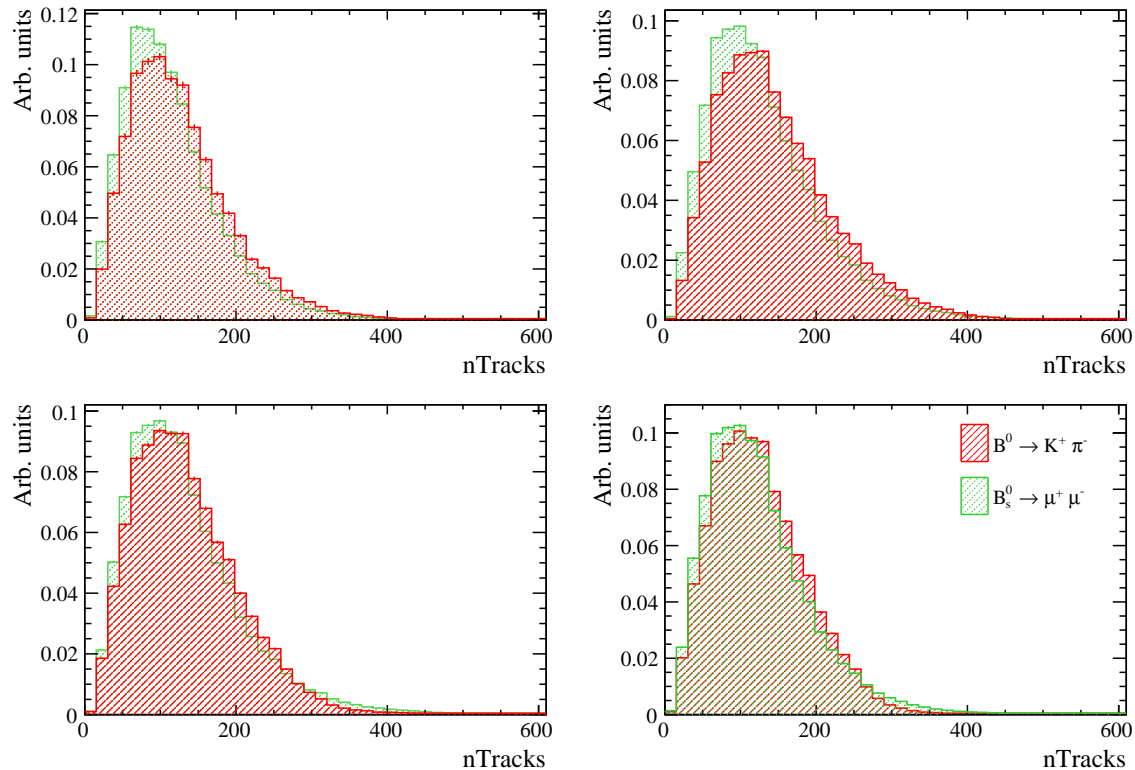


Fig. 6.6 Normalised histograms of the number of tracks per event in simulated $B^0 \rightarrow K^+ \pi^-$ and $B_s^0 \rightarrow \mu^+ \mu^-$ decays in data for 2011 (top left), 2012 (top right), 2015 (bottom left) and 2016 (bottom right) data.

to combine the simulated decays so that the combined set of decays has the same proportions of decays for each year as the complete data set. The proportion of events of each year is taken from the number of $B_s^0 \rightarrow J/\psi\phi$ decays in data for each year corrected for the selection differences for $B_s^0 \rightarrow \mu^+ \mu^-$ and $B_s^0 \rightarrow J/\psi\phi$ decays. The $B_s^0 \rightarrow J/\psi\phi$ yields, $Y^{J/\psi\phi}$, are extracting from maximum likelihood fits to the mass spectrum of candidates in each year of data. The selection applied to identify candidates is the very similar to that applied to $B_s^0 \rightarrow \mu^+ \mu^-$ decays apart from the particle identification and global BDT requirements. This decay is chosen because the ratio of the efficiencies for the stripping, trigger and pre-selection requirements of $B_s^0 \rightarrow \mu^+ \mu^-$ and $B_s^0 \rightarrow J/\psi\phi$ decays is uniform across the different years making $B_s^0 \rightarrow J/\psi\phi$ decays a good proxy for $B_s^0 \rightarrow \mu^+ \mu^-$. The weights applied to simulated $B_s^0 \rightarrow \mu^+ \mu^-$ decays are

$$\omega_i = \frac{Y_i^{J/\psi\phi} \epsilon_i}{\sum_j Y_j^{J/\psi\phi} \epsilon_j} \cdot \frac{\sum_k N_k^{\mu^+ \mu^-}}{N_i^{\mu^+ \mu^-}} \quad (6.5)$$

where i represents the year and $N^{\mu^+ \mu^-}$ the number of simulated $B_s^0 \rightarrow \mu^+ \mu^-$ decays available for the year passing the full $B_s^0 \rightarrow \mu^+ \mu^-$ selection and ϵ_i the efficiency of the particle identification and global BDT requirements for $B_s^0 \rightarrow \mu^+ \mu^-$ decays that have passed all other selection requirement evaluated from simulated decays. The weights applied to simulated $B_s^0 \rightarrow \mu^+ \mu^-$ decays and values of the different components of the weights are given in Table 6.2.

Year (i)	Y_i	ϵ_i	N_i	ω_i	$\mathcal{N}_i \equiv N_i \omega_i$
2011	19190	0.412	70448	1.72	131364
2012	42103	0.406	254822	1.03	262461
2015	8571	0.410	222820	0.24	53917
2016	37765	0.406	124870	1.88	235218

Table 6.2 Weights used to combine simulated $B_s^0 \rightarrow \mu^+ \mu^-$ decays for each year to determine the acceptance function. Weights ensure the proportion of simulated events for each year matches what is expected in data.

An unbinned maximum likelihood fit is performed to the combined simulated $B_s^0 \rightarrow \mu^+ \mu^-$ decays to determine the acceptance parameters in equation 6.4. In the fit the acceptance parameters are free and the $B_s^0 \rightarrow \mu^+ \mu^-$ lifetime is constrained to the weighted average of lifetimes used to generate each year of simulated decays. The fit results are shown in Figure 6.7 and the acceptance parameters are given in Table ??.

Figure 6.8 shows the selection efficiency histogram as a function of decay time with the acceptance function overlaid.

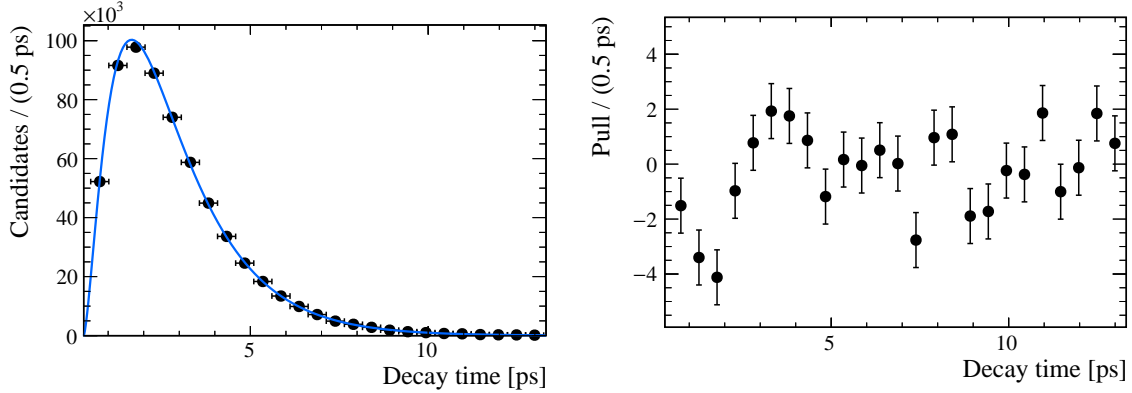


Fig. 6.7 The maximum likelihood fit to the combined decay time distribution (left) of 2011, 2012, 2015 and 2016 simulated $B_s^0 \rightarrow \mu^+ \mu^-$ decays and the pull distribution of the fit.

6.3.2 Background decay time pdf

The final fit to measure the $B_s^0 \rightarrow \mu^+ \mu^-$ effective lifetime does not require knowledge of the decay time *pdfs* of the backgrounds. However the fit configuration is developed using toy studies that use the mass and decay time distributions of both signal and background decays. Therefore realistic models of the decay time *pdfs* are needed to determine the optimal fit configuration.

The selection biases the decay time distributions of the backgrounds in the same way as the $B_s^0 \rightarrow \mu^+ \mu^-$ decay time. Therefore they are described by the same *pdfs* as in equation 6.3.

The backgrounds from semi-leptonic, $B \rightarrow h^+ h^-$ and $B^0 \rightarrow \mu^+ \mu^-$ decays are assigned the same acceptance function as $B_s^0 \rightarrow \mu^+ \mu^-$ decays because the decay time efficiency of these backgrounds roughly the same as $B_s^0 \rightarrow \mu^+ \mu^-$ decays. The acceptances of these backgrounds does not need to be as accurately known as the acceptance function of the signal because very few background decays from these sources will be present in the data set after the selection and the final results does not depend on the acceptance function of the backgrounds. The lifetimes of these background decays are taken from a fit to simulated decays for, for $B \rightarrow h^+ h^-$ the fit is performed to a combined set of $B \rightarrow h^+ h^-$ decays representing what is expected in data.

The decay time *pdf* of the combinatorial background is more challenging to determine. This background arises from random combinations of muons in the event and not

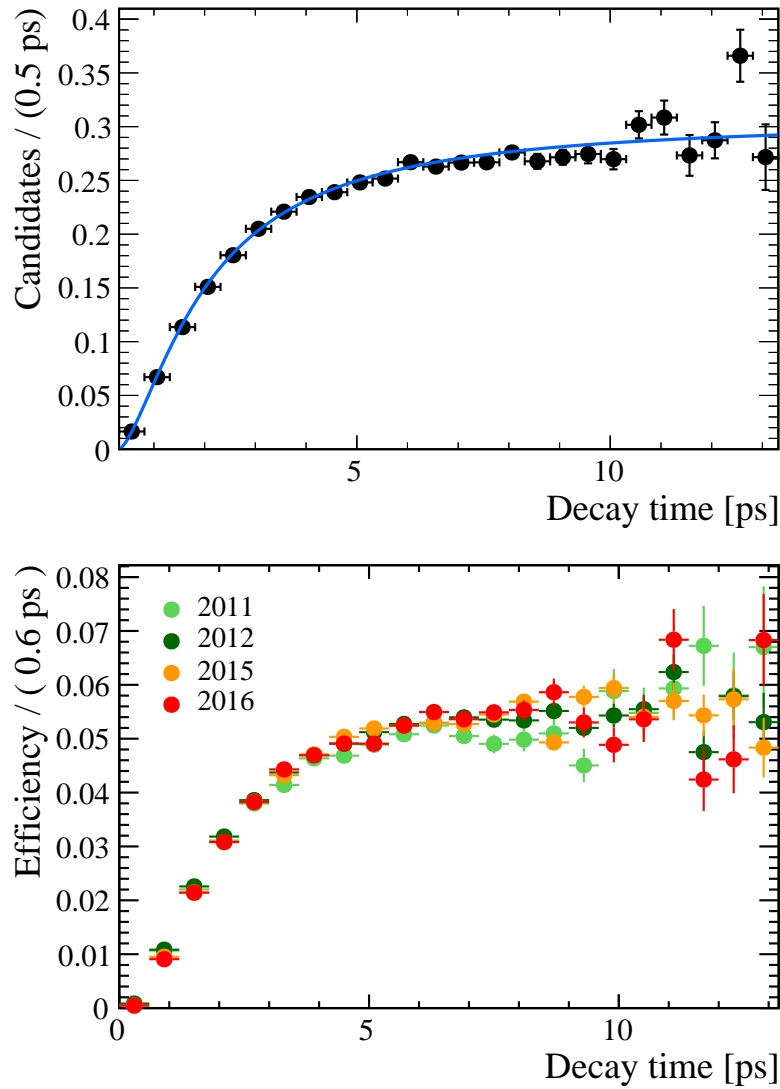


Fig. 6.8 The selection efficiency histogram as a function of decay time with the acceptance *pdf* overlaid for weighted 2011, 2012, 2015 and 2016 simulated $B_s^0 \rightarrow \mu^+ \mu^-$ decays (left) and the efficiency histograms for each year separately for weighted simulated $B_s^0 \rightarrow \mu^+ \mu^-$ decays.

from one source, therefore there is no single lifetime that describes the background. Furthermore the global BDT which is designed to separate $B_s^0 \rightarrow \mu^+ \mu^-$ decays from combinatorial background decays will have a different efficiency as a function of decay time for the combinatorial background compared to the signal. The decay time *pdf* of the combinatorial background cannot be evaluated from simulated decays or decays in data that pass the $B_s^0 \rightarrow \mu^+ \mu^-$ selection because there are too few candidates left. Therefore the decay time *pdf* of the combinatorial background for $B_s^0 \rightarrow \mu^+ \mu^-$ decays is evaluated from combinational background of $B \rightarrow h^+ h^-$ decays using candidates in data that pass the $B \rightarrow h^+ h^-$ selection and have a reconstructed mass greater than 5447 MeV/ c^2 , above the B_s^0 signal region. The decay time *pdf* for combinatorial background decays is modelled by

$$P_{cbg}(t) = \epsilon(t) \times \left(f \cdot e^{-\Gamma_1 t} + (1 - f) \cdot e^{-\Gamma_2 t} \right) \quad (6.6)$$

where Γ_1 and Γ_2 are two independent lifetimes used to describe the background, f describes the fraction of candidates with each lifetime and the same acceptance shape as in equation 6.4 is used for describe the decay time efficiency. The lifetimes are different, one describes a long lived component and the other a short lived component that are evident in the data. The decay time acceptance is flat at large decay times, therefore the lifetimes of the combinatorial background decays are determined from a maximum likelihood fit of equation 6.6, setting $\epsilon(t) = 1$, to candidates with a decay time above 2.5 ps. The acceptance function parameters are then determined from a maximum likelihood fit to the full decay time range using equation 6.6 where the lifetimes and the fraction of candidates with each lifetime are fixed. The results are shown in Figure 6.9 and the *pdf* parameters in Table 6.3, the t_0 parameter is fixed in the fit to improve fit stability.

Parameter	Value
a	$1.45 \pm 0.12 \text{ ps}^{-1}$
n	1.92 ± 0.17
t_0	0.290 ps
Γ_1	$0.06 \pm 0.05 \text{ ps}^{-1}$
Γ_2	$0.77 \pm 0.17 \text{ ps}^{-1}$
f	0.032 ± 0.027

Table 6.3 Parameters to described the background decay time distribution from combinatorial background decays in data passing the $B \rightarrow h^+ h^-$ selection.

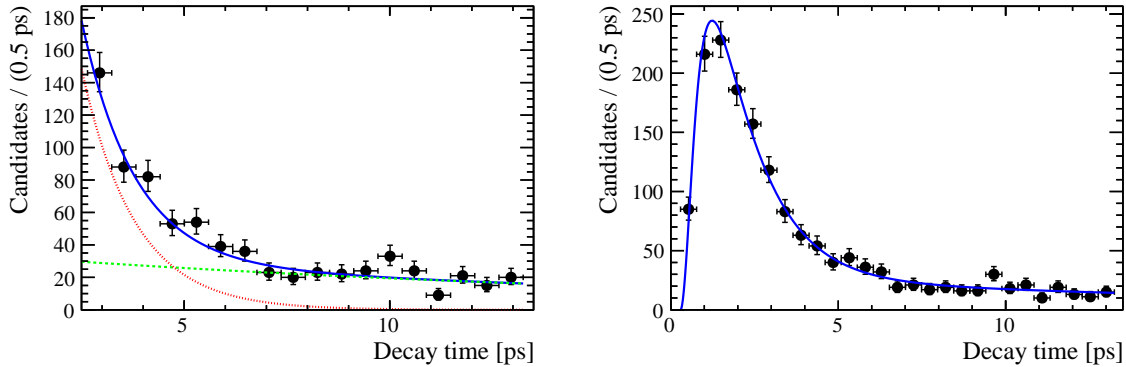


Fig. 6.9 The maximum likelihood to determine the lifetimes of the background (left), with the long live component (green) and the short lived component (red) shown and the acceptance parameters (right) of combinatorial background decays in data passing the $B \rightarrow h^+h^-$ selection requirements.

This model for the background assumes that the decay time distribution of $B \rightarrow h^+h^-$ candidates formed by random combinations of kaons and pions is the same as that of $B_s^0 \rightarrow \mu^+\mu^-$ candidates formed by randomly combining muons in the event. There are too few candidates passing the $B_s^0 \rightarrow \mu^+\mu^-$ selection to verify this assumption, the validity of this model and the impact of the toy studies is investigated in Section ??.

6.4 Toy Studies for fit optimisation

The strategy to measure the $B_s^0 \rightarrow \mu^+\mu^-$ effective lifetime was described earlier in Section 6.1, however given the extremely rare nature of $B_s^0 \rightarrow \mu^+\mu^-$ decays, the stability and performance of the final fit will be highly dependant on maximum likelihood fit to the invariant mass distribution. Toy studies were performed to determine the mass range and background components included in the maximum likelihood fit would produce the smallest expected uncertainty on the measured effective lifetime for the data set.

The expected number of signal and background decays in the data set passing the $B_s^0 \rightarrow \mu^+\mu^-$ selection in the mass range 4600 - 6000 MeV/ c^2 were used as the basis for the toy studies. The expected background yields were calculated using the same methods described in Section 5.3 but taking into account the looser particle identification requirement and the cut placed on the global BDT. The number of $B_s^0 \rightarrow \mu^+\mu^-$ and $B^0 \rightarrow \mu^+\mu^-$ decays are calculated using the normalisation factors in Section 5.4 and assuming the branching fraction values predicted by the Standard Model. The expected yields are shown in Table 6.4.

Decay	Expected yield
$B_s^0 \rightarrow \mu^+ \mu^-$	30.94
$B^0 \rightarrow \mu^+ \mu^-$	3.27
$B \rightarrow h^+ h^-$	9.68
$\Lambda_b^0 \rightarrow p \mu^- \nu_\mu$	13.34
$B^0 \rightarrow \pi^- \mu^+ \nu_\mu$	40.50
$B_s^0 \rightarrow K^- \mu^+ \nu_\mu$	9.13
$B^+ \rightarrow \pi^+ \mu^+ \mu^-$	6.01
$B^0 \rightarrow \pi^0 \mu^+ \mu^-$	4.86
$B_c^+ \rightarrow J/\psi \mu^+ \nu_\mu$	9.79
Combinatorial background	66.23

Table 6.4 Number of expected decays in data passing the $B_s^0 \rightarrow \mu^+ \mu^-$ effective lifetime selection.

The toy studies are performed by generating the mass and decay time distributions for the expected number of signal and background decays using the *pdfs* described in Section 6.2 and 6.3 and assuming the Standard Model prediction for $\tau_{\mu\mu}$ and taking the slope of the combinatorial background mass *pdf* from simulated decays. Then sWeights are computed from an unbinned maximum likelihood fit to the invariant mass distribution and the lifetime and its inverse are measured by a unbinned maximum likelihood fit to the signal weighted decay time distribution. A series of different mass ranges and background components included in the mass fit were tested. For each possible configuration 10,000 toy studies were performed and the performance of each configuration was evaluated using a couple of different metrics. The first, is the median expected uncertainty of the $B_s^0 \rightarrow \mu^+ \mu^-$ lifetime and inverse lifetime, the median rather than the mean uncertainty is used due to the asymmetric spread of uncertainties observed for the expected statistics. The second measure, is the pull distributions of any free parameters in the fit, where the pull is defined as $(x - \mu)/\sigma$ with x the measured parameter value, μ the value used in the generation and σ the uncertainty on the measured parameter value. Ideally the pull distributions will be Gaussian in shape with a mean at 0 and a width of 1.

The details of the toy studies performed are given in Section 6.4.2, however first is a discussion of whether the $B_s^0 \rightarrow \mu^+ \mu^-$ lifetime or inverse lifetime should be measured given the expected number of decays present in the data set.

6.4.1 To fit for τ or τ^{-1}

During the development of the fit strategy the toy studies produced biased pull distributions for the measured $B_s^0 \rightarrow \mu^+\mu^-$ effective lifetime no matter what mass fit configuration or acceptance function was used. The pull distribution for the effective lifetime, $\tau_{\mu\mu}$, is shown in Figure 6.10 for a simplified configuration where no acceptance function is used and only signal and combinatorial background decays are generated in the mass range 4900 - 6000 MeV/ c^2 . The distribution is clearly not Gaussian in shape. The bias was more pronounced in early stages of the analysis development which was done assuming the expect signal and background yields of only the Run 1 data set.

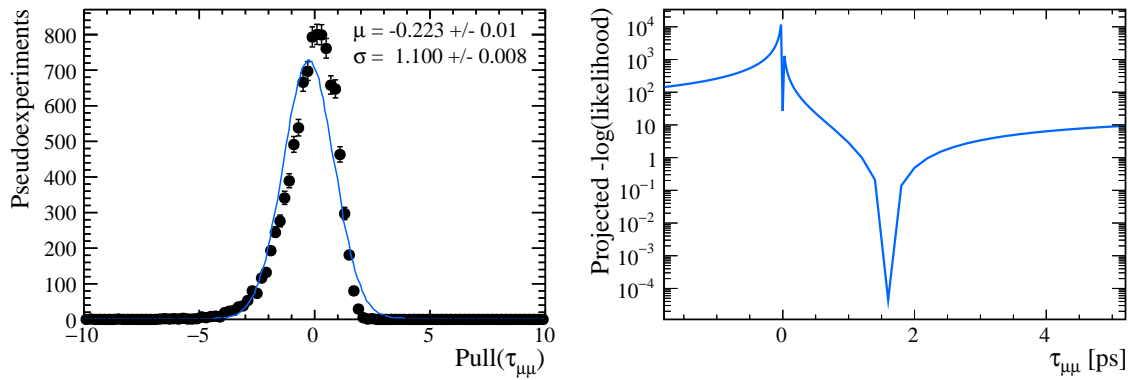


Fig. 6.10 Pull distribution (left) for $\tau_{\mu\mu}$ using a simplified configuration where no acceptance function is used and only signal and combinatorial background decays are generated in the mass range 4900 - 6000 MeV/ c^2 with the expected statistics for 4.4 fb $^{-1}$ of data. Likelihood profile for $\tau_{\mu\mu}$ (right).

The log-likelihood profile of the fit at a function of $\tau_{\mu\mu}$ reveals the cause of the biased pull distribution. For the simplified studies illustrated in Figure ?? the decay time is modelled by

$$N(t, \tau^{\mu\mu}) = N_0 e^{-t/\tau_{\mu\mu}} \quad (6.7)$$

The likelihood profile as a function of decay time for this model is shown in Figure ?? and there is a clear discontinuity at the zero. The discontinuity arises because the value of $N(t, \tau)$ approaches zero as τ reduces in value until at the origin when $\tau = 0$ and $N(t, \tau)$ jumps to infinity. The jump in value is reflected as the discontinuity in the log-likelihood profile. At the low statistics expected for the data set, particularly when only Run 1 data was considered, the fitted value for $\tau_{\mu\mu}$ is only a few standard deviations of the discontinuity, therefore leading the bias in the statistical uncertainty and hence the pull distributions. However as the number of expected signal and background decays are increased the $\tau_{\mu\mu}$ pull distributions become Gaussian in shape as shown

in Figure 6.11. This is as expected for when the statistical uncertainty deceases and the discontinuity of Figure ?? is no longer within a few standard deviations of the measured $\tau_{\mu\mu}$.

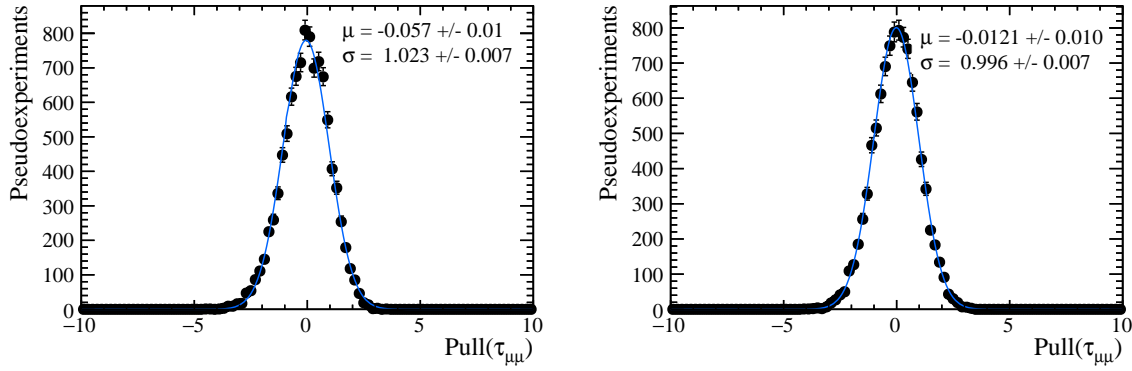


Fig. 6.11 Pull distribution for $\tau_{\mu\mu}$ using simplified toys for 50 fb^{-1} (left) and 300 fb^{-1} (right) using a simplified configuration where no acceptance function is used and only signal and combinatorial background decays are generated in the mass range $4900 - 6000 \text{ MeV}/c^2$.

The bias in the $\tau_{\mu\mu}$ pull distribution shows that the distribution cannot be interpreted in the usually way and also that the statistical uncertainties from the maximum likelihood to the weighted decay time distribution may not be correct.

Another way to assess the accuracy of the statistical uncertainties returned by the maximum likelihood fit is the coverage of the uncertainties; the percentage of fitted $\tau_{\mu\mu}$ values from the toy studies that fall within 1, 2 and 3 standard deviations of the lifetime used is the input value for the toy studies. Table 6.5 shows the coverage of the statistical uncertainties for $\tau_{\mu\mu}$ for 10,000 toy studies for the expected $B_s^0 \rightarrow \mu^+\mu^-$ and combinatorial background yields with 4.4 fb^{-1} alongside the intervals expected for a Gaussian distribution. The simple toy configuration used to produce the log-likelihood function is used. A comparison between the coverage of $\tau_{\mu\mu}$ and the Gaussian intervals shows that the coverage of the statistical uncertainties is very close to the expected values.

	$\tau_{\mu\mu}$	$\Gamma_{\mu\mu}$	Gaussian
1σ	68.50%	67.92%	68.27%
2σ	93.44%	95.91%	95.45 %
3σ	98.06%	99.55%	99.73 %

Table 6.5 Coverage.

Alternatively, a way to get around having a biased pull distribution is to measure the inverse of the effective lifetime, $\tau_{\mu\mu}^{-1} \equiv \Gamma_{\mu\mu}$. The pull distributions for $\Gamma_{\mu\mu}$ are shown in Figure 6.12 and produce unbiased pull values regardless of the amount of data. This is unsurprising given the smooth log-likelihood profile as a function of $\Gamma_{\mu\mu}$ also shown in Figure 6.12. Furthermore the statistical coverage of $\Gamma_{\mu\mu}$ is closer to the expected Gaussian coverage than the coverage of $\tau_{\mu\mu}$. However the lifetime is a more interesting variable from a physics point of view due to its relationship with $A_{\Delta\Gamma}$.

Ideally the fit strategy would be performed to extract the lifetime not the inverse lifetime, however for the moment the maximum likelihood fit for both $\tau_{\mu\mu}$ and $\Gamma_{\mu\mu}$ will be used in the toy studies. The statistical coverage for both parameters is good and using either is reasonable. The final decision will be made based on the statistical coverage for the observed number of decays in the data set.

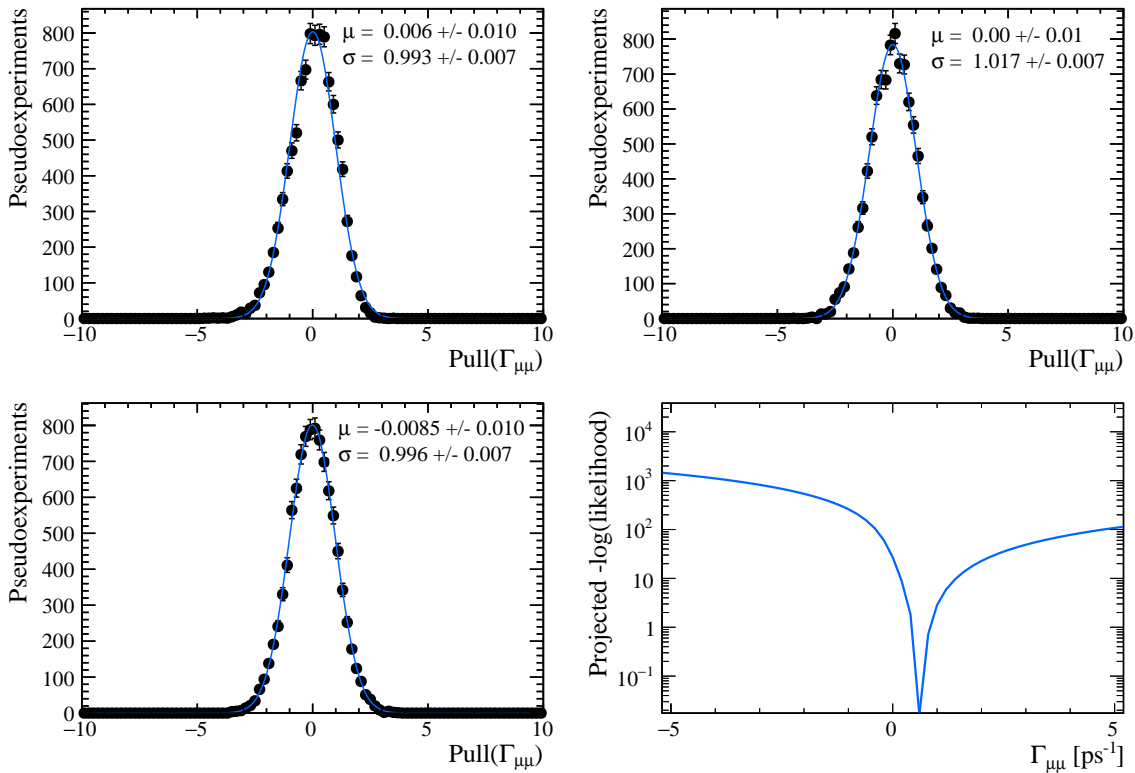


Fig. 6.12 Pull distribution for $\Gamma_{\mu\mu}$ using simplified toy studies for 4.4 (top left), 50 (top right) and 300 (bottom left) fb^{-1} and the likelihood profile as a function of $\Gamma_{\mu\mu}$ (bottom right).

6.4.2 Toy Results

The mass distribution of expected number $B_s^0 \rightarrow \mu^+ \mu^-$ candidates passing the effective lifetime selection is shown in Figure 6.13 alongside the corresponding decay time distribution. The contributions from the different signal and background sources are shown and the backgrounds beneath the B_s^0 mass peak are the combinatorial background and the tails of the $B \rightarrow h^+ h^-$, and $\Lambda_b^0 \rightarrow p \mu^- \nu_\mu$ backgrounds. The expected mass distribution is used to determine a range of mass fit configurations to be tested using toy studies to find the configuration that produces the smallest expected uncertainty on the measurement of $\tau_{\mu\mu}$ and $\Gamma_{\mu\mu}$.

In each mass fit configuration the mass *pdf* in equation 6.2 is used and the mass ranges and backgrounds included in the *pdf* for the different configurations are given in Table 6.6.

For each possible mass fit configuration the $B_s^0 \rightarrow \mu^+ \mu^-$, $B^0 \rightarrow \mu^+ \mu^-$ and combinatorial background yields are left free in the fit whereas the yields of any other backgrounds are constrained to their expected values. The mass shapes of all components are fixed in the maximum likelihood fit except the slope of the combinatorial background because this is not accurately known in data. The Standard Model prediction, $\tau_{\mu\mu} = tH$, for the $B_s^0 \rightarrow \mu^+ \mu^-$ effective lifetime is used to generate events for the toy studies where τ_H is taken from the PDG value and regardless of which background components are included in the mass fit all backgrounds are generated for each mass range. The *pdfs* used in the toy studies are detailed in Appendix ??.

A total of 10,000 toy studies are performed for each mass configuration and the results are given in Table 6.7. The mean and widths of $\Gamma_{\mu\mu}$, the $B_s^0 \rightarrow \mu^+ \mu^-$ yield and combinatorial background yield and slope as well as the median expected uncertainty on $\tau_{\mu\mu}$ and $\Gamma_{\mu\mu}$ are used to measure the performance of each mass fit configuration. The pull distribution of the fit for $\tau_{\mu\mu}$ is not used to assess the performance of each mass fit configuration given the discussion in Section 6.4.1.

The expected statistical uncertainties for $\tau_{\mu\mu}$ and $\Gamma_{\mu\mu}$ are smallest for mass of the simplest mass fit configuration, number 11, where the mass range is restricted to 5320 - 6000 MeV/ c^2 and only the $B_s^0 \rightarrow \mu^+ \mu^-$ and combinatorial background components are used in the total mass *pdf*. The mean and widths for the different pull distributions are consistent with the expected mean of 0 and width of 1 for this fit configuration. The larger mass ranges with more background components included in the mass *pdf* have larger expected uncertainties for $\tau_{\mu\mu}$ and $\Gamma_{\mu\mu}$ as well as clearly biased pull distributions. It is not surprising that the simplest fit performs the best given the very low expected number of events.

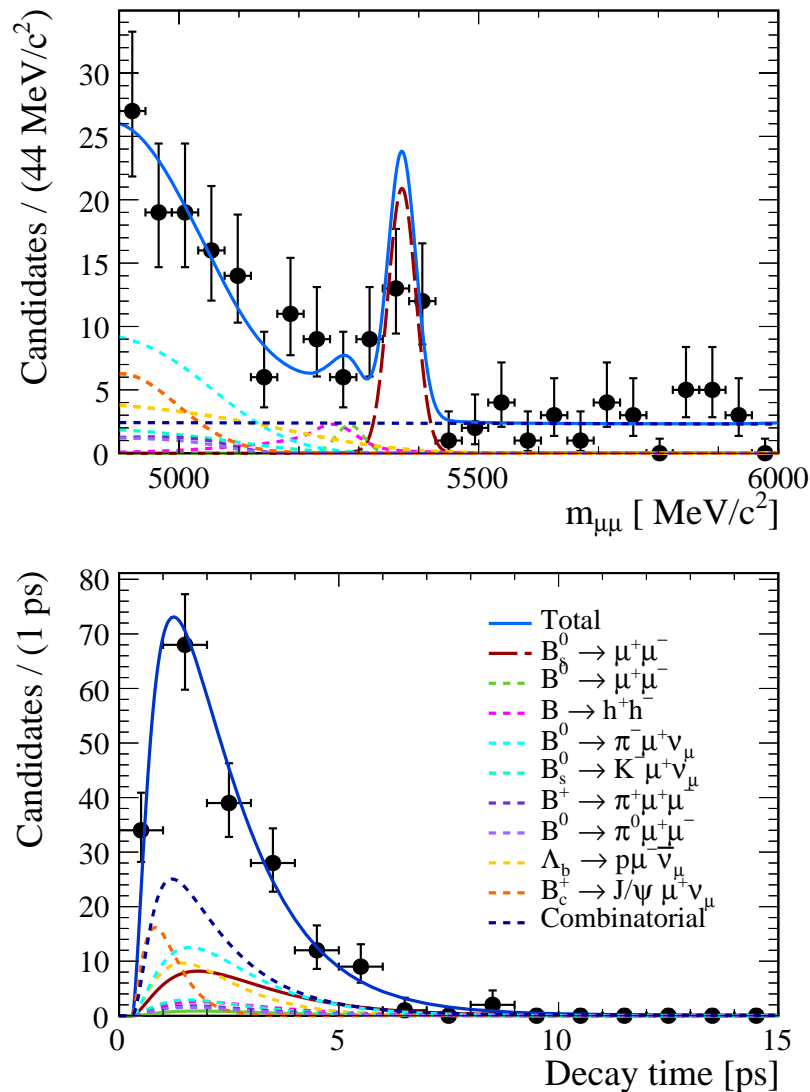


Fig. 6.13 Mass and decay time distributions for the generated decays in the mass range 4900 - 6000.

Fit no.	Mass Range / MeV/ c^2	Components included in the mass <i>pdf</i>	
		Free yields free	Fixed yields
1.	4900 - 6000	$B_s^0 \rightarrow \mu^+ \mu^-$, $B^0 \rightarrow \mu^+ \mu^-$, comb. bkg. $B_s^0 \rightarrow K^- \mu + \nu_\mu$, $B^+ \rightarrow \pi^+ \mu^+ \mu^-$, $B^0 \rightarrow \pi^0 \mu^+ \mu^-$, $B_c^+ \rightarrow J/\psi \mu^+ \nu_\mu$	$B \rightarrow h^+ h^-$, $\Lambda_b^0 \rightarrow p \mu^- \nu_\mu$, $B^0 \rightarrow \pi^- \mu + \nu_\mu$, $B_s^0 \rightarrow K^- \mu + \nu_\mu$, $B^+ \rightarrow \pi^+ \mu^+ \mu^-$, $B^0 \rightarrow \pi^0 \mu^+ \mu^-$, $B_c^+ \rightarrow J/\psi \mu^+ \nu_\mu$ Mass <i>pdfs</i> for $B^0 \rightarrow \pi^- \mu + \nu_\mu$, $B_s^0 \rightarrow K^- \mu + \nu_\mu$ are combined and so are $B_{0(+)}^0 \rightarrow \pi^{0(+)} \mu^+ \mu^-$.
2.	4900 - 6000	$B_s^0 \rightarrow \mu^+ \mu^-$, $B^0 \rightarrow \mu^+ \mu^-$, comb. bkg. $B \rightarrow h^+ h^-$, $\Lambda_b^0 \rightarrow p \mu^- \nu_\mu$, $B^0 \rightarrow \pi^- \mu + \nu_\mu$, $B_s^0 \rightarrow K^- \mu + \nu_\mu$, $B^+ \rightarrow \pi^+ \mu^+ \mu^-$, $B^0 \rightarrow \pi^0 \mu^+ \mu^-$, $B_c^+ \rightarrow J/\psi \mu^+ \nu_\mu$	$B \rightarrow h^+ h^-$, $\Lambda_b^0 \rightarrow p \mu^- \nu_\mu$, $B^0 \rightarrow \pi^- \mu + \nu_\mu$, $B_s^0 \rightarrow K^- \mu + \nu_\mu$, $B^+ \rightarrow \pi^+ \mu^+ \mu^-$, $B^0 \rightarrow \pi^0 \mu^+ \mu^-$, $B_c^+ \rightarrow J/\psi \mu^+ \nu_\mu$ Mass <i>pdfs</i> for $B^0 \rightarrow \pi^- \mu + \nu_\mu$, $B_s^0 \rightarrow K^- \mu + \nu_\mu$ are combined and so are $B_{0(+)}^0 \rightarrow \pi^{0(+)} \mu^+ \mu^-$.
3.	5150 - 6000	$B_s^0 \rightarrow \mu^+ \mu^-$, $B^0 \rightarrow \mu^+ \mu^-$, comb. bkg. $B \rightarrow h^+ h^-$, $\Lambda_b^0 \rightarrow p \mu^- \nu_\mu$, $B^0 \rightarrow \pi^- \mu + \nu_\mu$, $B_s^0 \rightarrow K^- \mu + \nu_\mu$, $B^+ \rightarrow \pi^+ \mu^+ \mu^-$, $B^0 \rightarrow \pi^0 \mu^+ \mu^-$, $B_c^+ \rightarrow J/\psi \mu^+ \nu_\mu$	$B \rightarrow h^+ h^-$, $\Lambda_b^0 \rightarrow p \mu^- \nu_\mu$, $B^0 \rightarrow \pi^- \mu + \nu_\mu$, $B_s^0 \rightarrow K^- \mu + \nu_\mu$, $B^+ \rightarrow \pi^+ \mu^+ \mu^-$, $B^0 \rightarrow \pi^0 \mu^+ \mu^-$, $B_c^+ \rightarrow J/\psi \mu^+ \nu_\mu$ Mass <i>pdfs</i> for $B^0 \rightarrow \pi^- \mu + \nu_\mu$, $B_s^0 \rightarrow K^- \mu + \nu_\mu$ are combined and so are $B_{0(+)}^0 \rightarrow \pi^{0(+)} \mu^+ \mu^-$.
4.	5150 - 6000	$B_s^0 \rightarrow \mu^+ \mu^-$, $B^0 \rightarrow \mu^+ \mu^-$, comb. bkg. $B \rightarrow h^+ h^-$, $\Lambda_b^0 \rightarrow p \mu^- \nu_\mu$, $B^0 \rightarrow \pi^- \mu + \nu_\mu$, $B_s^0 \rightarrow K^- \mu + \nu_\mu$, $B^+ \rightarrow \pi^+ \mu^+ \mu^-$, $B^0 \rightarrow \pi^0 \mu^+ \mu^-$, $B_c^+ \rightarrow J/\psi \mu^+ \nu_\mu$	$B \rightarrow h^+ h^-$, $\Lambda_b^0 \rightarrow p \mu^- \nu_\mu$, $B^0 \rightarrow \pi^- \mu + \nu_\mu$, $B_s^0 \rightarrow K^- \mu + \nu_\mu$, $B^+ \rightarrow \pi^+ \mu^+ \mu^-$, $B^0 \rightarrow \pi^0 \mu^+ \mu^-$, $B_c^+ \rightarrow J/\psi \mu^+ \nu_\mu$ Mass <i>pdfs</i> for $B^0 \rightarrow \pi^- \mu + \nu_\mu$, $B_s^0 \rightarrow K^- \mu + \nu_\mu$ are combined and so are $B_{0(+)}^0 \rightarrow \pi^{0(+)} \mu^+ \mu^-$.
5.	5200 - 6000	$B_s^0 \rightarrow \mu^+ \mu^-$, $B^0 \rightarrow \mu^+ \mu^-$, comb. bkg. $B_s^0 \rightarrow \mu^+ \mu^-$, $B^0 \rightarrow \mu^+ \mu^-$, comb. bkg. $B \rightarrow h^+ h^-$, $\Lambda_b^0 \rightarrow p \mu^- \nu_\mu$, $B_c^+ \rightarrow J/\psi \mu^+ \nu_\mu$	
5.	5200 - 6000	$B_s^0 \rightarrow \mu^+ \mu^-$, $B^0 \rightarrow \mu^+ \mu^-$, comb. bkg. $B \rightarrow h^+ h^-$, $\Lambda_b^0 \rightarrow p \mu^- \nu_\mu$, $B_c^+ \rightarrow J/\psi \mu^+ \nu_\mu$	
6.	5200 - 6000	$B_s^0 \rightarrow \mu^+ \mu^-$, $B^0 \rightarrow \mu^+ \mu^-$, comb. bkg. $B \rightarrow h^+ h^-$, $\Lambda_b^0 \rightarrow p \mu^- \nu_\mu$, $B_c^+ \rightarrow J/\psi \mu^+ \nu_\mu$	
7.	5200 - 6000	$B_s^0 \rightarrow \mu^+ \mu^-$, comb. bkg. $B \rightarrow h^+ h^-$, $\Lambda_b^0 \rightarrow p \mu^- \nu_\mu$, $B_c^+ \rightarrow J/\psi \mu^+ \nu_\mu$	
8.	5250 - 6000	$B_s^0 \rightarrow \mu^+ \mu^-$, comb. bkg. $B \rightarrow h^+ h^-$, $\Lambda_b^0 \rightarrow p \mu^- \nu_\mu$, $B_c^+ \rightarrow J/\psi \mu^+ \nu_\mu$	
9.	5300 - 6000	$B_s^0 \rightarrow \mu^+ \mu^-$, comb. bkg. $B \rightarrow h^+ h^-$, $\Lambda_b^0 \rightarrow p \mu^- \nu_\mu$, $B_c^+ \rightarrow J/\psi \mu^+ \nu_\mu$	
10.	5320 - 6000	$B_s^0 \rightarrow \mu^+ \mu^-$, comb. bkg. $B \rightarrow h^+ h^-$, $\Lambda_b^0 \rightarrow p \mu^- \nu_\mu$, $B_c^+ \rightarrow J/\psi \mu^+ \nu_\mu$	

Table 6.6 Mass ranges and components included in the different mass fit configurations tested using to toy studies. In the mass fit the slopes of the combinatorial background decays are not fixed but the shapes of all other mass *pdfs* are fixed.

Fit	$\mathcal{N}(B_s^0 \rightarrow \mu^+\mu^-)$		$\mathcal{N}(\text{Comb.})$		λ		$\tau_{\mu\mu}$	$\Gamma_{\mu\mu}$		
	Mean	Width	Mean	Width	Mean	Width	σ/ps	Mean	Width	σ/ps^{-1}
1.	-0.04	1.00	-0.05	1.05	0.06	1.00	0.38	0.03	0.95	0.14
2.	-0.06	1.01	-0.05	1.05	0.09	1.01	0.37	-0.01	0.96	0.13
3.	-0.04	0.99	-0.08	1.03	-0.04	0.99	0.41	0.00	0.94	0.15
4.	-0.03	0.99	-0.10	1.02	-0.03	1.00	0.40	0.03	0.96	0.15
5.	-0.11	0.99	0.10	1.03	-0.25	1.04	0.40	0.00	0.95	0.15
6.	-0.15	1.03	0.09	1.02	-0.17	1.02	0.31	-0.01	0.98	0.11
7.	0.36	1.05	1.25	0.93	-1.62	1.11	0.32	-0.12	0.99	0.11
8.	-0.52	1.05	1.73	0.89	-2.23	1.08	0.33	-0.15	0.99	0.12
9.	0.45	1.04	1.29	0.91	-1.78	1.13	0.33	-0.14	0.99	0.12
10.	-0.08	1.03	0.36	0.98	-0.49	1.06	0.30	-0.05	1.00	0.11
11.	0.00	1.01	0.06	1.02	-0.10	1.02	0.29	0.00	1.00	0.11

Table 6.7 Results for the toy studies testing the mass fit configuration. The mean and width of the pull distributions for the $B_s^0 \rightarrow \mu^+\mu^-$ and combinatorial background yields and the slope of the combinatorial background mass *pdf*, λ , are shown along with the expected statistics uncertainty on $\tau_{\mu\mu}$ and $\Gamma_{\mu\mu}$. The uncertainties on the means and widths are 0.01 for all configurations.

Therefore the fit configuration number 9 is chosen to measure the $B_s^0 \rightarrow \mu^+ \mu^-$ effective lifetime. Figure 6.14 gives an example of the mass and decay time maximum likelihood fits for the chosen configuration, it is clear from Figure 6.13 that the number of background decays from $B^0 \rightarrow \mu^+ \mu^-$, $B \rightarrow h^+ h^-$ and $\Lambda_b^0 \rightarrow p \mu^- \nu_\mu$ is extremely small above 5320 MeV/ c^2 therefore these backgrounds do not need to be modelled in the mass *pdf*. The affect on the final result of not modelling these backgrounds is estimated in Section ??.

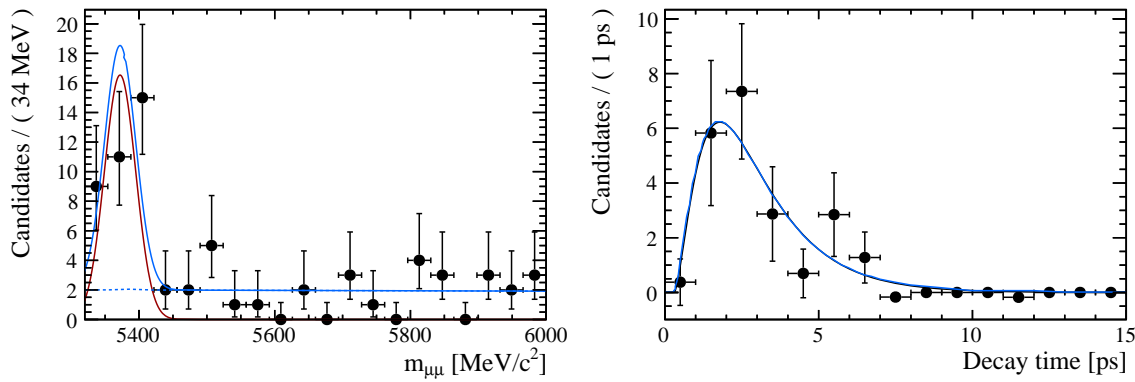


Fig. 6.14 Toy example of the mass and decay time maximum likelihood fits for the chosen fit configuration where only components for $B_s^0 \rightarrow \mu^+ \mu^-$ and combinatorial background are modelled in the mass *pdf*.

The expected uncertainties for the chosen fit configuration for $\tau_{\mu\mu}$ and $\Gamma_{\mu\mu}$ are $\sigma(\tau_{\mu\mu}) = 0.28$ ps and $\sigma(\Gamma_{\mu\mu}) = 0.11$ ps $^{-1}$. However due to the low expected number of decays there is a large spread in the expected uncertainties as shown in Figure 6.15. Therefore the uncertainties on the measurements would range between 0.1 - 0.8 ps for $\tau_{\mu\mu}$ and 0.07 - 0.2 ps $^{-1}$ for $\Gamma_{\mu\mu}$.

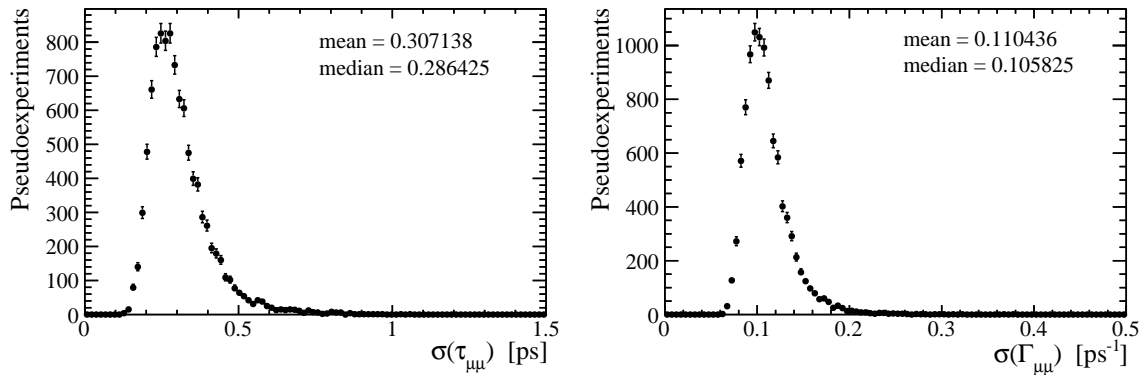


Fig. 6.15 Expected statistical uncertainties for $\tau_{\mu\mu}$ (left) and $\Gamma_{\mu\mu}$ (right) using fit configuration number 11.

6.5 Results

The results of the unbinned maximum likelihood fit to the dimuon mass distribution and the sWeighted decay time of $B_s^0 \rightarrow \mu^+\mu^-$ candidates for 4.4 fb^{-1} of Run 1 and Run 2 data are shown in Figure 6.16. The number of observed decays was 22 ± 6 $B_s^0 \rightarrow \mu^+\mu^-$ decays and 20 ± 6 combinatorial background decays. The measured values of $\tau_{\mu\mu}$ and $\Gamma_{\mu\mu}$ are

$$\tau_{\mu\mu} = 2.04 \pm 0.44 \text{ ps} \quad (6.8)$$

$$\Gamma_{\mu\mu} = 0.489 \pm 0.117 \text{ ps}^{-1} \quad (6.9)$$

where the uncertainties are only statistical. The results are consistent with the Standard Model prediction of $\tau_{\mu\mu} = \tau_H$ within 1σ and within 1.5σ of $\tau_{\mu\mu} = \tau_L$.

The observed number of decays is lower than expected and the statistical coverage of the uncertainties has been checked using toy studies generated with the observed number of decays. In the toy studies the all background decays are generated at the expected level. The coverage of both $\tau_{\mu\mu}$ and $\Gamma_{\mu\mu}$ statistical uncertainties is good, as shown in Table 6.8, therefore the result of the more interesting $\tau_{\mu\mu}$ and its statistical uncertainty can be trusted as accurate.

	$\tau_{\mu\mu}$	$\Gamma_{\mu\mu}$	Gaussian
1σ	68.83%	67.76%	68.27%
2σ	93.11%	95.55%	95.45 %
3σ	97.92%	99.67%	99.73 %

Table 6.8 Coverage of observed decays.

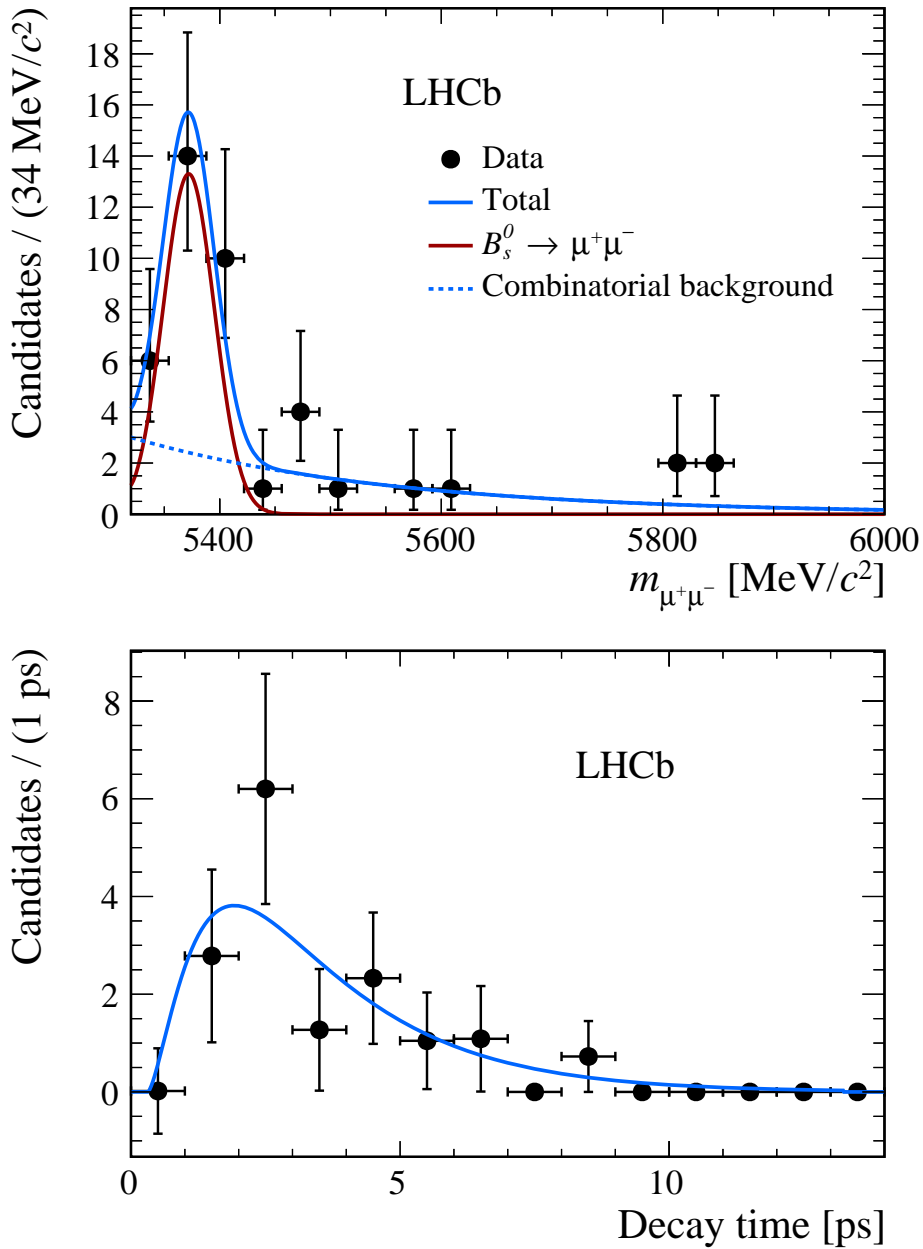


Fig. 6.16 Maximum likelihood fit to the invariant mass distribution (left) and weighted decay time distribution (right) of $B_s^0 \rightarrow \mu^+\mu^-$ candidates in 4.4 fb^{-1} of data collected by the LHCb experiment. $B_s^0 \rightarrow \mu^+\mu^-$ candidates are described by the red peak in the mass plot and combinatorial background by the blue dashed line, the total *pdf* is given by the solid blue line.

Chapter 7

Systematic Uncertainties and Cross Checks

Chapter 8

Summary and Future Outlook

Bibliography

- [1] C. member states. <http://home.cern/about/member-states>.
- [2] S. Amato *et al.*, “LHCb technical proposal,” 1998.
- [3] A. A. Alves, Jr. *et al.*, “The LHCb Detector at the LHC,” *JINST*, vol. 3, p. S08005, 2008.
- [4] “LHCb technical design report: Reoptimized detector design and performance,” 2003.
- [5] R. Aaij *et al.*, “LHCb Detector Performance,” *Int. J. Mod. Phys.*, vol. A30, no. 07, p. 1530022, 2015.
- [6] R. Aaij *et al.*, “Performance of the LHCb Vertex Locator,” *JINST*, vol. 9, p. 09007, 2014.
- [7] R. Aaij *et al.*, “Measurement of the track reconstruction efficiency at LHCb,” *JINST*, vol. 10, no. 02, p. P02007, 2015.
- [8] M. Adinolfi *et al.*, “Performance of the LHCb RICH detector at the LHC,” *Eur. Phys. J.*, vol. C73, p. 2431, 2013.
- [9] F. Archilli *et al.*, “Performance of the Muon Identification at LHCb,” *JINST*, vol. 8, p. P10020, 2013.
- [10] R. Aaij *et al.*, “Absolute luminosity measurements with the LHCb detector at the LHC,” *JINST*, vol. 7, p. P01010, 2012.
- [11] O. Lupton and G. Wilkinson, *Studies of $D^0 \rightarrow K_s^0 h^+ h^-$ decays at the LHCb experiment*. PhD thesis, Oxford U., Jul 2016. Presented 14 Sep 2016.
- [12] P. Mato, “GAUDI-Architecture design document,” 1998.
- [13] R. Antunes-Nobrega *et al.*, *LHCb computing: Technical Design Report*. Technical Design Report LHCb, Geneva: CERN, 2005. Submitted on 11 May 2005.
- [14] F. Stagni *et al.*, “LHCbDirac: Distributed computing in LHCb,” *J. Phys. Conf. Ser.*, vol. 396, p. 032104, 2012.
- [15] R. Brun and F. Rademakers, “ROOT: An object oriented data analysis framework,” *Nucl. Instrum. Meth.*, vol. A389, pp. 81–86, 1997.

- [16] I. Belyaev, T. Brambach, N. H. Brook, N. Gauvin, G. Corti, K. Harrison, P. F. Harrison, J. He, C. R. Jones, M. Lieng, G. Manca, S. Miglioranzi, P. Robbe, V. Vagnoni, M. Whitehead, J. Wishahi, and the LHCb Collaboration, “Handling of the generation of primary events in Gauss, the LHCb simulation framework,” *Journal of Physics: Conference Series*, vol. 331, p. 032047, 2011.
- [17] M. Clemencic, G. Corti, S. Easo, C. R. Jones, S. Miglioranzi, M. Pappagallo, and P. Robbe, “The LHCb simulation application, Gauss: Design, evolution and experience,” *J. Phys. Conf. Ser.*, vol. 331, p. 032023, 2011.
- [18] T. Sjostrand, S. Mrenna, and P. Z. Skands, “PYTHIA 6.4 Physics and Manual,” *JHEP*, vol. 05, p. 026, 2006.
- [19] T. Sjostrand, S. Mrenna, and P. Z. Skands, “A Brief Introduction to PYTHIA 8.1,” *Comput. Phys. Commun.*, vol. 178, pp. 852–867, 2008.
- [20] D. J. Lange, “The EvtGen particle decay simulation package,” *Nucl. Instrum. Meth.*, vol. A462, pp. 152–155, 2001.
- [21] P. Golonka and Z. Was, “PHOTOS Monte Carlo: A Precision tool for QED corrections in Z and W decays,” *Eur. Phys. J.*, vol. C45, pp. 97–107, 2006.
- [22] S. Agostinelli *et al.*, “GEANT4: A Simulation toolkit,” *Nucl. Instrum. Meth.*, vol. A506, pp. 250–303, 2003.
- [23] J. Allison *et al.*, “Geant4 developments and applications,” *IEEE Trans. Nucl. Sci.*, vol. 53, p. 270, 2006.
- [24] I. Bird, “Computing for the Large Hadron Collider,” *Ann. Rev. Nucl. Part. Sci.*, vol. 61, pp. 99–118, 2011.
- [25] W. L. C. Grid. <http://www.cern.ch/LHCgrid>.
- [26] S. Paterson and A. Tsaregorodtsev, “DIRAC Infrastructure for Distributed Analysis,” Feb 2006.
- [27] T. Skwarnicki, *A study of the radiative cascade transitions between the Upsilon-prime and Upsilon resonances*. PhD thesis, Institute of Nuclear Physics, Krakow, 1986. [DESY-F31-86-02](#).
- [28] H. Albrecht *et al.*, “Search for hadronic $b \rightarrow u$ decays,” *Phys. Lett.*, vol. B241, pp. 278–282, 1990.
- [29] M. Pivk and F. R. Le Diberder, “SPlot: A Statistical tool to unfold data distributions,” *Nucl. Instrum. Meth.*, vol. A555, pp. 356–369, 2005.
- [30] W. Verkerke and D. P. Kirkby, “The RooFit toolkit for data modeling,” *eConf*, vol. C0303241, p. MOLT007, 2003. [,186(2003)].
- [31] R. Aaij *et al.*, “Measurement of the CP violating phase ϕ_s in $\bar{B}_s^0 \rightarrow J/\psi f_0(980)$,” *Phys. Lett.*, vol. B707, pp. 497–505, 2012.

Appendix A

Distributions of input variables for the global BDT

Comparison of the signal and background distributions of the input variables used in the global BDT for 2011, 2012, 2015 and 2016 data taking conditions. Signal distributions are from simulated $B_s^0 \rightarrow \mu^+\mu^-$ decays for each year that have passed the selection cuts in Table ???. The background distributions are from $b\bar{b} \rightarrow \mu^+\mu^-X$ decays in 2011, 2012, 2015 and 2016 data with $m_{\mu\mu} > 5447$ evcc and 2012 simulated $b\bar{b} \rightarrow \mu^+\mu^-X$ decays passing the selection cuts in Table ???.

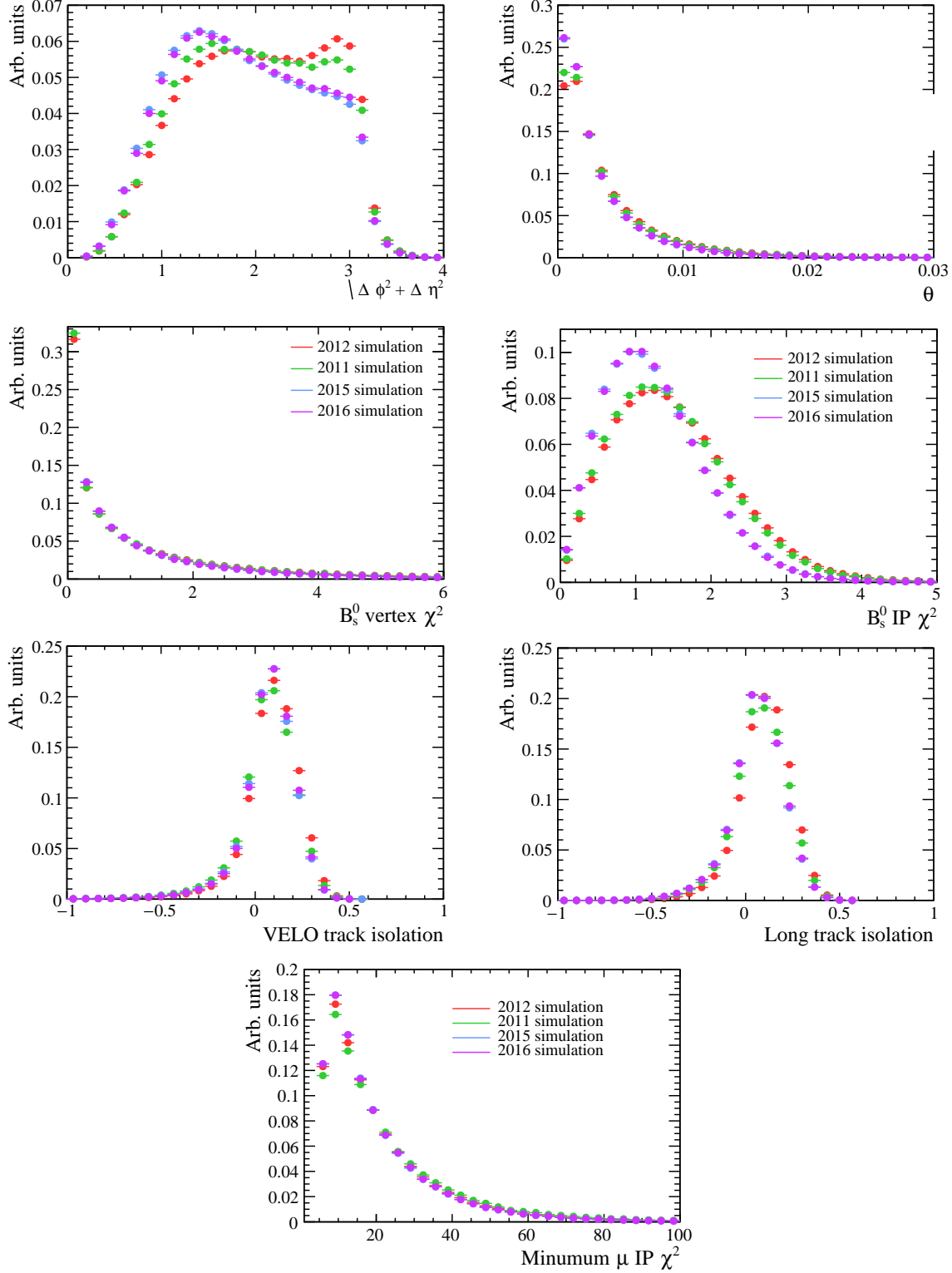


Fig. A.1 Signal distribution for input variables for the global BDT for $B_s^0 \rightarrow \mu^+ \mu^-$ simulated decays in 2011, 2012, 2015 and 2016.

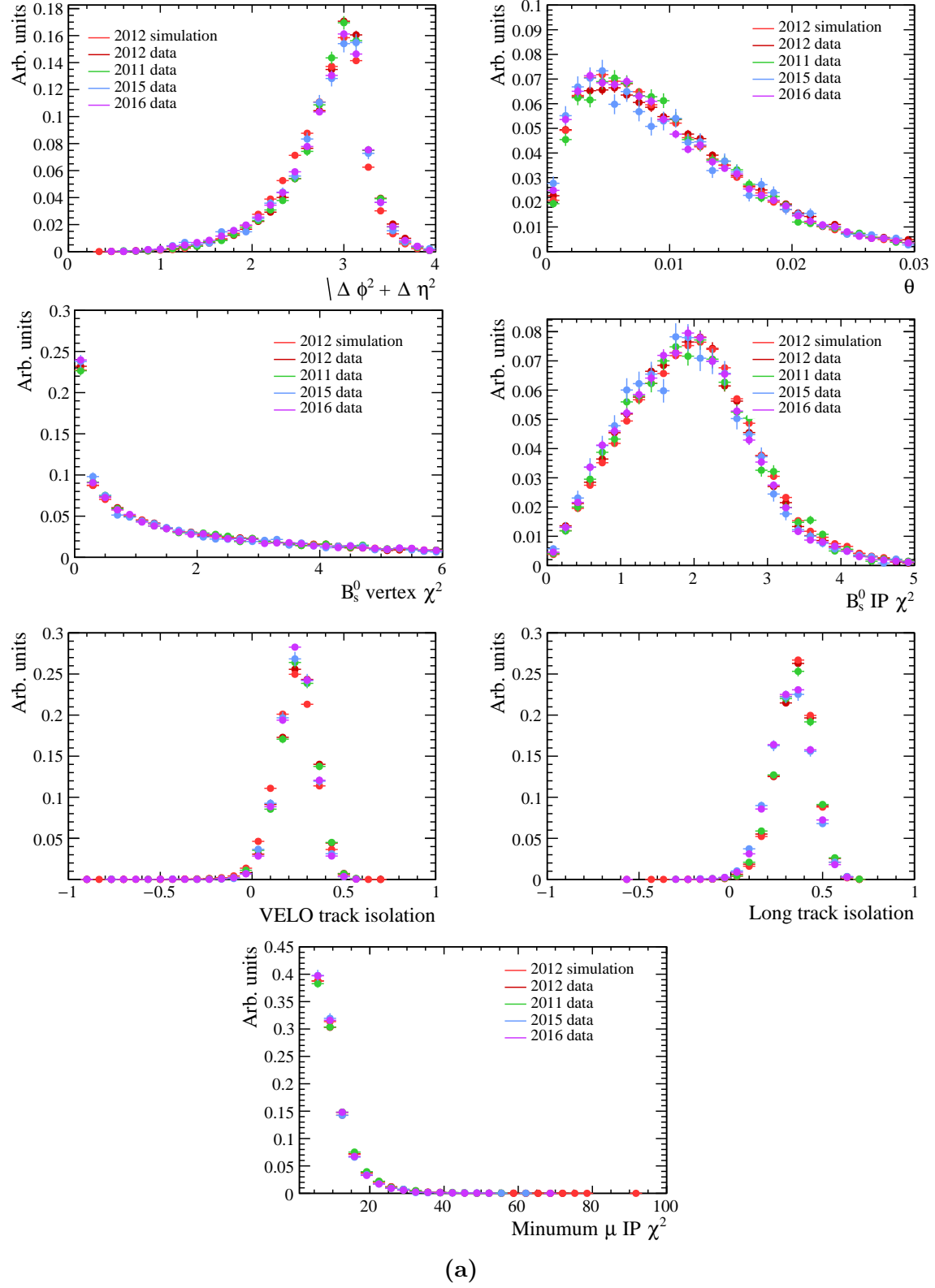


Fig. A.2 Background distribution for input variables from $b\bar{b} \rightarrow \mu^+\mu^-X$ decays in 2011, 2012, 2015 and 2016 data with $m_{\mu\mu} > 5447 \text{ MeV}/c^2$ and 2012 simulated $b\bar{b} \rightarrow \mu^+\mu^-X$ decays.

